Quantitative Colour Schlieren Techniques

Duncan Stevenson

A dissertation submitted to the Faculty of Engineering and the Built Environment, University of the Witwatersrand, in fulfillment of the requirements for the Degree of Master of Science in Engineering.

Johannesburg - 2011

Declaration

I declare that this dissertation is my own, unaided work, except where otherwise acknowledged. It is being submitted for the degree of Master of Science in Engineering in the University of the Witwatersrand, Johannesburg. It has not been submitted before for any degree or examination at any other university.

Signed on this the _____ day of _____

Duncan Stevenson

Abstract

Schlieren photography is a common name given to the optical technique of capturing changes in density of transparent media. It is possible that, with the aid of modern numerical solutions, schlieren techniques are able to produce quantitative results. Modern image processing algorithms and techniques allow for a more complex and comprehensive analysis of the flow phenomenon while still remaining non-intrusive. This dissertation describes the potential of a 2-dimensional colour schlieren system for producing quantitative data on the density field within the test section of a shock tube. Density gradient components, magnitude and direction, form the basis of the quantitative evaluation. These are encoded onto an imaging plane by means of a colour coded source mask placed along the optical axis of the schlieren system. Direction is indicated by the relative ratios of the 3 primary colours, Red, Green and Blue (RGB). Magnitude is indicated by the relative intensities of the RGB values. Sensitivity of the system is adjusted by an iris diaphragm placed at the focal point of the second parabolic mirror in the cut-off plane. The schlieren method described is applied to a two-dimensional focusing parabolic model subjected to a shock traveling at between Mach 1.3 and Mach 1.4. The experimental results of the schlieren technique are compared to computational simulations with synthetic two-dimensional colour and magnitude coding applied to the results. Image processing methods are used to determine the density gradients within the experimental images and allow comparisons to computational results. The source masks designed and used herein proved to require a greater intensity light source and thus the design of an LED light was developed. A number of existing circuits are used as building blocks and as a comparison tool in the development of the light source. In-house Computational Fluid Dynamics (CFD) has been developed with emphasis on 2-Dimensional solutions. The CFD solutions did not yield colour schlieren data thus a computational script was designed to convert the results into an image format directly comparable to the photographic images obtained by experimentation. Image processing techniques have been employed to deconstruct photographs to allow for quantitative comparisons with a calibration lens. Density gradient direction has been conclusive, however density gradient magnitude is not yet accurately determined due to light source constraints.

Acknowledgments

I would like to express sincere appreciation to all those who provided me with support and assistance for the duration of this project

My supervisor, Professor B. W. Skews, for his guidance, advice, willingness and humbling interest; For allowing me the opportunity of presenting this work at an international conference.

I would also like to thank the *National Research Foundation* (NRF) for funding my studies.

Gary Settles, Mike Hargather & James Taylor for their help with the electrical circuits.

Gary Settles & Harald Kleine for their valuable input on colour schlieren systems.

www.discovercircuits.com and www.allaboutcircuits.com forums for their valuable input and troubleshooting advice on the pulsed LED circuits.

Beith Digital Printing for countless hours and rolls of film spent on the laborious process of printing and photographing source masks.

My partner, Leila, for her unrelenting support and valued advice through the tough times.

My family for putting up with my schlieren discussions and feigning interest in a rather abstract but visually appealing topic.

Contents

List of Figures **v**

List of Tables **x**

Nomenclature **xi**

1 Introduction **1**

2 Literature Review **3**

2.1 Overview 3

2.2 Compressible flow 3

2.2.1 Waves in compressible flow 3

2.2.2 Normal shock waves 5

2.3 Schlieren Photography 6

2.3.1 History 6

2.3.2 Schlieren Systems 7

2.3.3 Schlieren Problems 9

2.3.4 Elemental Derivations 14

2.3.5 Broader Derivations 18

2.4 Light Sources 19

2.4.1 Methods of illumination 19

2.4.2 Requirements 23

2.5 Quantitative Methods . . . 23
2.5.1 CCS & BOS . . . 24
2.5.2 Rainbow & Bulls-Eye schlieren . . . 25
2.5.3 Calibration Lens . . . 26
2.6 Digital Imaging . . . 27
2.6.1 Digital image recording . . . 27
2.6.2 Image post-processing . . . 29
2.6.3 Spectral Responses . . . 33

3 Objectives **36**

4 Design Development **37**

4.1 Source Masks . . . 37
4.1.1 Software used . . . 37
4.1.2 Code Description . . . 37
4.1.3 Source mask design . . . 38
4.2 LED Light Source . . . 41
4.2.1 Design considerations . . . 41
4.2.2 Circuits examined . . . 42
4.2.3 Circuit design . . . 43
4.2.4 Circuit operation . . . 46
4.2.5 High power LED's . . . 46
4.3 Colour schlieren code . . . 48
4.3.1 Software used . . . 49
4.3.2 Code description . . . 49
4.4 Image post-processing . . . 51
4.5 Image integration . . . 55
4.6 Optical ray-tracing . . . 57

5 Apparatus **58**

5.1 Data Acquisition considerations . . . 58

5.1.1 PC . . . 58

5.1.2 DAC's . . . 58

5.1.3 Pressure and Temperature transducers . . . 59

5.2 Shock tube considerations . . . 59

5.2.1 Details . . . 59

5.3 Optical considerations . . . 60

5.3.1 General arrangement . . . 61

5.3.2 Mirrors . . . 62

5.3.3 Lenses . . . 62

5.3.4 Cameras . . . 64

5.3.5 Light sources . . . 65

5.3.6 Stands & alignment aids . . . 66

5.3.7 Iris Diaphragm . . . 67

5.4 Numerical solution considerations . . . 67

5.4.1 Software . . . 67

5.4.2 PC . . . 70

5.5 Test model . . . 70

6 Research Methodology **72**

6.1 Experimental procedure . . . 72

6.1.1 Overview . . . 72

6.1.2 Light source . . . 72

6.1.3 Source Masks . . . 74

6.1.4 Seitz shock tube . . . 75

6.1.5 Repeatability considerations . . . 76
6.2 Computational procedures . . . 77
6.2.1 Overview . . . 77
6.2.2 CFD . . . 77
6.2.3 Source mask generation . . . 80
6.2.4 Synthetic schlieren generator . . . 82
6.2.5 Comparison software . . . 83

7 Results and Discussion **85**
7.1 LED light source . . . 85
7.1.1 Circuit performance . . . 85
7.1.2 Observations . . . 100
7.2 Data processing & analysis . . . 103
7.2.1 Source mask analysis . . . 103
7.2.2 Tecplot post-processing . . . 106
7.2.3 OpenCV . . . 112
7.3 Schlieren system . . . 118
7.3.1 Optical response . . . 119
7.3.2 Image palette . . . 131

8 Conclusions **136**

9 Recommendations **138**

Bibliography **140**

Appendix A LED light sources **144**
A.1 LED Circuit . . . 144
A.2 Buttsworth et al. LED circuit . . . 146
A.3 Hargather et al. LED circuit . . . 147

Appendix B DVD **150**

List of Figures

2.1 Weak compression waves forming at a concave corner 3

2.2 Weak expansion waves forming at a convex corner 4

2.3 Stationary shock wave 4

2.4 Moving shock wave 4

2.5 Toepler's single lens schlieren system 8

2.6 Dual lens parallel light schlieren system 8

2.7 Z-type schlieren arrangement 8

2.8 Schematic showing the effects of an extended light source 10

2.9 Schematic representation of the problems due to astigmatism 11

2.10 Ray trace schematic diagram for the cylindrical lens in plan view 12

2.11 Schematic representation of the aberration due to Coma 13

2.12 Diagram of elemental light refraction by a density gradient 15

2.13 Schematic representation of a displaced source image 17

2.14 Schematic image of the test section 18

2.15 Xenon spectral distribution Hamamatsu [2005] 20

2.16 LED electromigration, Cree [2011b] 22

2.17 Colour schlieren dissection technique. (a) Rainbow method; (b) Bulls-Eye method 25

2.18 Calibration lens in the test section 26

2.19 Monochromatic image leveling illustration (a) before adjustment; (b) after adjustment 30

2.20 Monochromatic image contrast adjustment illustration (a) before adjustment; (b) after adjustment 31

2.21 Monochromatic image brightness adjustment illustration (a) before adjustment; (b) after adjustment 32

2.22 Monochromatic image threshold adjustment illustration (a) before adjustment; (b) after adjustment 33

2.23 Eye response, [Kumar et al., 2008] 34

2.24 Spectral response comparison between the human eye and CMOS/CCD sensors, [Smith, 2006] 35

4.1 Source mask schematic 38

4.2 Variety of source masks designed and printed for testing and comparison . . 40

4.3 Circuit diagram of high power LED light source 43

4.4 Photo of high power LED light circuit as tested 43

4.5 High power LED's 47

4.6 LED Lenses 48

4.7 Colour distribution wheel 50

4.8 Polar diagram illustrating the intensity of the colour variation with angle . . 50

4.9 Plot of RGB colour distribution around HSV wheel 51

4.10 Screen shot of OpenCV schlieren software calibration window 52

4.11 Screen shot of OpenCV schlieren software test image window 53

4.12 Screen shot of OpenCV schlieren software calibration window with selection . 54

4.13 Screen shot of OpenCV schlieren software console window 54

4.14 Original CFD density distribution image 55

4.15 Original CFD image subjected to a first degree derivation producing; (a) Density gradients in the x-direction; (b) Density gradients in the y-direction . 56

4.16 Cropped and integrated CFD image (a) compared to similar region of original CFD density distribution image (b) 56

5.1 Schematic representation of the Seitz shock tube 60

5.2 Schematic layout of apparatus in plan view 61

5.3 Light source schematic side layout 61

5.4 Calibration lens schematic 63

5.5 Cylindrical lens schematic 63

5.6 Flow diagram of software used to obtain colour CFD images 68

5.7 Procedure and software used to obtain quantitative density gradient plots . . 69

5.8 Use of Matlab to extract pixel information for calibration image analysis . . . 69

5.9 Test model 70

5.10 Model curved surface plot 71

6.1 Initial mesh conditions 79

6.2 Refined mesh 79

7.1 4427 IC and 74121 IC voltage outputs for 3 supply voltages with no load circuitry connected 86

7.2 4427 IC and 74121 IC voltage outputs for 3 supply voltages with the 9x9 LED array connected 88

7.3 4427 IC and 74121 voltage outputs for 3 supply voltages for the single Cree MC-E LED 89

7.4 4427 IC and 74121 voltage outputs for 3 supply voltages for the Cree MC-E LED array 90

7.5 Current draw for the 9x9 array 91

7.6 Current draw for the single Cree 92

7.7 Current draw for the Cree array 94

7.8 Short circuit MOSFET current for three supply voltages 96

7.9 MOSFET supply voltage and 9x9 LED array current for four high voltages . 97

7.10 MOSFET supply voltage and single Cree MC-E LED current for four high voltages 98

7.11 MOSFET supply voltage and Cree MC-E LED array current for four high voltages 99

7.12 Source voltage fluctuation with the Cree MC-E LED array at three high voltages 100

7.13 Images of the calibration lens placed within the test section at various ISO settings 102

7.14 Source mask comparison 104

7.15 Source mask in cut-off plane 104

7.16 Source mask in cut-off plane illustrating RGB response 105

7.17 CFD simulation images with corresponding colour schlieren interpretations . 107

7.18 CFD simulation images with corresponding colour schlieren interpretations . 108

7.19 Vertical data 109

7.20 Horizontal data 111

7.21 Calibration lens used for pixel analysis 112

7.22 Experimental image, vertical data extraction 113

7.23 Plot of vertical data 114

7.24 Experimental image, horizontal data extraction 115

7.25 Plot of horizontal data 115

7.26 Improved quality images subjected to OpenCV analysis 117

7.27 Plot of resultant density gradient magnitude for CFD and experimental results 118

7.28 Calibration lens and corresponding posterization 119

7.29 Calibration lens image decompiled into monochromatic RGB components . . 121

7.30 33% calibration lens radius 122

7.31 66% calibration lens radius 123

7.32 100% calibration lens radius 123

7.33 Calibration lens response - Yellow 124

7.34 Calibration lens response - Red 125

7.35 Calibration lens response - Magenta 125

7.36 Calibration lens response - Blue 126

7.37 Calibration lens response - Cyan 126

7.38 Calibration lens response - Green 127

7.39 Images showing the rotation of the calibration lens within the test section . . 129

7.40 Extracted center positions 131

7.41 Progression of shock wave at $20\mu s$ intervals prior to shock focus 132

7.42 Progression of shock wave at $20\mu s$ intervals after shock focus 133

7.43 Raw and Jpeg image comparison 134

9.1 Figure of a possible LED layout to replace the source mask 138

A.1 High power LED circuit 144

A.2 Excerpt fromButtsworth and Ahfock [2003] 146

A.3 Original 1 LED system Hargather et al. [2009] 147

A.4 High power LED power supply Hargather et al. [2009] 148

A.5 High power LED pulsing circuit Hargather et al. [2009] 149

List of Tables

2.1 Benefits and drawbacks for mirror and lens based schlieren systems 7

5.1 Table of calibration lens data 63

5.2 Table of cylindrical lens data 64

7.1 Table comparing the amperage drawn by the 9x9 LED array with and without a MOSFET driver 92

7.2 Table comparing the amperage drawn by the single Cree MC-E LED with and without a MOSFET driver 93

7.3 Table comparing the amperage drawn by the Cree MC-E LED array with and without a MOSFET driver 95

7.4 Table illustrating the amperage which may be passed by the MOSFET during short circuit at low voltages 96

7.5 Table of current drawn by the 9x9 LED array for high voltages 97

7.6 Table of current drawn by the Cree MC-E LED array for high voltages 98

7.7 Table of current drawn by the Cree MC-E LED array for high voltages 99

7.8 Table containing pixel values for each channel for each segment of the source mask 106

A.1 Circuit bill of materials 145

Nomenclature

α Astigmatic difference

η Refractive index

γ Ratio of specific heats of air

κ Shockwave distance travelled

λ Illumination

ϕ Mirror diameter

ρ Gas density

τ Average light source pulse duration

φ Schlieren system angle

ξ Light refraction angle

a Local speed of sound

c Speed of light

d Image distances

f Focal length

i Current

k Gladstone-Dale constant

L Test section width

M Mach number

P Gas pressure

p Power

R Specific gas constant

r Resistance

T Gas temperature

t Time

v Voltage

x x co-ordinate

y y co-ordinate

z z co-ordinate

Chapter 1

Introduction

Fluid flow visualization may be achieved in a number of ways; many involve intrusive testing and measurements which, by implication, has a direct effect on the phenomenon occurring within the flow field. Optical methods are non-intrusive and allow the measurement of fluid characteristics without disturbance or influence. In many cases, optical methods are the only means available to acquire detailed visual information about the inner workings of a flow field. Shock wave and high speed flow research relies, to a large extent, on optical methods since adding foreign particles, or tracers, may not adhere to the fluids own dynamics. It would be very difficult to validate theoretical or mathematical models without various different forms of flow visualization.

Schlieren photography is a common name given to the optical technique of capturing changes in density of transparent media. It is possible that, with the aid of modern numerical solutions, the schlieren techniques are able to produce quantitative results. Modern image processing algorithms and techniques allow for a more complex and comprehensive analysis of the flow phenomenon while still remaining non-intrusive.

Two-dimensional direction indicating colour schlieren allows the direction, and to some extent the magnitude, of a density gradient at a given point in the test section to be recorded. It has been stated that while a system such as this will produce clear directionality, magnitude information might only be coarsely determined since the extent of colour saturation is not clearly visible in outputted images.

Currently within the *Flow Research Unit* (FRU) a satisfactorily operating colour schlieren system is not set up. The colour schlieren systems designed previously have either been too complicated to manufacture or have not allowed for the necessary fine adjustments to be made to obtain high quality images. For the technique to be quantitatively useful, high quality images must be obtained which accurately reflect the density gradients and directions within the test section. Once these 2-dimensional images containing density gradient information are acquired, the colours may be compared to the colours produced by calibration lens of known specifications and thus a density gradient and its direction may be found for each point in the test section.

This technique could prove to be sufficiently powerful in the understanding of flow characteristics. The system should also allow the density gradients in all directions to be determined with a single test in comparison to the direction yielding monochromatic systems.

Chapter 2

Literature Review

2.1 Overview

This chapter of the Master's dissertation aims to discuss the technical nature of shock waves and compressible flow; the theory of schlieren photography and its applications to flow research and the ability to use a calibration lens to improve analysis of schlieren images. Thereafter, previous attempts to quantify schlieren methods will be exposed as well to disclose LED usage as pulsed and continuous light sources for schlieren photography.

2.2 Compressible flow

2.2.1 Waves in compressible flow

Not all wave phenomenon present in compressible fluid flows result in shock waves being formed. Weak expansion or compression waves can be generated depending on the nature of the compressible flow field and what the flow field is interacting with.

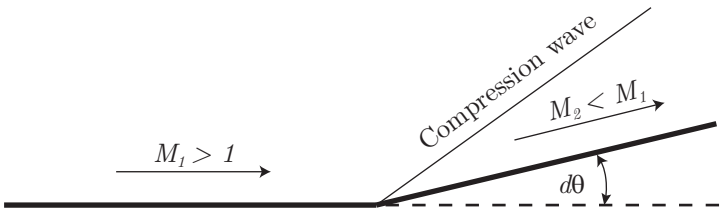


Figure 2.1: Weak compression waves forming at a concave corner

A weak compression wave, figure 2.1, may occur due to flow interacting with a concave corner whereas a weak expansion wave may occur in a similar but convex corner, figure 2.2, for infinitesimal values of $d\theta$. Both waves generated are weak and thus isentropic flow

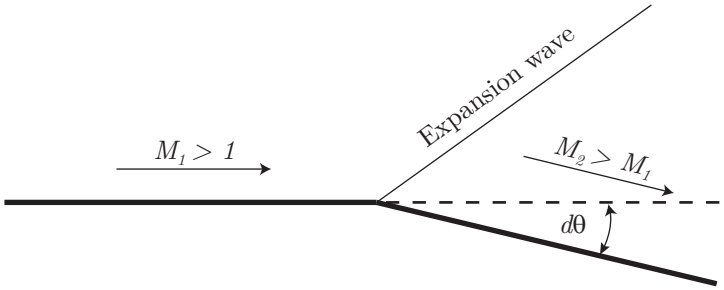


Figure 2.2: Weak expansion waves forming at a convex corner

analysis is possible across the waves. It is intuitive that across the compression wave, the flow is decelerated and the gas density increases whereas, across the expansion wave, flow is accelerated and gas density decreases.

A shock wave is essentially a discontinuity within a compressible medium. This discontinuity between pressure, temperature and density is in the region of $\backsim 10^{-4}mm$ thick and causes an enormous amount of energy to be dissipated. It is only possible for a shock to be generated when a compression wave is present since an adiabatic expansion wave would require a decrease in entropy and this violates the second law of thermodynamics [Potter and Wiggert, 2007].

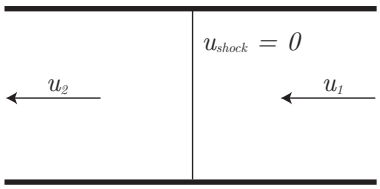


Figure 2.3: Stationary shock wave

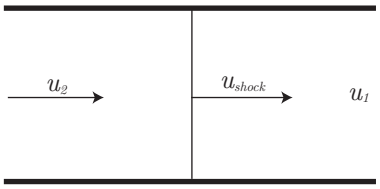


Figure 2.4: Moving shock wave

Shock waves may be moving or stationary depending on the conditions in which they are generated. A shock is said to be stationary, figure 2.3, when the gas in which it propagates is traveling at the same speed but in the opposite direction to that of the shock wave. Converse to this situation is a moving shock wave in a stationary or low velocity gas, figure 2.4.

Shock waves can be created by fast moving objects such as supersonic aircraft or projectiles; explosions such as balloons popping or chemical explosions; jet engines compressing and expelling superheated air out of the turbine; expansions in shock tubes etc. The velocity which the shock wave propagates through a given media is proportional to the strength of

the given shock wave. This study on shock wave visualization and quantitative methods deals with normal shock waves traveling down a shock tube in an ideal gas [Balachandran, 2010].

2.2.2 Normal shock waves

Normal shock waves are defined as wave fronts which move perpendicular, or normal, to the flow stream. It is possible to analyze these wave fronts with simple one dimensional flow equations. Oblique shock waves require two dimensional flow equations since they are at some arbitrary angle to the flow direction.

For a normal one dimensional adiabatic stationary shock wave bounded by a constant area region, the following derivations and relations will hold. For the moving shock wave case, a reference frame velocity is added Rathakrishnan [2010].

Continuity equation:

$$\rho_1 u_1 = \rho_2 u_2 \tag{2.1}$$

Momentum equation:

$$\rho_1 u_1^2 + P_1 = \rho_2 u_2^2 + P_2 \tag{2.2}$$

Energy equation:

$$h_1 + \frac{u_1^2}{2} = h_2 + \frac{u_2^2}{2} \tag{2.3}$$

The Mach number is determined as a ratio of the shock propagation speed to the local speed of sound, a.

$$M = \frac{u}{a} \tag{2.4}$$

To determine the local speed of sound:

$$a = \sqrt{\gamma RT} \tag{2.5}$$

The enthalpy can be related by:

$$h = \frac{\gamma}{\gamma - 1} RT \tag{2.6}$$

These equations can be manipulated to provide pressure and temperature ratios as well as downstream Mach numbers as follows:

$$\frac{P_2}{P_1} = \frac{(1+\gamma M_1^2)}{(1+\gamma M_2^2)} \tag{2.7}$$

$$\frac{T_1}{T_2} = \frac{(1+\frac{\gamma-1}{2}M_1^2)}{(1+\frac{\gamma-1}{2}M_2^2)} \tag{2.8}$$

$$M_2 = \left[\frac{\frac{2}{\gamma-1}+M_1^2}{\frac{2\gamma}{\gamma-1}M_1^2-1}\right]^{\frac{1}{2}} \tag{2.9}$$

The distance a shock travels for a given duration of illumination of a schlieren light source is:

$$\kappa = Ma\tau \tag{2.10}$$

If the distance κ is too large for a given flow field, the schlieren image will appear blurry and density gradient fields will not be accurately represented. Similarly, if κ is too small, the shock will appear very thin and will not yield much useful information. Light sources with a larger τ would be better suited to shocks with a lower Mach number. More information can be found in section 4.2.1.

2.3 Schlieren Photography

The following reviews of schlieren history, the optical theory and methods involved are largely based on work conducted, by this author, for previous undergraduate work. This section outlines the optical systems employed, common schlieren problems as well as the various optical principles and theory, around which this quantitative analysis revolves.

2.3.1 History

Schlieren were first observed in the 17th century by Robert Hooke and Christian Huygens during experiments using a candle as both a light source and a test subject. Only 200 years later was it rediscovered by Leon Foucault during experimentation with parabolic mirrors and knife edges. August Toepler first observed schlieren in one of his images he captured. The schlieren were formed by the chromatic aberrations in one of his field lenses. However, Toepler did not realize the usefulness of his discovery.

In 1896, Julius Rheinberg was reported to have discovered several colour schlieren techniques which are still in use today. He correctly identified the advantages of colour contrast over

conventional bright and dark field microscopy as well as the colour coding of the magnitude and direction of refracted and diffracted light [Settles, 2001].

Hubert Schardin released his paper, in 1942, on schlieren methods and applications which contained several new and innovate schlieren techniques. Schardin has been described as being the modern pioneer of colour schlieren techniques and in his paper he describes 12 schlieren arrangements, three of which produced coloured images: the prism, lattice filter and colour-background methods.

Post war technological developments required various high speed flow visualizations which led to widespread use of the colour schlieren techniques. More recently, Cords [1968] proposed a new 1-dimensional colour schlieren arrangement. This arrangement led G.S. Settles to develop a two-dimensional colour coding arrangement [Settles, 2001].

2.3.2 Schlieren Systems

There are a number of schlieren system arrangements which have been devised over the years. Each system has its benefits and drawbacks but all are based on Toepler's design principles [Settles, 2001]. The goal of an optical schlieren system is to effectively visualize a schlieren object. A schlieren object may be defined as a region within the field of view, in which, there is a fluid medium with a fluctuating density field.

Modern schlieren systems employ either a lens or a mirror based optics layout. Table (2.1) outlines the benefits and drawbacks of each type of system.

Table 2.1: Benefits and drawbacks for mirror and lens based schlieren systems

Mirror	Lens
Folded, off axis optics	In-line, on axis optics
Difficult to align	Simple in-line optics, easier to align
Off-axis optical aberrations can inhibit image quality	Chromatic aberrations occur in cheaper non-achromatic lenses
Single reflective surface	Modern multi-element lenses have several optical surfaces
Lower cost	Higher cost

2.3.2.1 Lens Systems

Schlieren photography is a highly precise technique often looking at very weak schlieren objects within a flow field thus high quality, sharp lenses should be used. It has been said that the surface of lens based optics should not deviate by more than half a wavelength of light over the diameter of the lens.

Toepler's single field lens arrangement, figure 2.5, is an example of one of the early schlieren setups. It is important to note that the schlieren object is not traversed by parallel light.

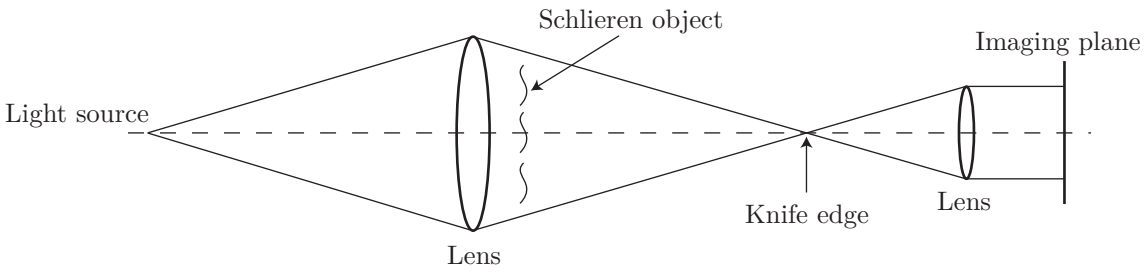


Figure 2.5: Toepler's single lens schlieren system

This is a disadvantage if the schlieren object is 2-dimensional as light will be distorted and the resulting image will not be an accurate representation of the true schlieren object.

The problem of non-parallel light in the test section is solved by introducing an additional lens into the system, placed after the first primary lens but before the knife edge. Figure 2.6 shows the test section and schlieren object being traversed by parallel light [Settles, 2001].

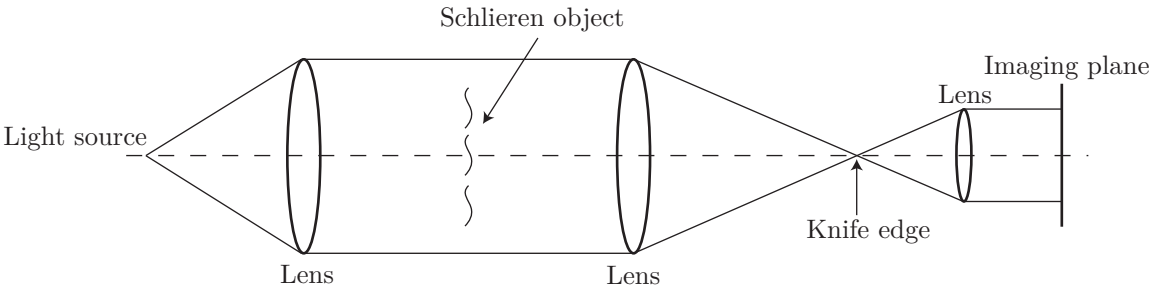


Figure 2.6: Dual lens parallel light schlieren system

2.3.2.2 Mirror Systems

Schlieren systems which use mirrors are most often arranged in the fashion illustrated in figure (2.7). The arrangement is commonly known as a Z-Type two mirror schlieren system and will be the preferred method of schlieren setup for this purposes of this dissertation.

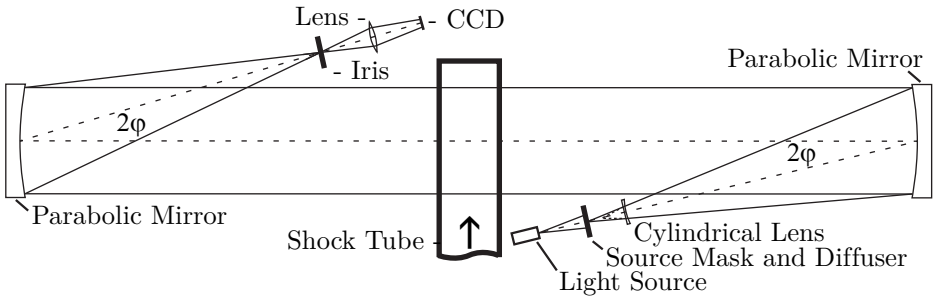


Figure 2.7: Z-type schlieren arrangement

The mirrors used are either spherical or parabolic and their alignment with the light sources and imaging planes are based on the Herschellian method of tilting the mirror off-axis to

gain access to the focused image. It is clear that the mirrors are tilted off axis in opposite directions; this is done to reduce a schlieren problem known as coma. The arrangement leads to a few optical problems although the effects of the problems can be minimized with certain adjustments and optics. See section 2.3.3 for more details on the problems and how to rectify them.

As in the improved lens based schlieren system, the 2 mirror system generates parallel light passing through the test region. A large benefit of using mirrors over lenses is that the test regions field of view is larger for a given cost than that of lenses.

It has been suggested that the distance between the two mirrors be approximately twice the mirror focal length. The reason for this is to provide a large enough area between the two focal points to place or house the test section [Settles, 2001].

2.3.2.3 Extended light sources

An extended light source is simply a light source with finite dimensions, as is used for the colour schlieren setup described herein. The source masks, placed at the focal length of the primary schlieren mirror, have a finite diameter and thus generate the problem of non-parallel light passing through the test section. It is possible to imagine each point on the source mask as a single point source of light. These individual point sources of light are emitting a cone shaped bundle of rays which each strike the mirrors at slightly different angles, thereby causing the non-parallel light to traverse the test section.

Figure 2.8, based on the dual field lens method schematic of an extended light source by Settles [2001] and generated by Rayoptik, illustrates the effects of an extended light source. It can be seen that the dashed and solid lines at the extreme edges of the test section are not running parallel since they emanate from the extremities of the source mask. It may also be noted that the focal points of the two bundles of rays after the second mirror do not coincide.

The major influence that this phenomenon has on a schlieren system, is the ability to control the depth-of-focus. It is also important to make sure the source mask center is positioned as accurately as possible on the optical center line to avoid enhancing the non-parallel light effect. Furthermore, the light falling on the cut-off knife edge is a composite virtual image of the source mask. This forms the basis of the schlieren method as the image which falls on the cut-off knife edge, or iris diaphragm in this case, contains the information regarding the test section light refractions. Figure 2.13 illustrates how this information is extracted and used to compile a schlieren image [Settles, 2001].

2.3.3 Schlieren Problems

A number of inconveniences arise when setting up schlieren optics systems. Due to the nature of the schlieren method, the slightest misalignment, optical imperfection or incorrect

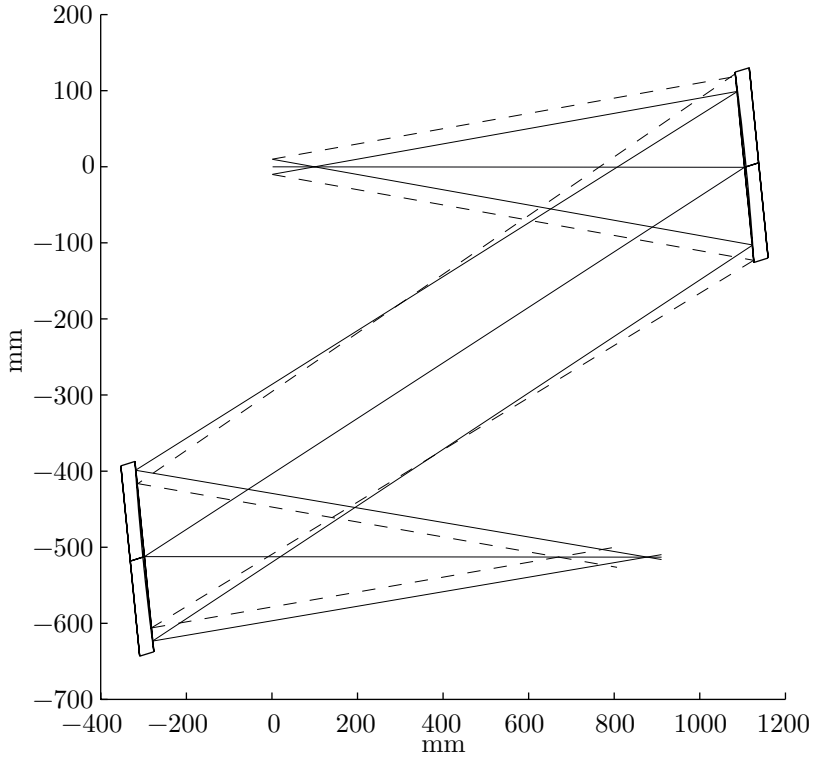


Figure 2.8: Schematic showing the effects of an extended light source

apparatus adjustment impacts the quality of the captured images. Thus, it is important that the optics system is of a high enough quality to yield images which are to be quantitatively analyzed.

The layout of the schlieren system results in various optical aberrations. The first such aberration is known as astigmatism. The word astigmatism is derived from the Greek words meaning 'without' and 'spot' or 'mark'. It refers to the loss of a focal point, in this case due to the off axis rotation of the 2 parabolic mirrors. Considering a bundle of parallel light rays moving along the optical axis and striking a rotated parabolic mirror, the reflected rays will not all come to a common focal point. Two focal points will be generated, namely the tangential and sagittal focal points. The focal points lie in either the tangential (vertical) or sagittal (horizontal) planes respectively. The difference between these focal points is known as the astigmatic difference. This distance is influenced by the focal length of the mirror and the degree of the off axis rotation [Zhang, 2010].

The severity of the astigmatism present in an optical system is related to the distance between the two foci and can be represented by the geometric formula, equation (2.11).

$$\alpha = \frac{f \sin^2 \varphi}{\cos \varphi} \tag{2.11}$$

And this can be simplified in the limit as φ tends to a small angle,

$$\alpha = \frac{\phi^2}{4f} \tag{2.12}$$

From equation (2.12), it is clear that for a given mirror diameter, a larger focal length is desired to reduce the astigmatic difference [Settles, 2001].

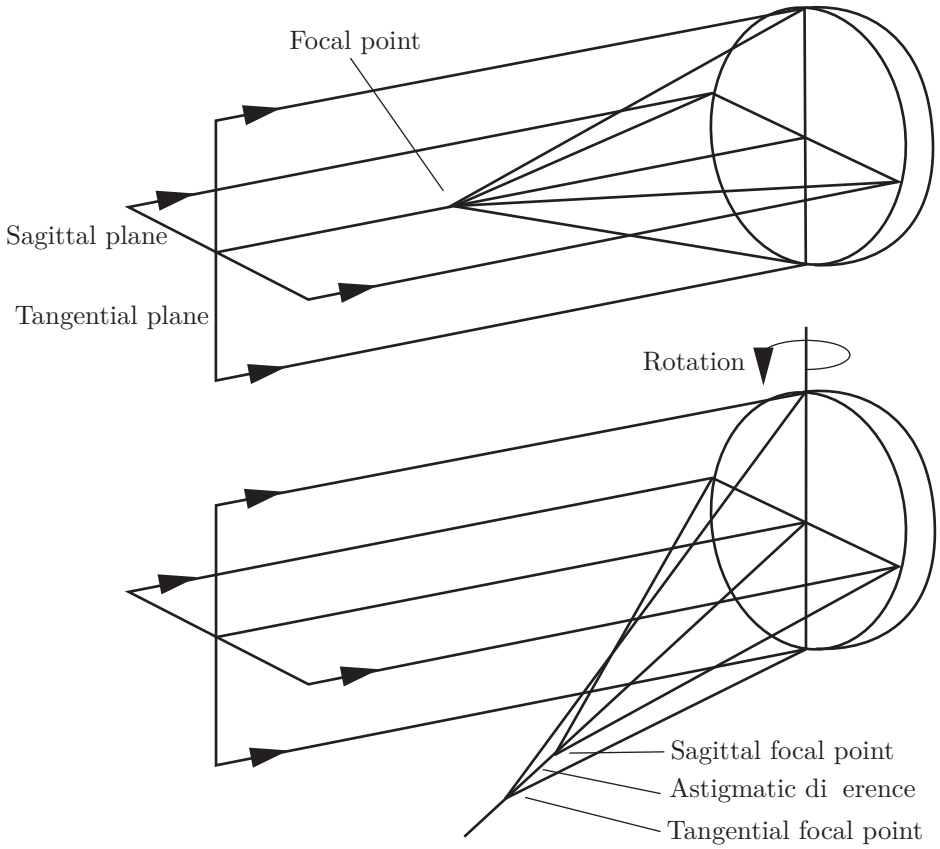


Figure 2.9: Schematic representation of the problems due to astigmatism

Astigmatism will always be present in an optical system however it is possible to reduce its effects. If the effects are not reduced, the quality of images and hence the schlieren system can be severely compromised and result in a system which is not qualitatively useful, let alone quantitatively.

Studying figure 2.13, one finds the focal points are separated by the astigmatic difference along the optical axis. Taking into account the arrangement of the optical system, it is possible to use corrective measures to significantly reduce the astigmatic difference. The two separate focal points are positioned in the region where the source mask for a colour schlieren system should be placed. Using a plano-convex cylindrical lens on the mirror side of the source mask, it is possible to bring the focal point of the primary schlieren mirror back to a single point.

A plano-concave cylindrical lens works by altering the light paths in one plane only. For the present system, the sagittal focal point is moved forwards while the tangential focal remains

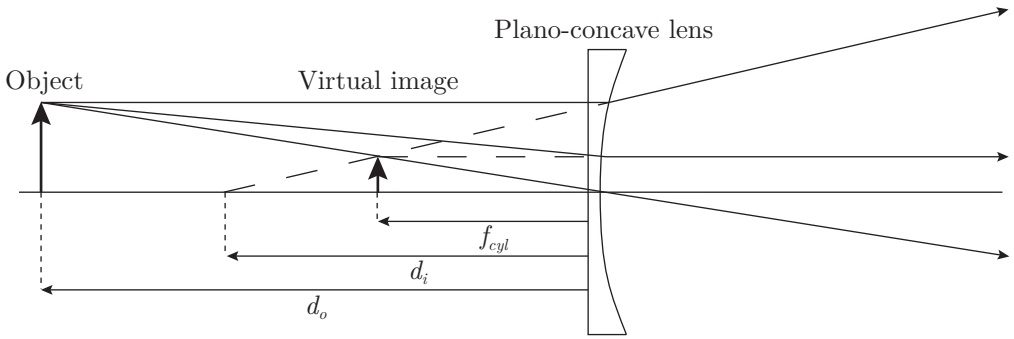


Figure 2.10: Ray trace schematic diagram for the cylindrical lens in plan view

in one position. This requires the cylindrical lens to be placed such that it influences the sagittal plane only. The tangential plane is to pass through the lens with no light ray alterations.

The source mask is placed at the tangential focal point of the parabolic mirror, shown as the object in figure 2.10. The positions of the cylindrical lens along the optical axis, mirror focal length and schlieren system angle all have an influence on the dimensions and position of the virtual image.

The thin lens equation relates the formed focal points to the focal length of the lens:

$$\frac{1}{d_o} + \frac{1}{d_i} = \frac{1}{f_{cyl}} \tag{2.13}$$

This can be re-arranged to determine the distance of the virtual image from the lens:

$$d_i = \frac{d_o f_{cyl}}{d_o - f_{cyl}} \tag{2.14}$$

Equations (2.11) and (2.14) can be equated together to determine appropriate optical element positions:

$$d_o + d_i = \alpha$$

$$d_o = \alpha - \frac{d_o f_{cyl}}{d_o - f_{cyl}}$$

Making the distance from the source mask to the lens the subject of the formula yields:

$$d_o = \frac{\alpha \pm \sqrt{\alpha^2 - 4 f_{cyl} \alpha}}{2} \tag{2.15}$$

This equation indicates the position along the optical axis from the source mask which the cylindrical lens should be placed to most efficiently account for the astigmatic difference. Two values are obtained from the above equation; however, it is the negative value which is desired as this ensures the virtual image falls on the same side of the lens as the object. Equation (2.14) can be used to determine the position of the virtual image along the optical axis. The magnification of the object is determined by:

$$m = -\frac{d_i}{d_o} \tag{2.16}$$

The magnification is used to determine the distortion characteristics which need to be applied to the source mask to obtain the correct aspect ratios. The cylindrical lens causes the width of the virtual source mask to be reduced and thus the width of the real source mask needs to be extended for this distortion effect. The maximum width of the source mask should be specified such that all the light passing through the mask strikes the cylindrical lens. This dimension is then multiplied by the magnification factor to give the corresponding height of the source mask. More on this and the design of the source mask in section 4.1.3.

The second optical aberration which has the potential to destroy image quality is known as coma. The name is derived from the word "comet" since it induces a comet like smear of non-focus in the imaging plan. The aberration, caused by the tilting of the schlieren mirrors off-axis, results in light striking the mirrors surface not forming a point like focal point but rather a focal line with varying light intensity and spot size. This phenomenon, represented in figure (2.11), has been generated by an open source ray-tracing script, compiled in Matlab, called RayOptik. Further information and computational ray-tracing can be found in section 4.6.

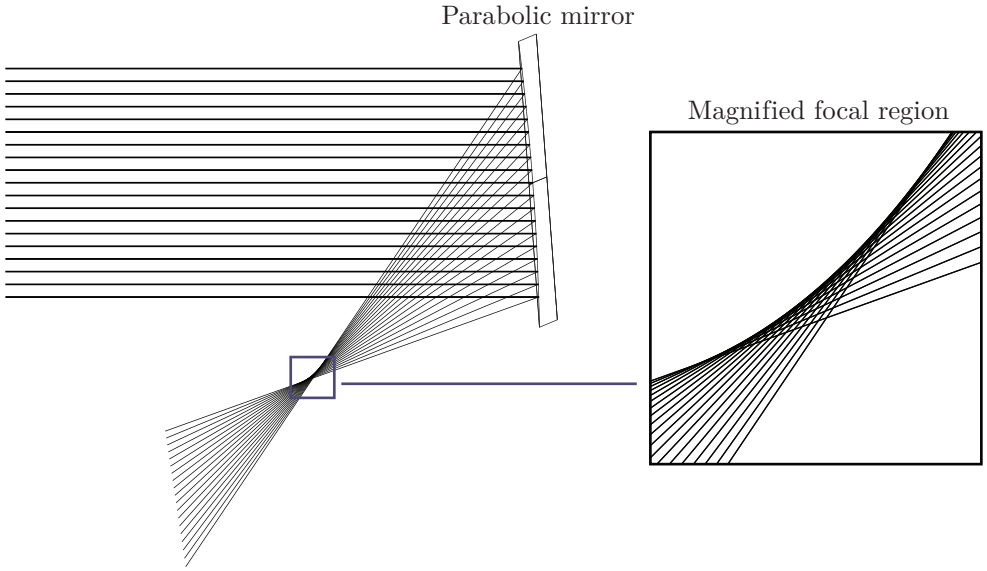


Figure 2.11: Schematic representation of the aberration due to Coma

Although it seems like the focus of the primary mirror converges in one point, enlarging the focal point illustrates a degree of non-focus. A region of higher light intensity would

exist on the side towards the optical axis, blurring would occur outwards and away from the axis. The geometric details of the above arrangement is negligible, the images serve only to illustrate the effect [Settles, 2001].

Coma, unlike astigmatism, is readily solved by simply counter-rotating the schlieren mirrors off-axis to form the typical Z-type configuration. It should be pointed out that if the mirrors are not counter rotated, the effects of coma are doubled rather than nullified. Similarly, this aberration is directly proportional to the angle of the schlieren system as well as inversely proportional to the focal lengths of the mirrors. Thus it is desired to reduce the schlieren angle and use large focal length mirrors to keep this optical aberration from reducing image quality. It should be noted that all optical components, if more than one is used, should be identically specified [Settles, 2001].

2.3.4 Elemental Derivations

The human eye is not able to discern phase differences within a light beam; we can only readily see amplitude and contrast. Schlieren techniques allow us to distinguish these phase differences and thus determine amplitude and, with appropriate equipment, direction.

Light will propagate uniformly through a homogeneous medium, which is evident in everyday life. If this were not the case, it would be incredibly difficult to do anything because we would not know exactly where anything was in physical space. We would have to rely simply on touch alone to be able to locate ourselves in space. However, we can spot phenomenon in everyday life that the schlieren technique is based entirely on. For instance, if one looks over the roof of a car that has been parked in the sun for a while against a discernible background, one can clearly see the light being refracted over the surface of the roof. Similarly; mirages or the twinkle in the stars occurs because of light being 'bent' as it passes through inhomogeneous media.

Thus, we can conclude that light must slow down upon interacting with transparent media. The ratio of the universally known speed of light, $c = 3 \times 10^8 m/s$, to the speed of light in the transparent media, c, is known as the refractive index, n.

$$n = \frac{c_o}{c} \tag{2.17}$$

For air and other gasses, there is a simple relationship between the refractive index and the gas density ρ.

$$n - 1 = k\rho \tag{2.18}$$

The Gladstone-Dale coefficient, k, varies from around $0.1 cm^3/g$ to $1.5 cm^3/g$. For air, $k = 0.23 cm^3/g$ at standard temperature and pressure. The density of the media in question can

also be related by the ideal gas equations, provided that the temperature and pressure do not vary too greatly from the ambient atmospheric conditions.

$$\rho = \frac{P}{RT} \tag{2.19}$$

Where the specific gas constant for dry air is $R = 287.15 J/kg.K$

It should also be noted that the Gladstone-Dale coefficient increases slightly with an increase in wavelength. Thus the refractivity is higher for higher wavelengths so disturbances would be more visible using infrared light as opposed to visible light. This may prove to be a useful technique when experimenting with media with very low density fluctuations.

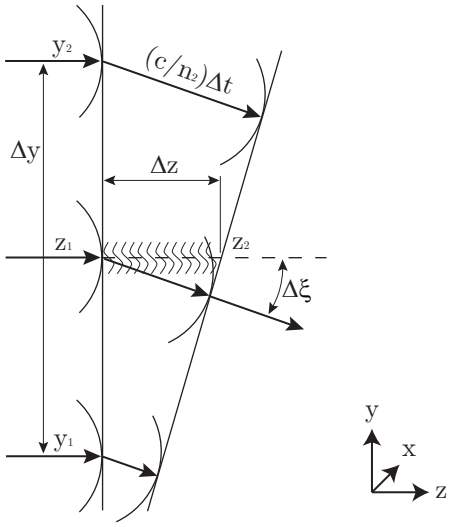


Figure 2.12: Diagram of elemental light refraction by a density gradient

The relation of the curvature of a refracted ray to the magnitude of the corresponding refractive index can be derived using the schematic representation shown in figure 2.12. The derivation makes use of the following assumptions:

- The test section is exposed to a uniform parallel illumination in the x-y plane with no change in illumination in the z plane.
- Within the schlieren object, the displacement of a light ray from its rectilinear path is negligible.
- No changes in gradient in either the x or z directions, $\frac{dn}{dx} = 0$ and $\frac{dn}{dz} = 0$.
- Only a negative vertical refractive-index gradient, $\frac{dn}{dy} < 0$, in the y direction between z_1 to z_2.

From figure 2.12, it can be seen that a planar wave front of light is initially vertical upon passing through z_1. As the wave travels through the schlieren object from z_1 to z_2, it

traverses the distance Δz in a differential time Δt and is refracted through and angle of $\Delta\xi$. Thus we can write:

$$\Delta\xi = \frac{c_o/n_2 - c_o/n_1}{\Delta y}\Delta t \tag{2.20}$$

And the differential time can be further expressed as:

$$\Delta t = \Delta z \frac{n}{c_o} \tag{2.21}$$

Combining these equations yields:

$$\Delta\xi = \frac{n}{c_o}\frac{c_o/n_2 - c_o/n_1}{\Delta y}\Delta z \tag{2.22}$$

Simplification results in:

$$\Delta\xi = \frac{n}{n_1 n_2}\frac{(n_1 - n_2)}{\Delta y}\Delta z \tag{2.23}$$

The term n/n_1n_2 can be simplified to $1/n$ in the limit as Δy tends to zero. Letting all the finite differences approach zero, we obtain:

$$\frac{d\xi}{dz} = \frac{1}{n}\frac{dn}{dy} \tag{2.24}$$

Since ξ is a very small angle, it can be approximated to the slope of the refracted ray. Implementing this and accounting for other refractive-index gradients we obtain the relationship between the curvature of the refracted ray to the magnitude of the refractive index gradient:

$$\frac{\partial^2 y}{\partial z^2} = \frac{1}{n}\frac{\partial n}{\partial y} \tag{2.25}$$

A similar expression can be generated for the refraction in the x direction:

$$\frac{\partial^2 x}{\partial z^2} = \frac{1}{n}\frac{\partial n}{\partial x} \tag{2.26}$$

Now, to obtain the angular ray deflections in the test section we integrate equations 2.25 and 2.26 to obtain the following:

$$\xi_y = \frac{L}{n_o}\frac{\partial n}{\partial y} \tag{2.27}$$

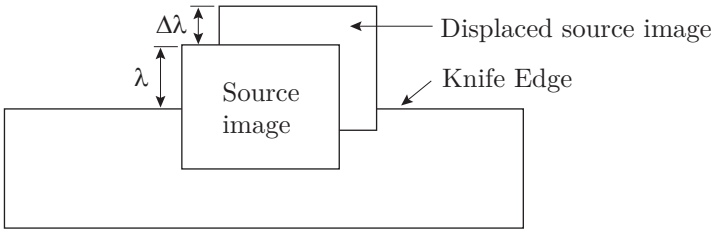


Figure 2.13: Schematic representation of a displaced source image

$$\xi_x = \frac{L}{n_o}\frac{\partial n}{\partial x} \tag{2.28}$$

Figure 2.13 shows a rectangular source image half cut off by a knife edge with a height of λ remaining un-obscured. If there is a light refraction within the test section, a weak image will be displaced vertically with its un-obscured height now becoming $\lambda + \Delta\lambda$ thereby allowing additional light to fall on the imaging plane behind the knife edge.

The initial amount of light cut-off, which is essentially the height λ, sets the background illumination level on the imaging screen. So, from the above figure, it can be seen that if the refractive index in the test section causes a light refraction in the opposite direction i.e. downwards, then the image in the imaging pane will become darker.

Thus it can be said that the image illumination level is linearly proportional to the amount of knife-edge cut-off. Thus:

$$\Delta\lambda = f_2\xi_y \tag{2.29}$$

Combining equations (2.18), (2.27) and (2.29) we obtain an expression for the density gradient in the y-direction as follows:

$$\frac{\partial\rho}{\partial y} \cong \frac{\Delta\lambda}{kLf_2} \tag{2.30}$$

Integrating equation (2.30) in the y direction, we obtain the density distribution function assuming we know the flow density at some reference point:

$$\rho(y) \cong \frac{1}{kLf_2}\int_{y_2}^{y_1} \Delta\lambda(y)dy + \rho_{ref} \tag{2.31}$$

This derivation allows monochromatic intensity images to be used to determine the approximate density distribution throughout the image [Settles, 2001].

These derivations have been shown for a simple monochromatic schlieren system using a single knife edge cutoff. The schlieren setup for the present study operates on similar

principles, however an iris diaphragm is used in place of the single knife edges to allow for omni-directional sensitivity.

2.3.5 Broader Derivations

The following broader derivations pertain to the test section interaction with refracted light and outline the methods of attaining density gradient information in relation to angular light deflection.

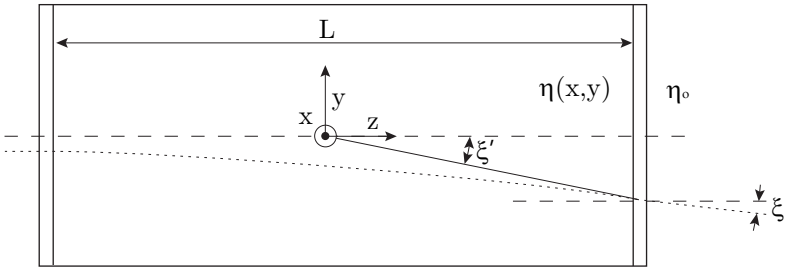


Figure 2.14: Schematic image of the test section

Invoking the Gladstone-Dale relationship and assigning each point in the (x, y) plane a corresponding refractive index and density we have:

$$\eta(x, y) = 1 + k\rho(x, y)$$

Deriving both sides with respect to y, we arrive at:

$$\frac{\partial n(x, y)}{\partial y} = k\frac{\partial \rho(x, y)}{\partial y} \tag{2.32}$$

Snells law:

$$\eta_o \sin\xi = \eta(x, y) \sin\xi^{'}$$

Assuming small angles and working in the y-direction only we arrive at:

$$\eta_o \xi_y = \eta(x, y)\xi_y^{'} \tag{2.33}$$

Snells law will apply to a light ray deviation in the (x, y) plane only and will not take into account further deviations caused by density gradients along the z-axis. Thus integrating equation (2.33) results in:

$$\xi_y^{'} = \int_0^L \frac{1}{\eta(x,y,z)} \frac{\partial \eta(x,y,z)}{\partial y} dz$$

For $n \neq n(z)$

$$\xi_y^{'} = \frac{1}{\eta(x,y)} \frac{\partial \eta(x,y)}{\partial y} \int_0^L dz$$

$$\xi_y^{'} = \frac{L}{\eta(x,y)} \frac{\partial \eta(x,y)}{\partial y} \tag{2.34}$$

From Snells law and substituting equation (2.34) we get:

$$\eta_o \xi_y = \eta(x,y) \xi_y^{'} = \eta(x,y) \left[\frac{L}{\eta(x,y)} \frac{\partial \eta(x,y)}{\partial y} \right]$$

Which simplifies to:

$$\eta_o \xi_y = L \frac{\partial \eta(x,y)}{\partial y}$$

$$\xi_y = \frac{Lk}{\eta_o} \frac{\partial \rho(x,y)}{\partial y} \tag{2.35}$$

Equation (2.35) describes the angle of light deflection in the test section with a finite width Settles [2001].

2.4 Light Sources

This section outlines the types of light sources which may be employed in a schlieren system. Constraints and performance requirements are discussed briefly.

2.4.1 Methods of illumination

The method of illumination for a schlieren system depends inherently on the type of study being undertaken and the equipment available. Specific combinations of equipment will have different light demands. If a high speed camera is available, a continuous light source may

be employed or perhaps even a standard SLR camera flash, triggered to flash at a predefined moment in time. The latter option allows a number of settings to be adjusted to suit the optical setup and the flow regime being visualized.

Due to the expense of high speed cameras, a more conventional method of using a SLR camera might be used. This method simply requires a high intensity pulse or flash of light to be triggered at precisely the right time to freeze a given flow at that instant. This method may involve more electronics to trigger the flash than a continuous light source but does not require expensive photographic equipment.

2.4.1.1 Xenon flash lamps

Pulses of light may be generated by a number of methods. Perhaps the most common method is by way of an electrical arc jumping between electrodes. Xenon flash lamps operate by passing a high voltage from a low capacitance capacitor between electrodes in the presence of a high purity ionizing gas, in this case xenon gas.

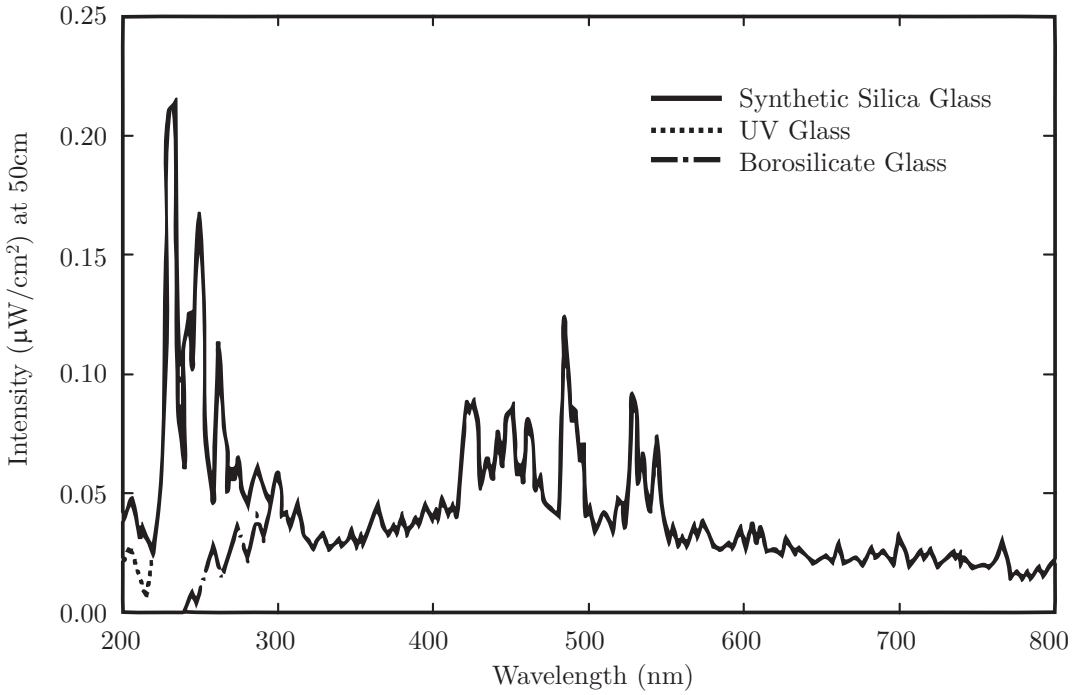


Figure 2.15: Xenon spectral distribution Hamamatsu [2005]

The incoherent light produced is extremely intense across the light spectrum from the UV range through to the infrared range. Figure 2.15 illustrates the spectral range and relative intensities emitted by a Hamamatsu xenon flash lamp. Bearing in mind the visible spectrum ranges from approximately 450nm through to 650nm, there is a large degree of energy wasted in the form of non-visible electromagnetic radiation. Arc stability, the repeatability of the arc traversing the same path within the bulb, has the potential to influence images taken with such a device, however, Hamamatsu claims a significant improvement of arc stability over conventional flash lamps.

Hamamatsu does not indicate light intensity outputs with any values comparable to LED's, constant light sources or boot flashes thus any comparisons between the devices are inherently difficult. The most appropriate method is to simply test each item and compare results.

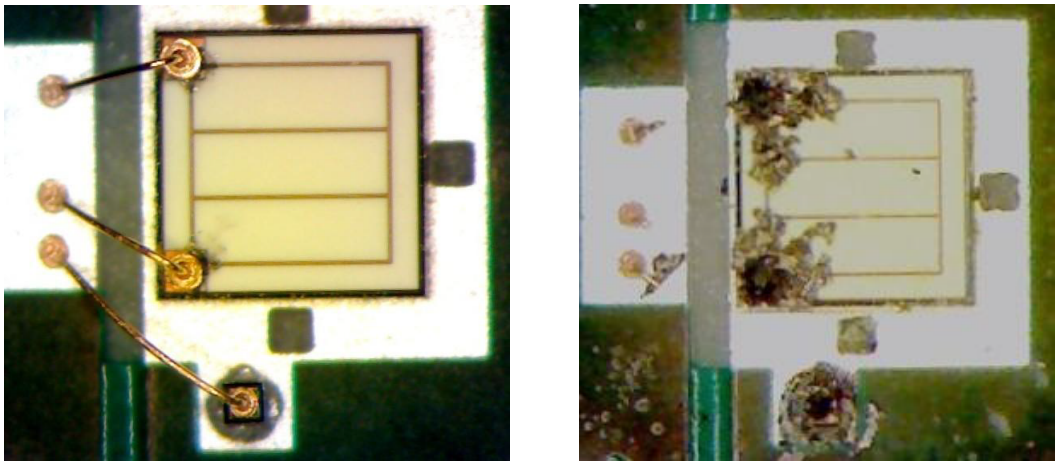
2.4.1.2 LED pulsing circuits

Light Emitting Diodes (LEDs) were introduced in the 1960's as low power, low intensity red indicator lights. Over the years, the technology they are based on has moved forwards very rapidly and LED's are now are finding their way into numerous lighting applications such as televisions, display boards, interior lighting, torches, automotive lighting etc. There are a number of advantages and disadvantages of using LED's for everyday applications however, for rapid pulsing high intensity lighting applications, LED's are making their way to meet or supersede the specifications of conventional methods of rapid pulse generation.

Very few organizations are marketing such systems and at the inception of this dissertation, no private company was in fact developing such light sources. It has been said that LED technology is advancing according to Moore's Law which, amongst other things, implies that power output, efficiency and availability are inversely proportional to the cost. Haitz and Kish [1999] suggests that LED technology has the potential to replace all other lighting requirements given that the correct research and development is undertaken.

Technicalities involving LED light sources are relatively new and the technology behind their operation is constantly adapting to suit new niches. There have been few studies on how over-current conditions are effecting the LED's performance, lifespan and illumination. Once such study conducted by LED manufacturer, Cree [2011b], discusses three types of electrical over-current; Single pulsed events, Repetitive pulsing and Ripple effects.

The most pertinent aspect of this study is the single pulsed events as this relates to the type of LED illumination used by the driving circuitry. Single pulsed events or *Electrical Over-Stress* (EOS) may typically be associated with large in-rush currents or transient electrical surges into the LED diode. *Electrostatic Discharge* (ESD) is common and most electronics are fairly sensitive to this type of EOS. The main factors involved with an LED being able to withstand an EOS event is the current carrying capacity of the LED and its internal connections. The type of electrical pulse is also a critical factor as to whether the LED will be able to withstand the current influx or whether catastrophic failure would occur Cree [2011a].



(a) (b)

Figure 2.16: LED electromigration, Cree [2011b]

As current passing through the LED connections increases, the amount of heat generated increases and thus the current should be kept to within the limitations of the interconnections thermal capacity. If this is not the case, the current causes the conductors to melt and fuse as well as the insulating material to break down. This results in the materials forming the interconnections to subtly change position. Electromigration is the term used to describe this translocation of moving electrons to nearby ions, causing them to dislocate from their original lattice positions. This phenomenon may be seen in figure 2.16 which illustrates electromigration [Cree, 2011b].

A more in depth problem of pulsed LED operation is chromaticity shifting. As the LED forward current increases, colour coordinates begin to shift on the CIE 1931 colour space, resulting in an increase in the *Correlated Colour Temperature* (CCT). See Cree [2011b] for more details on this phenomenon.

2.4.1.3 Constant light sources

A constant light source is generally used for two areas of schlieren photography; to setup an optics system accurately; and to provide enough light for high speed camera capturing systems. As LED's improve in efficiency and luminous output while decreasing in cost, they are rapidly becoming more viable for the use as constant light sources.

Halogen bulbs of varying power output are readily available and relatively cheap systems can be setup to provide constant light sources. It is however, important to note that halogen bulbs produce a large amount of infrared radiation in comparison to LED's. This makes them largely inefficient and caution must be taken when confining the bulbs or positioning them next to heat sensitive optical components such as photographic slides.

2.4.1.4 Boot flashes

This method of illumination is typically used with a schlieren system which requires a large amount of light, perhaps due to loss of scattered light, insensitive camera equipment, demanding optical designs or a combination of these.

A boot flash is a powerful extension to the built in flash on many SLR cameras. The flash can operate in conjunction with or separate from the camera body. The latter method of the flash being separate from the camera requires a coaxial cable from the camera, or trigger source, to the flash body. High quality professional flashes have a number of settings which modify their light intensity output as well as focusing positions. There are typically diffusing screens built in which allow the more even dispersion of light.

The flashes operate using gas filled discharge tubes in much the same way a flash lamp works however conventional camera flashes are not constrained by the duration of the light output. At full power, the Canon EX430 has an even level of illumination for a duration of approximately 1ms. This means as many as 1000, $1\mu s$ exposures may be captured for a given flash. A high speed camera is the only way to capture such images. More information on the boot flash and high speed camera can be found in section 5.3.

A number of benefits are apparent when using a system of this nature. The system essentially captures the flow regime, shock waves in particular, at every state of their existence before leaving the test section. This drastically improves repeatability considerations as a single test may prove to provide all the information that is required. It allows comparisons to be made between frames and the motion of the fluid system immediately becomes apparent.

2.4.2 Requirements

As was discussed in section 2.2.2 the duration of the illumination of a moving shock wave is critical in order to obtain a crisp sharp image. If the light source duration for a given shock wave is too large, too much blurring will occur and density gradients will not be accurately represented. However, if the illumination bandwidth is too narrow, the shock waves will appear very thin. Recalling section 2.2.1, it was determined that the width of a shock wave is in the region of $10^{-4}mm$. Thus, the narrower the bandwidth of illumination, the closer the shock will appear to be this width. A discussion of the optical requirements can be found in the design development section under section 4.2.1.

2.5 Quantitative Methods

This section aims to outline various quantitative methods of schlieren visualization.

2.5.1 CCS & BOS

An assessment into quantitative schlieren methods was undertaken by Elsinga et al. [2003]. A comparison was made between a *Calibrated Colour Schlieren* (CCS) system and a *Background Orientated Schlieren* (BOS) system. Both are described as 2-dimensional systems inferring their ability to analyze density gradients within a 2-dimensional flow field.

CCS utilizes a square cutoff mask, with graded colours in order to encode light ray deflections. The source comprises of a square piece of ground glass diffuser of variable size. The CCS system is assembled with a Z-type layout, however it uses mirrors at the focal lengths of the two primary mirrors to allow a smaller system angle to be used.

The system is calibrated by recording the colour ratios of each pixel for a variety of filter positions. The source mask is translated 25 times in both the x and y directions and the corresponding images are recorded. Various specified pixels are then compared and the colour ratios result in a complex calibration polynomial which allows the deflection angles to be determined for each pixel.

CCS makes use of a reference image, taken with no density field in the test section. This reference image is used to determine the reference deflection angles and these angles are then subtracted from the resulting angles when a schlieren object is present. Once the deflection angles are known, an equation similar to equation 2.35 is used to determine the density gradients and, following that, integration of the results provides the density field.

It was found that the density gradients resulting from the CCS measurements showed large fluctuations due to camera noise however the density which was determined agreed with theory. The CCS system assumes a 2 dimensional flow field while in reality, a 3 dimensional flow field exists. This assumption, together with the boundary layer effects on the test section glass were found to cause differences between measurements and theory [Elsinga et al., 2003].

BOS , while not specifically related to the current dissertation topic, was similarly analyzed for its quantitative potential. BOS utilizes a computer generated random dot pattern which is placed over the rear optical tunnel window and illuminated from behind by a lamp. Images are then taken with and without schlieren objects within the test section and then compared by an advanced cross correlation technique, originally designed for for PIV systems [Elsinga et al., 2003].

Camera noise was not observed in the BOS system as was found in the CCS system, however, a lack of resolution lead to inaccurate results. The resolution was limited by the need for cross-correlation techniques and the fact that the schlieren object in BOS systems are out of focus. The BOS system was found to have a higher dynamic range [Elsinga et al., 2003].

2.5.2 Rainbow & Bulls-Eye schlieren

The following two techniques are based on very similar principles but they may, however, be configured to produce slightly different information depending on which experimental data is required. The original concepts of both variations were developed by Rheinberg in 1896 and also go by the name of ring and band lattice respectfully [Settles, 2001].



(a) (b)

Figure 2.17: Colour schlieren dissection technique. (a) Rainbow method; (b) Bulls-Eye method

Rainbow schlieren is based on the dissection technique and is typically uni-directional. The source mask comprises a number of strips of coloured gelatin filters or colour transparency, see figure 2.17 (a). They are arranged in such a way so as to produce as many different hues of colour in the imaging plane. Up to eleven hues may be represented however, only two pure colours will be produced by the innermost segments on the source mask. Since the system is uni-directional, the source and cutoff apparatus will need to be rotated to capture density gradients in other directions [Kleine, 2000].

This method allows the magnitude of the density gradient to be determined by analyzing the changing hues in the image. Many applications only require sensitivity in a single plane such as temperature analysis of a plume, Ibarreta and Sung [2000] and visualization of an oscillating helium jet, Leptuch and Agrawal [2003].

Bulls eye schlieren operates on exactly the same principle as Rainbow schlieren however instead of a uni-directional slit, a set of coloured rings in employed which allows omni-directional sensitivity. Figure 2.17 (b) illustrates the arrangement of the annular slits. This method allows density gradient magnitude to be determined for all density gradient directions within the test section.

Wolter (1950) produced a schlieren system with colour coded sectors that produced enough contrasting colours to code both density gradient direction and magnitude by using birefringent quartz plates and cross polarizers [Settles, 2001].

The bulls eye method allows investigations into omni-directional insensitive systems such as combustion chambers, Oren et al. [1988] or spherical flames, Feikema [2004].

2.5.3 Calibration Lens

It is possible to determine the performance of a given optical setup in terms of sensitivity, dynamic range and focus by placing an object of known refractive index within the test section. Ideally, the object should have a range of refractive indices which would allow the dynamic range of the setup to be determined. The data determined by this initial testing of the optics system may be used as a calibration to determine approximate values within the flow field. A large focal length plano-convex lens, as suggested by Schardin [1942], placed into the test section provides an object with varying refractive index as well as a visual indication of the optical setup [Kleine and Gronig, 1991].

The calibration lens would be placed into the test section before a test is run to finely tune and adjust the position of the iris diaphragm cut off. A calibration image may be taken as a record of the settings used before and after a test to prove repeatability of the optical setup.

The specifications of a given calibration lens will vary according to the desired specifications of the experimental setup. A larger focal length would yield less light deflection and correspondingly return lower density gradient magnitudes.

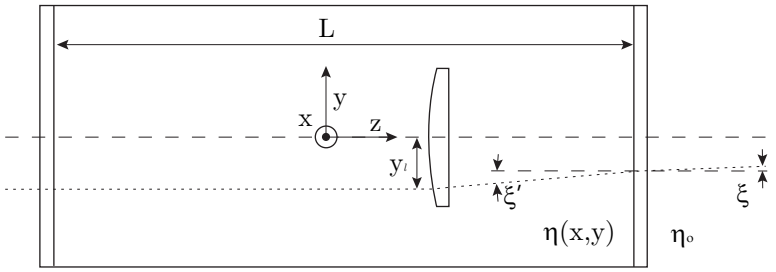


Figure 2.18: Calibration lens in the test section

Examining figure 2.18, it is possible to equate the angular deflection of a ray of light to the radial position it passes through a given lens and the focal length of that lens.

$$\tan \xi = \frac{y_l}{f} \tag{2.36}$$

From equations 2.36 and 2.35

$$\frac{\partial \rho(x,y)}{\partial y} = \frac{y_l \eta_o}{Lkf} \tag{2.37}$$

Thus, it can be inferred that the density gradient, for any given direction, is a function which varies linearly with the radius of the calibration lens.

When placing the calibration lens into the test section, care should be taken to orientate the curved surface of the lens towards the light source to reduce any optical aberrations and to improve lens focusing.

2.6 Digital Imaging

Digital image processing drastically affects the process of calibration and understanding the content of digital images. Since the inception of digital imaging, the turnaround time from capturing the images to being able to view the images has dropped significantly. This not only improves the efficiency of research but enhances the quality of processed data and opens doors to new research possibilities.

Due to the nature of the digital image, additional complexities and variables are introduced into the equation, however it is possible to exploit these for improved control over the final outcome.

2.6.1 Digital image recording

The digital image sensors used to capture light and convert the data into a digital format vary from camera to camera. Typically there are two types, namely a *Charged-Coupled Device* (CCD) and a *Complementary Metal Oxide Semiconductor* (CMOS) sensor. The sensors vary in size and are covered in microscopic light sensitive devices called photosites. Within each photosite is a photo diode, this component converts the light into an electrical charge, the stronger the light, the greater the charge. The photo diodes, by themselves, cannot distinguish colour and therefore a *Colour Filter Array* (CFA) is placed over the entire array of photo diodes. The CFA is made up of a mosaic pattern of red, green and blue squares. The most common pattern, called the Bayer pattern, was invented by a Kodak technician. Each photosite then has the ability to record a red, green or blue value. The camera's processors are then required to 'de-mosaic' and interpolate the data to generate a final image which could contain 16.7 million different colours. Typical digital SLR sensors are typically 23.5mm x 15.7mm however advanced SLR's have full frame sensors and are the same size as 35mm film, 36mm x 24mm [Luck, 2009].

Both types of sensors are manufactured in similar ways however the procedure of recording the digital data collected by each photosite is different. The photosite rows in a CCD are connected or "coupled" to one another and thus the data from each photosite is passed along the chain to one corner of the sensor array, read and then deleted. From the sensor, the values are then sent to an analogue/digital converter and stored [Luck, 2009].

In a CMOS chip, each photosite is equipped with its own amplifiers and circuitry in such a way that the data can be read directly from the photosite itself and then passed to the analogue/digital converter. This means the data does not need to be passed from site to site to be read [Luck, 2009].

High quality digital image data, in the form of drawings or photographs, needs to be stored in a practical and efficient manner. The most common method of storing digital image data is in the form of a bitmap. A bitmap is an array of thousands of dots called picture elements, pixels for short. Each pixel's colour is represented by a digital combination of 0's and 1's

and the total number of bits used for each pixel is called bit depth [Morley and Parker, 2009].

A monochrome image, as the name suggests, is made up of only two colours, black and white. In the digital form, the colour black would be represented by 0 and white by 1. This means only 1 bit of data is used to store each pixels colour. This is the most basic image type however its simplicity provides powerful computing possibility such as blob detection, image analysis, motion detection and facial recognition to name a few [Morley and Parker, 2009].

A grayscale image is the next enhancement to a monochrome image. Again, as the name suggests, the image is made up of shades of grey. Each pixel is now not represented by 1-bit but by 8-bits. This means that 256 shades of gray can be produced for each pixel [Morley and Parker, 2009].

A colour image is similar to a grayscale image however each pixel now has three grayscale channels as opposed to a single channel. Each of the three channels now represents the colour constituent of the image, *Red, Green, Blue* (RGB). 8-bits for each channel yields a 24-bit true colour image with 2563 or 16.8 million colours. It is possible to have a greater bit-depth however unless the image is being enlarged significantly, the human eye is not able to discern much difference. Images up to 48-bit are possible with the latest digital cameras and this allows for precise colour adjustments [Morley and Parker, 2009].

The *International Standards Organization* (ISO) is the group responsible for the development of light sensitivity specifications. The ISO number after the acronym is an indication of the sensitivity of the selected film or digital sensor used in a photographic device. The greater the number, the more sensitive the film or sensor is to light. This means lower shutter speeds or larger apertures can be used for a given light condition. In the present work, apertures and shutter speeds are not specifically used; however, the choice of ISO setting is crucial in capturing a high quality image.

Digital ISO settings are specified on the camera body in situ. The settings vary from camera to camera however they generally start at ISO100 and work their way up to as much as ISO100000. The digital settings inform the camera how much gain to apply to the signal obtained from the CMOS or CCD sensor. The problem of signal-to-noise ratio arises at this point since if the signal levels are boosted, so is the noise level. As the gain is increased, the noise in the images also increases and this inherent problem can cause drastic loss in image quality. The speckled appearance of an image indicates a high ISO setting was used.

Modern digital cameras have a number of brand specific enhancements which promise to reduce noise and improve low light photographic images. This comes at a cost of image clarity and captured details. Noise reducing algorithms are used to scan the image for specific patterns and consequently clean the image by creating regions which are averaged. This eliminates the finer image details and for quantitative work introduces even more data variation.

The construction of the sensor also plays a role in the effect of noise generation in the captured images. Full frame 35mm sensors are less susceptible to noise since the total light

sensitive area is larger than smaller sensors. CCD sensors produce more noise because of the higher power demands and thus higher operating temperatures. Ambient conditions also affect the noise characteristics of the sensor; a greater temperature will increase noise levels [Steinmueller and Gulbins, 2010].

File formats, image data encoding and compression methods vary from camera to camera. As the image is captured by the camera, the data is processed and optimized. Various alterations are made in the attempt to match the photo to the surroundings in terms of colour, brightness, colour temperature, exposure and compression. Modern cameras have very advanced techniques and imaging processors to do this seamlessly and efficiently, however, the effects of the processing generates variations from the original light data which struck the imaging sensor [Steinmueller and Gulbins, 2010].

Variations such as colour correction and image compression result in captured images not being indicative of the actual light and colour data striking the image sensor. For this reason, raw un-edited data is recorded directly from the sensor and stored in a commonly termed 'RAW' file format. The structure of RAW files might vary between manufacturers but the data conveyed is the same.

2.6.2 Image post-processing

Image post-processing and analysis is an important and powerful aspect of the digital image system. Not only does it allow for fine, and otherwise invisible, data to be extracted but it increases visual appeal and allows complex image analysis to be undertaken. A number of image adjustments are discussed below which are pertinent to this study.

Image leveling is an adjustment applied to an images channels enabling them to use the full number of bit variations available. Typical image leveling systems will scan a particular image channel for the highest and lowest values. These values are then remapped to utilize the full colour range from 0 to 255 or 0 to 1 for monochromatic images.

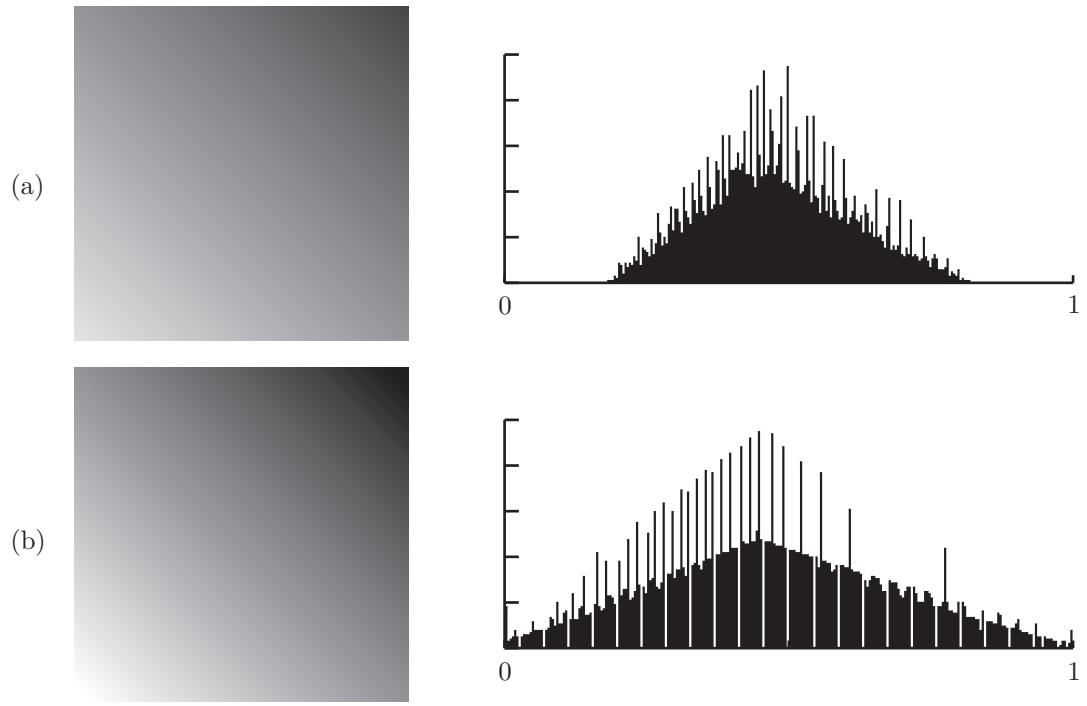


Figure 2.19: Monochromatic image leveling illustration (a) before adjustment; (b) after adjustment

This method of image adjustment improves the contrast and brightness of the image however it may be desired to adjust those settings individually to enhance or reduce the image characteristics. Figure 2.19 illustrates an image before and after leveling. It is clear from the images that the leveled image contains far more detail and contrast than the un-modified image. Examining the histogram before adjustment, there are a large number of pixels (vertical scale) which fall midway between 0 and 1. It is also apparent that almost half of the available pixels values are not used. The lower range of pixels, from 0 to about 0.25 illustrate that the image blacks are not actually black but rather a grey, similarly, the upper range appear light grey instead of white. The histogram after adjustment shows the full range of possible pixel values are used and the corresponding image displays true whites and blacks.

Image clipping may occur if an image is leveled too much. This occurs when pixel values are set to over 255 or 1 for colour and monochromatic images respectively. If pixel values are set to below zero, for both types of image, similar effects are generated. This technique may be useful in some cases but should be avoided for the colour schlieren methods described herein as image information is lost upon applying this kind of transformation.

Contrast is the ratio of the lightest pixel to the darkest pixel. When the contrast is increased, the ratio between the darkest and lightest pixels is increased and the image becomes more colour rich.

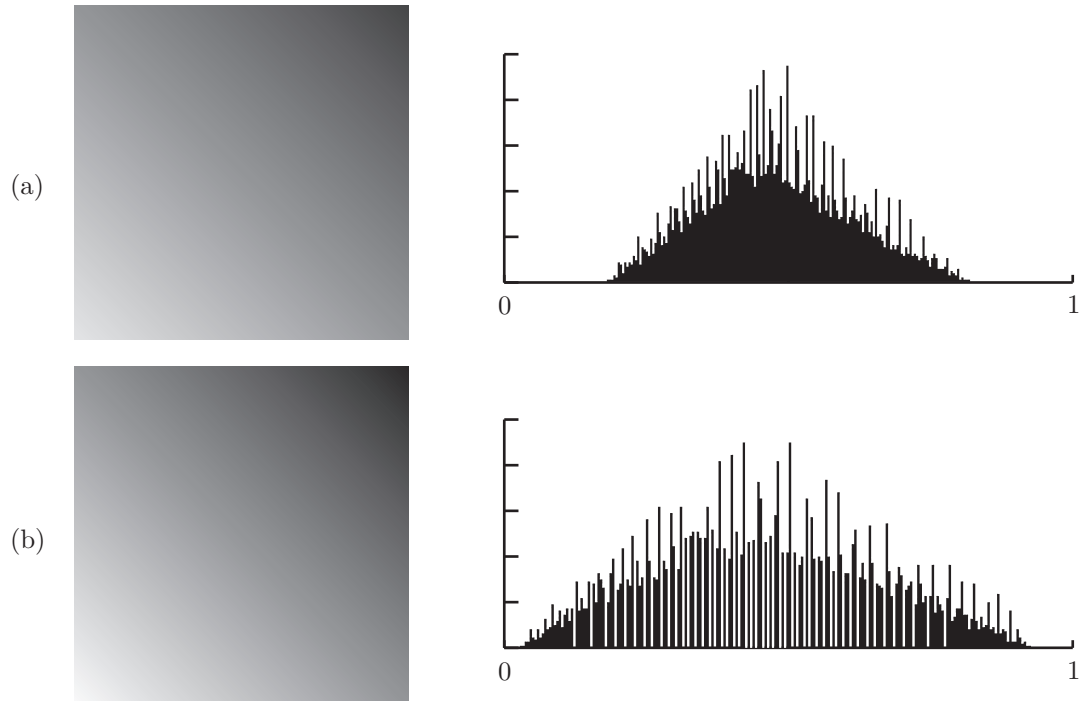


Figure 2.20: Monochromatic image contrast adjustment illustration (a) before adjustment; (b) after adjustment

Increasing the contrast, as in illustration 2.20, it is clear that the range of the image has also increased in a similar fashion to the image leveling adjustment. It can be seen that the new pixel value range does not completely fill the available range for a 100% increase in the contrast ratio. The adjusted image exhibits brighter whites and darker blacks.

Brightness adjustment is simply a control to shift the pixel values along the histogram. This procedure adds or subtracts a given value from all pixel values thereby increasing or decreasing the image brightness respectively.

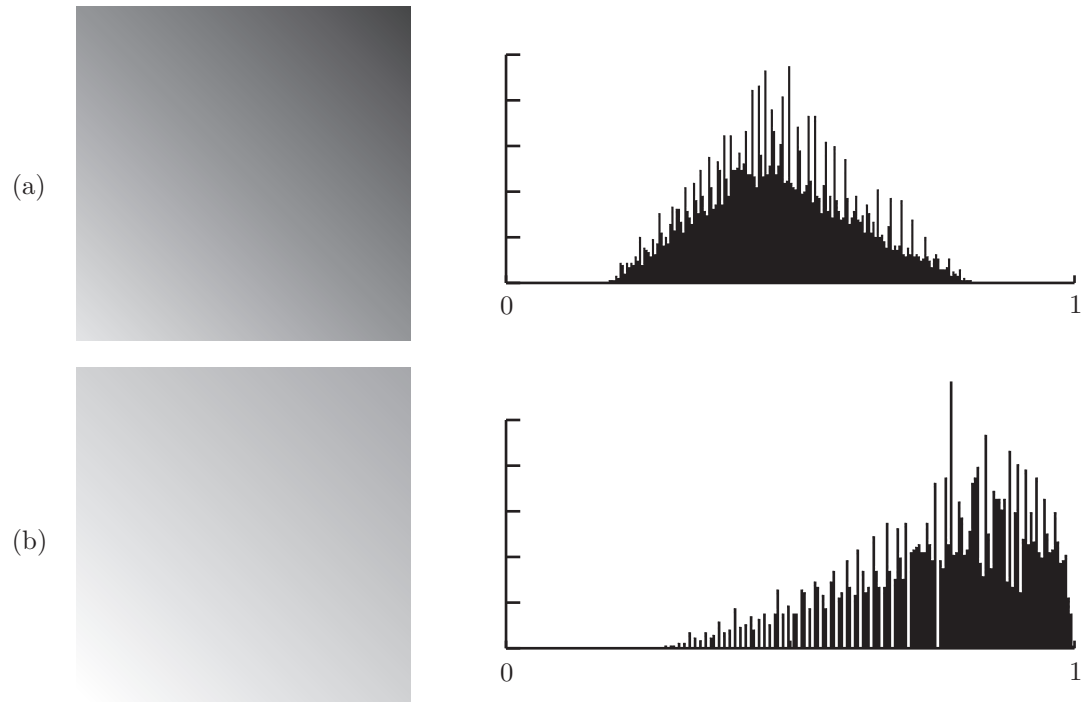


Figure 2.21: Monochromatic image brightness adjustment illustration (a) before adjustment; (b) after adjustment

Figure 2.21 illustrates this effect by applying a gain of 0.5 to each pixel. The histogram illustrates how the range is shifted to the right. It is important to note that brightness adjustment, as with most image adjustments, can have negative effects. If the image is brightened too much to either extreme, the pixels will tend to "pile up" at pure white, thereby destroying highlight details or, conversely, at pure black, destroying shadow details.

Thresholding is perhaps more of an analysis tool than an image adjustment tool. Simply put, thresholding decreases the number of colours an image is allowed to exhibit.

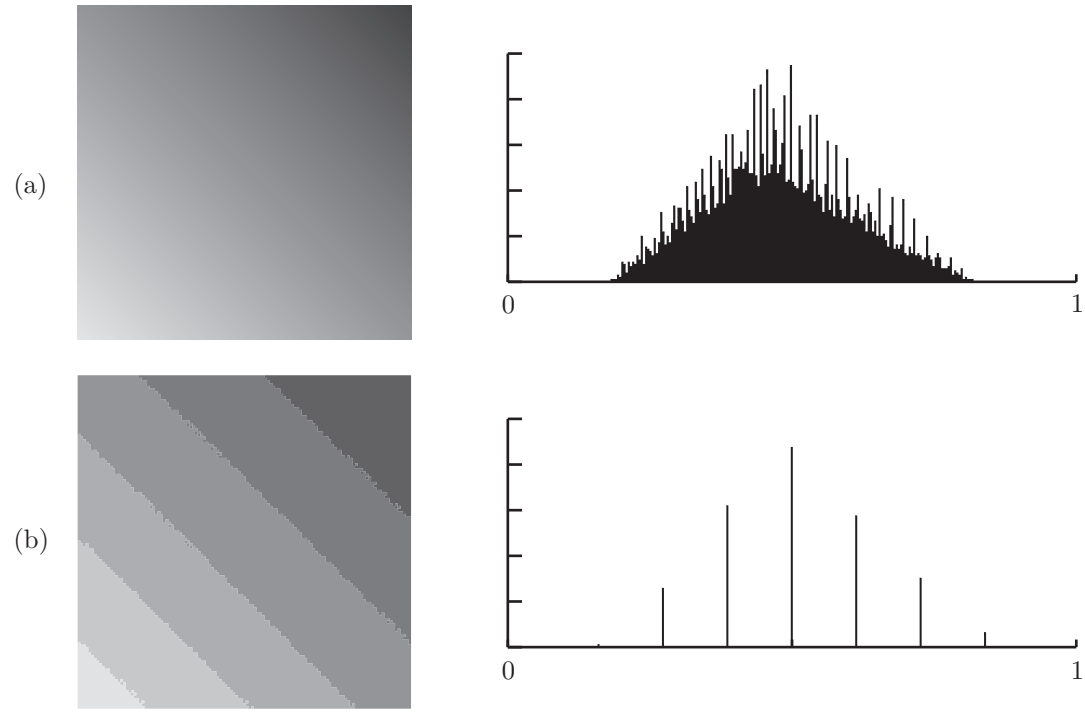


Figure 2.22: Monochromatic image threshold adjustment illustration (a) before adjustment; (b) after adjustment

By decreasing the number of colours, bands of equal colour pixels begin to appear. This method produces a contour like effect in the image as can be seen in figure 2.22 (b). Note the histogram has not shifted horizontally, however, the pixel values have been limited to specific values. The number of levels, or possible values a pixel may display, has been reduced from 100 down to 6. Therefore, 6 bands of constant colour have been produced and it is then clear that the gradient direction in the image flows from the lower left to the upper right. Each band indicates the number of pixels for that specific pixel intensity. The space between the bands is empty since there are no pixels in the image which exhibit those intensity values.

Thresholding is a useful technique to apply to an image to understand how gradients flow within an image as well as to reduce possible colour combinations thereby simplifying colour matching procedures between two images.

2.6.3 Spectral Responses

The response of the human eye to the visible spectrum is highly non-linear and as such any attempt to visually analyze an image will result in a degree of bias towards certain hues. Imaging processors found in cameras are designed to analyze the content of the images taken and make contrast adjustments in such a way so as to produce the most appealing life-like hues.

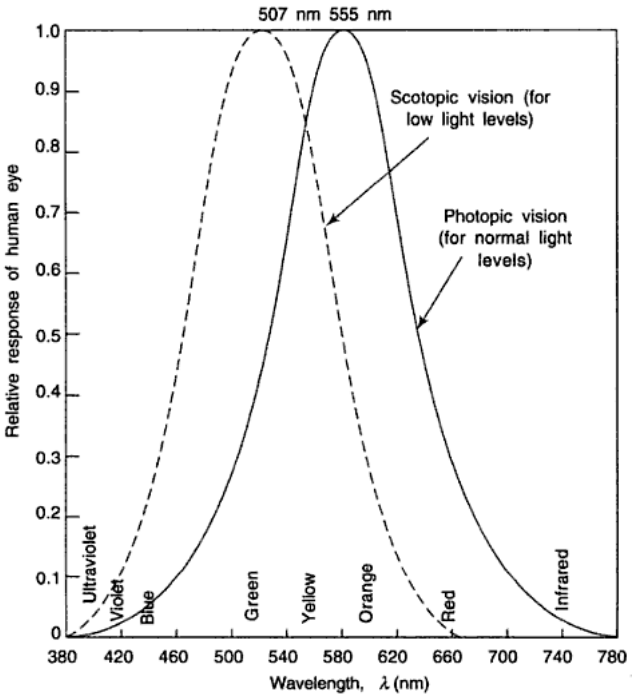


Figure 2.23: Eye response, [Kumar et al., 2008]

The sensitivity of the average human eye to normal light levels extends from around 380nm to 760nm. The peak sensitivity for photopic vision, normal light conditions, occurs at approximately 555nm while for scotopic vision, low light level conditions, the peak is shifted by 48nm to 507nm. This is shown in figure 2.23. It has been found that the human eye's sensitivity changes according to the level of light. The human eye is more sensitive to green-yellow and less sensitive to violets and reds [Kumar et al., 2008].

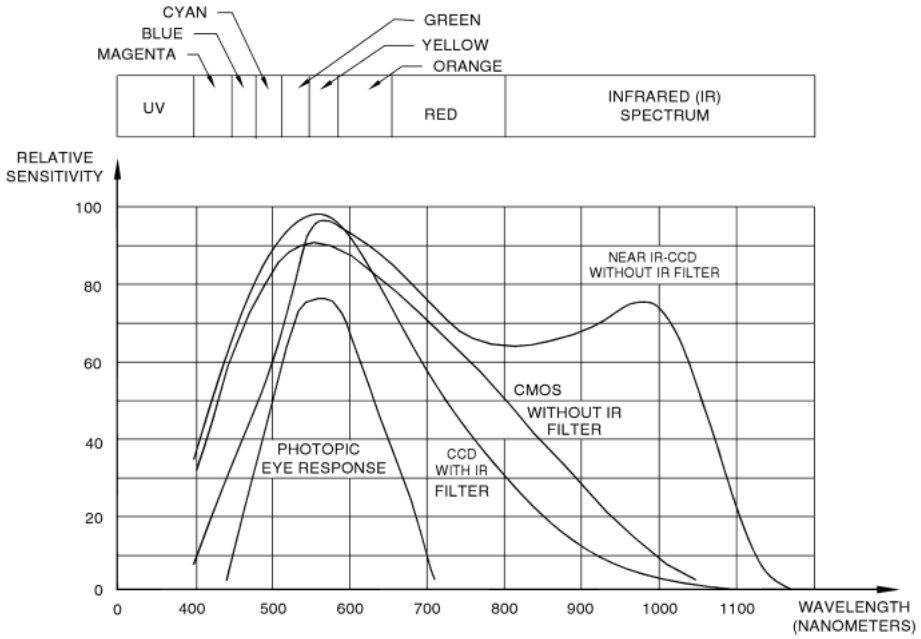


Figure 2.24: Spectral response comparison between the human eye and CMOS/CCD sensors, [Smith, 2006]

The response of CCD sensors, but not all CMOS sensors, is linear with exposure. This photometric property makes the CCD sensor a good quantitative tool to analyze levels of light. Referring to figure 2.24, CMOS and CCD sensors have a much broader spectral response than that of the human eye. They are able to detect, without filters, the range from 0.35µm to 1.1µm. The installation of infra-red filters improves image quality and colour responses in the visible spectrum [Smith, 2006].

Chapter 3

Objectives

The objectives of this study are:

- To create an accurate shock tube colour schlieren system which produces repeatable results suitable for quantitative analysis. The optics system should be based on working colour schlieren setups however, any areas of improvement should be focused on and adjusted accordingly. Quantitative systems have been produced for continuous wind tunnels but none, without exhausting literature research, for single shot shock tubes.
- To, as accurately as possible, obtain experimental images from the colour schlieren system and quantitatively analyze and compare them to CFD images. Shock tube tests will be conducted using models with known fluid flow phenomenon thereby validating both CFD and experimental results.
- To design and produce a prototype high power LED light source with the intention to match the performance of the existing Xenon flash lamps. If the results are found not to meet or surpass the required performance standards of the flash lamps, then producing a high power constant light source to aid in schlieren setup will be undertaken.

Chapter 4

Design Development

This section details the design development of new equipment required for testing and any updates or modifications to existing equipment.

4.1 Source Masks

4.1.1 Software used

The source masks used for the colour schlieren system, described in this dissertation, are digitally designed and printed using standard film photographic methods. The digital design concept provides a great degree of design freedom and accuracy. Image processing packages such as Adobe Photoshop (CS5) are readily available, however, at a price. Academic copies of Matlab (Version 7.3.0.267 - R2006b) provide ample computational power to generate the required images.

Source code has been included in Appendix B.

4.1.2 Code Description

A Matlab script m-file was generated to produce the images. The script computation includes the equations used to determine the degree of distortion required due to the cylindrical lens. The user is simply required to enter the details of the schlieren system and the correct source mask will be produced.

The script is complex enough to allow the generation of a number of different arrangements of colours; 'morph' ratios to account for the cylindrical lens; sizes and ratios of the inner colour bands. The script outputs a high resolution uncompressed TIFF file format which is then sent to the printing-house and a positive slide is developed.

4.1.3 Source mask design

The source masks used in this colour schlieren system are based on the annular round dissection method devised by Gary Settles in 1980. A variable aperture iris diaphragm is used in the cutoff plane to control sensitivity. The original method allows for the best mixing of colours since only three primary colours are required [Settles, 2001].

The source masks are produced digitally and need to be transferred to a transparent media. There have been propositions of using digital displays or projectors to replace the film equivalents; however the quality has not proven to be adequate [Ting et al., 2004].

The most suitable media is Fuji 35mm colour film, 100 ISO. The source mask images are printed at high resolution using commercial quality photographic printers. The printed images are then placed on a photographic air board with suitable lighting surrounding them to reduce any reflections yet supply enough ambient lighting for good contrast and colour saturation.

Referring to section 2.3.3, the source masks need to be designed with a certain distortion to account for the astigmatism reducing cylindrical lens. Calculating the astigmatic difference for the optical system, using equation 2.11, yields a difference between the sagittal and tangential focal points of 8.45mm for a schlieren system angle of 10 degrees. To determine the distortion required, equation 2.16 is required in conjunction with equation 2.15 and 2.14.

Equations 2.15 and 2.14 yield $d_o = 54.75mm$ and $d_i = -46.30mm$ respectfully. The negative d_i indicates the virtual image falls on the same side of the cylindrical lens as the object.

The inverse of equation 2.16 results in the total magnification value of the source mask in the sagittal plane; $m = 0.85 \implies \frac{1}{m} = 1.18$.

Thus the source mask needs to be stretched by 18% horizontally to account for the cylindrical lens. Taking into account the dimensions of the cylindrical lens is important as the total encompassed area of the annular rings needs to fall within the bounds of the cylindrical lens area. If this is not the case, light is lost out the edges of the lens and may cause distortions or stray light to enter the schlieren optics.

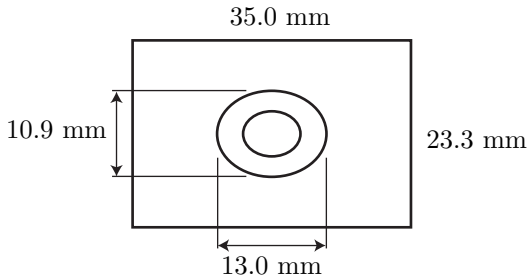


Figure 4.1: Source mask schematic

The horizontal dimensions, figure 4.1, of the slide and the outer annular ring are 35mm and 13mm respectively while the vertical dimensions of the slide and the outer annular ring are

23.3 mm and 10.9mm. These dimensions give a ratio of 1.5 for the photographic slide and 1.19 for the actual mask.

The images are then photographed with a standard 35mm film camera at various shutter speeds and apertures to obtain a mixed set of exposures on film. The images then undergo the standard development process for photographic film.

Resulting source masks are then checked and discarded depending on the apparent colour saturation, clarity, focus, noise, brightness and quality of print. The final selected masks are mounted in 35mm frames, ready for placement in the schlieren system for testing.

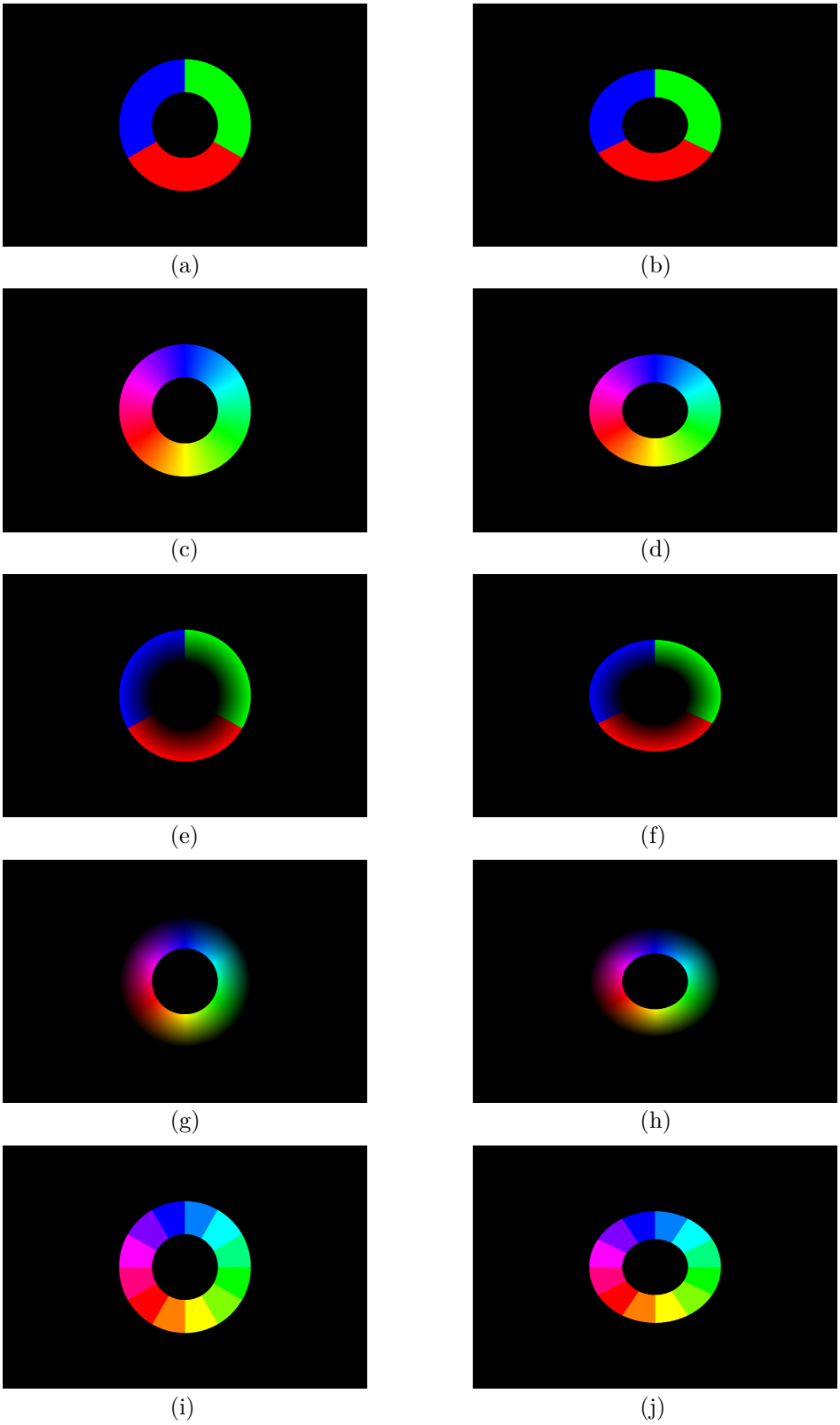


Figure 4.2: Variety of source masks designed and printed for testing and comparison

Figure 4.2 (a) is a conventional tri-colour mask with a red, green and blue filter. This

is the design most commonly used, however, it relies on the optics to mix the colours in order to form all the colours in the visible spectrum; (c) is a full colour wheel, presenting all the colours already pre-mixed and offering no bias to one particular hue. If density gradient directions are required in a particular colour, the source mask colour positions may be rotated by an arbitrary angle, in this case by 120^o, as an example; (e & g) Research was undertaken into the possibility of using graded colour filters, from light to dark (e) or dark to light (g). It was hypothesized that the grading may in fact alter the linearity of the sensitivity of the schlieren system; (i) Shows a source mask exhibiting only 12 colours, however, it's performance was estimated to be similar to that of (c).

A number of different source masks designs were printed, a few of these are illustrated in figure 4.2. The left column presents source masks without cylindrical lens compensation whilst the right column is adjusted for a cylindrical lens as per the above calculations. It is clear that the compensated source masks are 'morphed' or 'squashed' vertically to account for the change in aspect ratio of the source image induced by the cylindrical lens. As the light rays pass from the source mask through the cylindrical lens, a circular virtual image is created which then allows an iris diaphragm to be used in the cut-off plane.

4.2 LED Light Source

4.2.1 Design considerations

Pulsing an LED with microsecond durations requires precise electronics with minimal rise and fall times. In section 2.4, it was discussed how the duration of the light pulse will drastically influence the quality of image obtained by the schlieren system. The requirements of the duration of the light pulse are defined by the flow phenomenon being investigated. Mach 1 shock waves would require pulse durations in the region of 1µs, however, subsonic flow systems may only require light pulses in the 10's of microseconds range to produce sharp clear images. For this reason, a modular and adjustable system is implemented to encompass a wide range of possible test requirements.

Since LED's have nanosecond rise and fall ranges, they suit the requirements of a high speed pulsed light source very well. Higher power and efficiency LED's are constantly being developed and refined and as such the circuit will allow for new LED's and configurations to be installed to improve the overall light source performance.

The pulse width of the light source is easily configurable by the user as this allows for optimum lighting selection to match flow requirements. The area in which light emanates has been reduced as far as is practicably possible to reduce divergent light leaving the system.

Since a shock wave is essentially a very small finite thickness of continuously varying fluid properties, the refraction of light in this region is so significant that it produces a dark region in schlieren photographs. Thus, as the light pulse duration decreases, so the clarity of the shock wave improves and the dark regions become more apparent. To capture shock waves

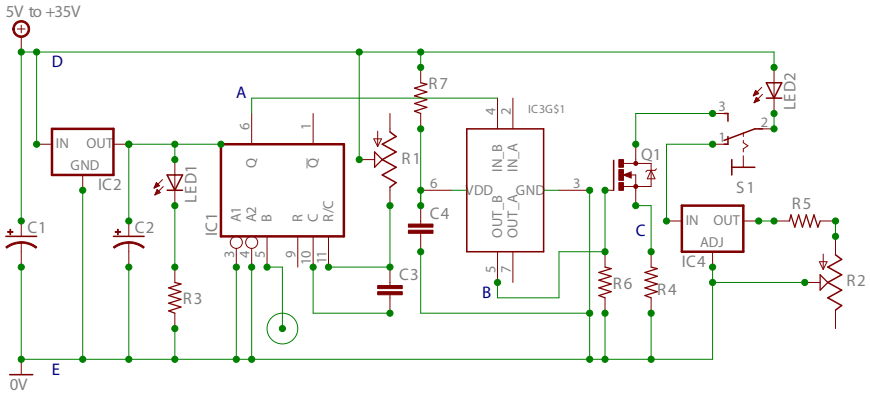
moving at between Mach 1 and Mach 2 the duration of the illumination would need to be within 1µs and 3µs. Anything greater would lead to a blurring and a reduction in detail as the shock front moves between 0.34mm and 0.86mm per micro-second of illumination.

4.2.2 Circuits examined

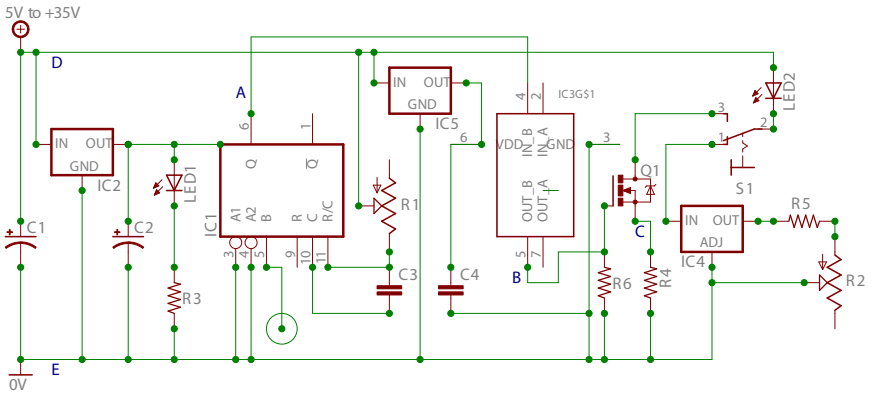
The pulsed LED system designed by Buttsworth and Ahfock [2003] was constructed and its efficacy was tested for use with the colour schlieren system. The drive circuit is triggered by a TTL signal from the data acquisition system. This trigger pulse turns on a number of transistors which in turn supply power to a resistor-capacitor pair which has a specific RC time constant. It is this combination in conjunction with a 4081 CMOS device which produces the required pulse. The pulse is then conditioned by use of transistors to improve the current gain which allows for rapid switching of the power MOSFET device. The circuit allows for a continuous illumination mode and includes a 1 ohm resistor for current monitoring. Additionally, there is a small side circuit which allows the power capacitors to be drained before the continuous illumination mode is activated, simply to reduce any voltage or current spikes overpowering the LED's. The circuit diagram as tested has been included in Appendix A.2.

A similar operating LED pulsing circuit designed by Hargather et al. [2009] and based on research by O'Hagan et al. [2002] was examined. The LED circuit was designed for use with a focusing schlieren system and was comprised of four 15 watt high-power cool-white LedEngin diodes. It was found that the circuit could produce 500ns pulse durations with the required square-wave illumination profile. The reported performance of the circuit was only adequate when the light from the diodes was directed directly into the camera instead of into a ground-glass diffusing plane. The diffuser decreased the image illumination by 2-4 stops and resulted in inadequate illumination even when in conjunction with a holographic diffusing screen. It was decided that the LED array could be boosted from 4 units to 16 units, thereby increasing the illumination sufficiently. No results were recorded for the improved system as the overall dimensions of the enlarged array were simply too significant to ignore. This system together with the improved LED array both rely on the pulse width of the TTL signal coming from the triggering systems to define the pulse width of the LED light source. The original circuit diagrams have been included in Appendix A.3. [Hargather et al., 2009]

Working closely with the circuits designed previously by Buttsworth and Ahfock [2003], Hargather et al. [2009] and O'Hagan et al. [2002] the author designed and developed a similar circuit capable of producing sub-microsecond illumination pulses. The design of this circuit can be found in the following section. This circuit aims at replacing the existing and expensive xenon flash lamps as well as adding features such as a continuous mode for optics setup or high speed photography.



(a) Circuit for use with a source voltage up to 15v



(b) Circuit with included 12v voltage regulator for 4427 IC MOSFET driver

Figure 4.3: Circuit diagram of high power LED light source

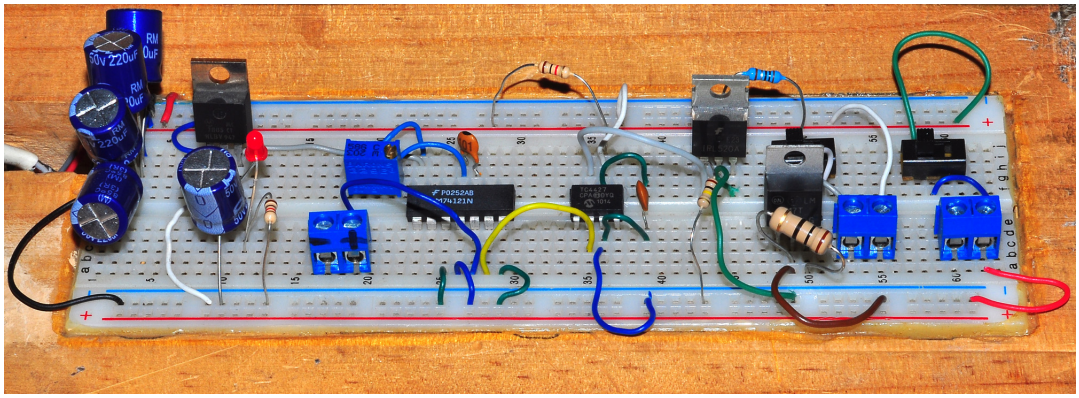


Figure 4.4: Photo of high power LED light circuit as tested

4.2.3 Circuit design

Details of the high power LED light source circuit are presented in figure 4.3. The circuit has been designed with simplicity in mind and has kept components to a minimum whilst still providing a large degree of flexibility in its operation. A variable voltage, self regulating

current, desktop power supply unit (Topward, Dual tracking DC power supply, 6306A) provides the power to the circuit as well as the high power LED's.

Capacitors C1 and C2 ($50v$ $220\mu F$) have been included to smooth out any voltage fluctuations in the system. The voltage supplying IC1 (pin 14) is regulated by a $5v$ voltage regulator, IC2 (L7805CV). It is able to supply a peak current load of 2 amps and maximum supply voltage is limited to $35v$. A power-on indicator, LED1, is a 5mm low intensity red LED coupled to a current limiting resistor, R3 ($1k\Omega$).

The main controller of the circuit operation is IC1 (DM74121N). This unit is a monostable multivibrator which features both positive and negative edge triggering with complimentary outputs. Pulse widths available range from $30ns$ up to 28 seconds and the unit is compensated for supply voltage and temperature fluctuations, National-Semiconductor [1995]. The IC is connected such that it accepts a rising edge trigger on pin 5 to trigger the light source. The internal circuitry requires pins 3 and 4 to be grounded. The timing operations of the IC are controlled by variable resistor R1 and ceramic capacitor C3 ($100v$ $100pF$). This RC combination produces a specific charge/discharge time which IC1 monitors and uses to control the pulse width outputted on pin 6. Pins 1, 2, 8, 9, 12, 13 are not currently used whilst pin 7 is connected to $0v$.

The output of IC1 (pin 6) is not able to supply enough current or voltage to drive a high power LED directly and thus an electronic relay system is required. The output form pin 6 is fed into the input, pin 2, of IC3 (TC4427) dual input MOSFET driver. This driver accepts the low voltage from IC1 and, with incredibly fast sub-50ns switching times, connects the output, pin 7, to the separate supply voltage, pin 6. This allows the MOSFET NPN transistor Q1 (IRL520) to turn on with much higher voltage and thus its current gate can be opened with a lot more force. In the low voltage circuit, resistor R7 ($1k\Omega$) is in place to limit the current drawn by the MOSFET driver and capacitor C4 ($100nF$) reduces the effects of any transient voltages over the driver. The higher voltage circuit utilizes a 12v voltage regulator IC5 (L7812) to regulate the supply voltage for use by IC3.

A number of IRF transistors were sampled however the IRL series are logic based transistors and thus turn on at a lower gate threshold voltage. This means a lower overall rise time and allows the LED to draw a larger current thus increasing intensity. Resistor R4 (1Ω) is in place to limit current draw as well as to monitor the current drawn by the high power LED2. This 1/4 watt resistor is not in place to limit the pulse current but rather to limit the current to LED2 in the event of the transistor remaining in its on state for whatever reason. The idea is that the resistor will burn out before the LED has a chance to heat up and potentially blow. The resistor has a tolerance of 1% within its stated value and is thus accurate enough for the purposes mentioned herein.

To prevent the transistor from turning on due to stray voltages when no voltage is supplied by IC3, a pull down resistor, R6 ($100k\Omega$) is connected to the gate of the MOSFET. This resistor will dissipate any voltage supplied to the MOSFET and reduce the likelihood of the transistor turning on.

The added advantage of using an LED based light source is that it can be kept on for setup and alignment purposes. The single pole, single throw switch S1 is used to change between

pulsed operation and continuous operation. When switch pins 2 and 3 are connected, the circuit is in pulsed mode and the LED is waiting for the ground connection which is made available momentarily by the power MOSFET. When switch pins 2 and 1 are connected, the light source is in constant mode. Constant mode allows LED2 to illuminate continuously; it does this by limiting the current passing through the LED by means of IC4 (LM317) voltage/current regulator. The LM317 regulator constantly monitors the voltage over the output and adjustment pins. Internal circuity requires the voltage over these pins to be $1.25v$ and it will adjust the current it pushes out to achieve this. Similarly, the voltage drop over the LM317 is stipulated to be $3v$ and thus the supply voltage must be sufficient to allow for the voltage drop over the LM317 and LED2. This $1.25v$ is measured over the resistors, R5 and R2, and thus as the sum of the resistances changes, so will the current flowing through them. Resistor R5 is set according to the maximum current limit of LED2. Resistor R2 is an adjustment resistor to decrease the intensity of the LED if it is too bright. These values are not specified since the specifications of LED2 change according to what the system requirements are.

A sample calculation to specify resistances R5 and R2 using a MCE Cree LED as LED2.

The LED has a forwards voltage drop of $11.5v$ at a maximum current draw of $350mA$. Applying a safety factor to avoid running the LED at its maximum current for extended periods, the current is reduced to $300mA$. This means a total of $300mA$ is to be allowed to flow through both the LED and resistors R5 & R2. By Ohm's law, assuming R2 to be zero since an increase in the sum of the resistances will reduce the current flow, and the fact that the LM317 requires a $1.25v$ drop, the following is calculated:

$v = ir$

$\therefore r = \frac{v}{i}$

$r = \frac{1.25}{0.3}$

$r = 4.16\Omega \approx 5\Omega$

$p = iv$

$p = 0.3x1.25$

$p = 0.375w \approx 0.5w$

So, in order to limit the current to $300mA$ flowing through the LED a resistor of 4.16Ω is required, however this resistor is most likely not available so the figure is rounded up to the next whole number, 5Ω. The power dissipation required by the resistor is found to $0.375w$ which is again rounded up to $0.5w$. This will allow the resistor to dissipate the energy safely and not burn out. The adjustment range of R2 should ideally be double that of R5. In this case, doubling R5 would result in a range of R2 between 0Ω and 10Ω. Setting R2 to its maximum value would result in the current flowing through the LED to drop to $0.08mA$. It is important to note the variable resistor must also be capable of dissipating the calculated power as for R5 although it will never actually be required to dissipate as much energy as R5 alone.

4.2.4 Circuit operation

The supply voltage to the circuit must be set between $17v$ and $30v$. The reason for this is because the voltage regulator (IC5) requires a minimum of $17v$ DC to output a constant $15v$ for the MOSFET driver.

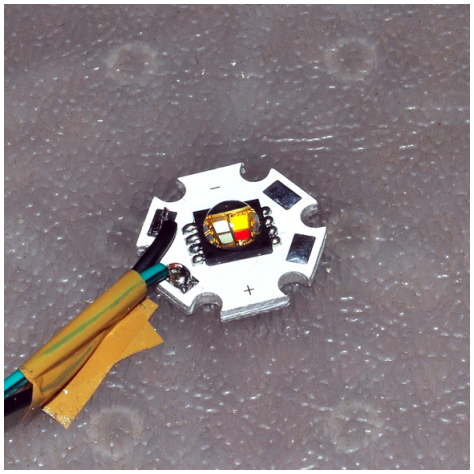
With S1 set to pulsed mode, the IC1 chip is powered with the $5v$ created by IC2. The 3mm red indicator LED will illuminate indicating the circuit is powered up. IC1 is triggered by a 5 volt *Transistor-Transistor Logic* (TTL) signal pulse from the data acquisition system. As the pulse is received, IC1 reconfigures the pulse depending on the resistor-capacitor combination (R1 and C3) and outputs a $3.4v$ square wave pulse through pin 6 to MOSFET driver IC3. The gate threshold voltage of Q1 falls between 1 volt and 2 volts and thus the 3.4 volt IC1 driving voltage is insufficient to turn on Q1 alone. IC3 receives the pulse and internal circuitry allows the voltage regulated $15v$ supply to pass through to the gate pin of MOSFET device Q1, turning the MOSFET on.

Approximately 100 nanoseconds after the pulse reaches the MOSFET, an internal electronic gate is fully closed and current is allowed to flow between the source and drain pins. This circuit is now closed and current is allowed to flow through LED2. Microseconds later, the square wave pulse ends, the MOSFET gate opens and the current is stopped, thereby extinguishing LED2. IC1 is set to trigger on a rising edge pulse so provided the TTL signal is constant and does not increase, IC1 will not be triggered again until the input signal ends and is re-triggered.

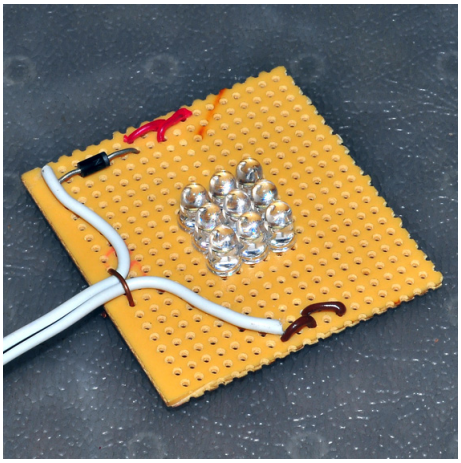
Please refer to Appendix B for details on the LED's and IC's.

4.2.5 High power LED's

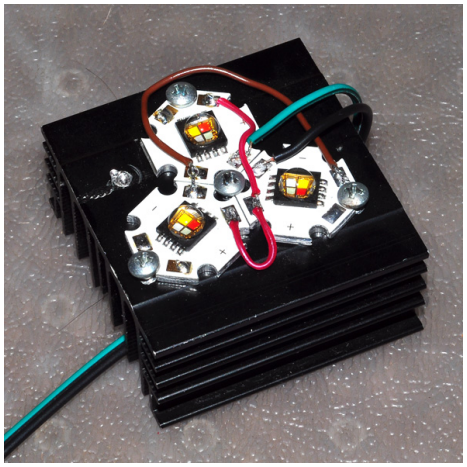
A number of high powered LED's are examined and tested for use with the pulsing circuit. Various arrangements of the LED's are investigated and are shown below in figure 4.5.



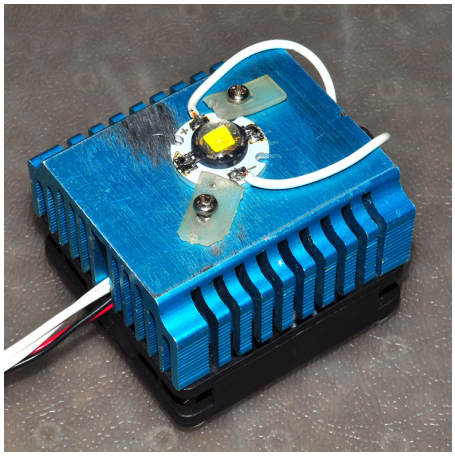
(a) Single Cree MC-E LED



(b) 3x3 Array of 5mm high power white LED's



(c) Array of 3 Cree MC-E LED's mounted to heat sink



(d) Single Seoul P7 high power LED mounted to heat sink with fan

Figure 4.5: High power LED's

The Cree colour MC-E LED's, figure 4.5a, are 4 diode emitters, containing individual red, green, blue and warm-white diodes within a single LED enclosure. Each LED is soldered onto a *Printed Circuit Board* (PCB), to which the positive and negative leads are connected. The individual diodes are connected in series which means the current flowing through each diode is identical. This also means the overall voltage per complete LED is in the region of $11.5v$ for a current draw of $350mA$. The typical luminous intensity for the LED at this power rating is 180 lumen however the distribution of the intensities varies drastically for each LED diode to obtain the most uniform warm white light. The warm-white and green are highest with 80 lumen and 67 lumen respectively while the red and blue are 30 lumen and 8 lumen respectively.

Figure 4.5b, shows the 3x3 array of 5mm round 20000 mcd white LED's. These LED's are not as powerful as the multidiode LED's however they do exhibit a lowered beam divergence due to the reflector and lens system covering the diode. This implies that more of the produced light is directed forwards in comparison to the multidiode LED's. The forward

voltage of these LED's is in the region of 3.0 - 3.2 volts while drawing a current of $20mA$. The LED arrangement uses a parallel configuration as this keeps the forward voltage the same but allows the circuit to draw a proportional amount more amps. The idea being that the voltage supplied to the circuit may be increased quite significantly to allow more current to be drawn by the LED's and consequently produce more light. A diode is included to prevent the LED's blowing if the polarity is inadvertently reversed.

To further increase light output, a number of the Cree MC-E LED's are wired in parallel and placed on a heat sink, figure 4.5c. This again allows the voltage to remain the same over each LED and thus allows more current to be drawn at a lower voltage. The total forward voltage is as per a single chip LED of $11.5v$ for a current draw of $350mA$.

The final LED configuration tested was using a powerful multidiode LED produced by Seoul Semiconductors. The LED chip, known as a Seoul-P7, is capable of outputting up to a maximum of 900 lumen. The typical output of 700 lumen occurs with forward voltage of only 3.6 volts at 2.8 amps. In short, this LED is very bright however the light it produces is not focused and the distribution pattern is similar to the Cree MC-E LED's.



(a) A $30mm$ diameter $f/2.4$ plano convex lens



(b) Ledil smooth spot lens for Cree MC-E LED's, 10^oFWHM



(c) Sekonix P7 collimator lens #1 for Seoul P7 LED, 15^oFWHM

Figure 4.6: LED Lenses

A few lenses, figure 4.6, were used in conjunction with the LED's to decrease the beam divergence and capture as much of the produced light as possible. The lens, shown in figure 4.6a, is an $f/2.4$ plano-convex glass lens. The lens is used as a means to distribute the light produced by the LED evenly over the upstream source mask surface. Similarly, figures 4.6b and 4.6c, the molded plastic lenses are used to fit over the LED diode. These high efficiency optics utilize *Total Internal Reflection* (TIR) to collimate lambertian light from an LED into a collimated beam. The lenses for the Cree and Seoul have beam divergences of 10^o and 15^o degrees respectively.

4.3 Colour schlieren code

Comparisons of experimental data to computational data are crucial for determining whether the colour schlieren system is quantitative or not. The CFD software used does not include

synthetic colour schlieren coloring routines and as such a script is produced to colour the CFD flow systems in the same manner as the experimental photographs.

4.3.1 Software used

Tecplot (Version 360, Build 12.0.0.4231 of 2009) is used to view the CFD data outputted by Luke's code. The software is able to display any of the variables outputted by Luke's code in a graphical manner however it is unable to produce colour schlieren images with the required flexibility to compare to experimental images. A script has been generated to produce the required images for comparison. Unfortunately, Tecplot's scripts are fairly slow to run since the language is scripted and not hard coded however the time for Luke's code to run a simulation is significantly larger in comparison and so the delay is insignificant.

4.3.2 Code description

Luke's code outputs a mesh data file with the following embedded information: X & Y coordinates; Density RHO; Velocities U & V; Pressure P and Energy E. See section 5.4.1 for details on the functioning of Luke's code.

The colour schlieren script is run by the user once the data file has been loaded into Tecplot. The code has been error checked, only for the data required and calculated in fulfillment of this dissertation and as such errors may occur if different sets of data are outputted by Luke's code.

The script offers a large degree of flexibility in adjusting the visual appearance of the final image and naturally some trial and error will be required to get the desired image. The initiation section of the code allows the user to set the following parameters: RGB combination of the desired background colour; a sensitivity bias adjustment to RGB components; zone colour combination adjustment and re-ordering; rotation of the overall colour scheme in either direction; mirroring about the X or Y axes; inverting the background colour; setting minimum and maximum threshold values for finer or coarser detail enhancement.

The script has been specifically designed to generate the final image according to specifications and requirements set out in Luke's code prior to running the simulation. As such not all geometric models will require the mesh to be mirrored about the X-axis. For efficiency purposes, the simulation is run only on half the model as the system under investigation is symmetrical about the X-axis. Thus the script mirrors the data in Tecplot for a full colour representation.

Tecplot has a built in routine to determine the density gradients in each direction by interrogating the X, Y, RHO and P variables. The routine produces density gradient variables in the X, Y and Z directions however the Z direction is not required and is removed to reduce memory requirements. The resultant density gradient magnitude is calculated and

the maximum magnitude is assigned a variable to allow for the colour intensity in the final image to be adjusted to more closely resemble experimental images.

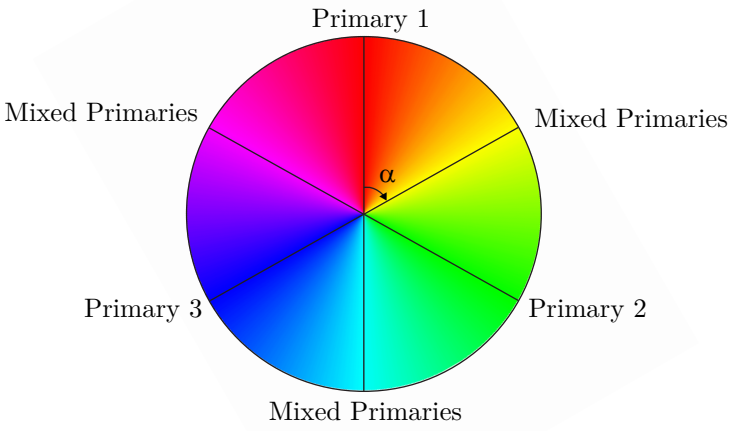


Figure 4.7: Colour distribution wheel

On closer inspection of the HSV wheel and the individual red, green and blue colour distributions (figure 4.7) it can be seen that in three main regions, the primary colours overlap to produce the main mixed primaries; magenta, yellow and cyan.

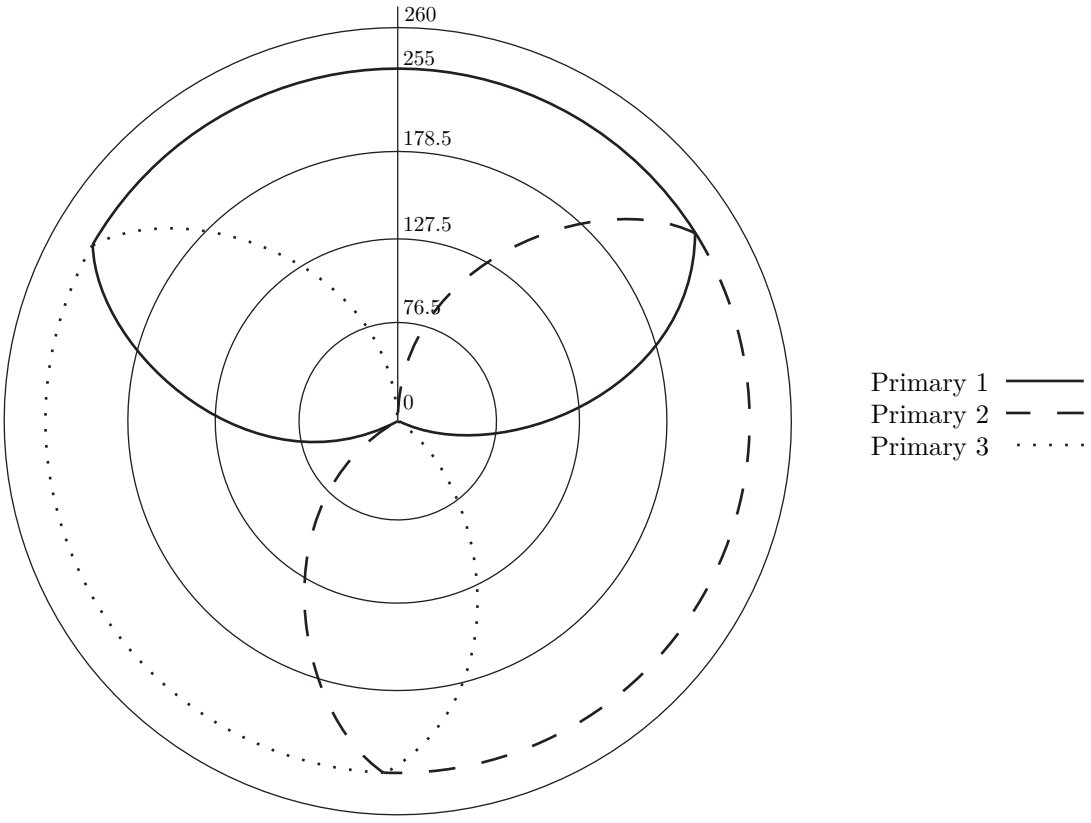


Figure 4.8: Polar diagram illustrating the intensity of the colour variation with angle

The actual RGB values adhere to a linear offset repeating pattern as shown in figure 4.9. It can be inferred that for each direction, α, a unique combination of red, green and blue values will exist.

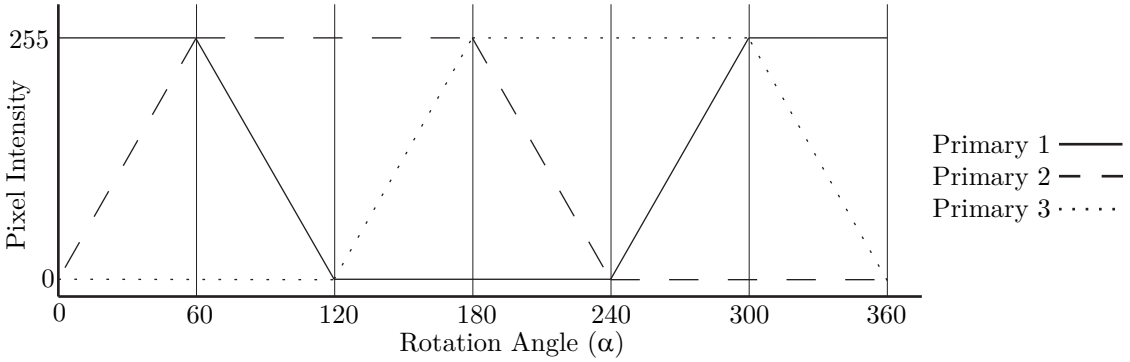


Figure 4.9: Plot of RGB colour distribution around HSV wheel

Next, the code calculates the final direction, taking into account the inputs from the user, for each point on the mesh. Each point's direction, α, corresponds to certain combination of red, green and blue components. The specific values are determined using piecewise equations derived from Figure 4.9. In the same logical step within the script, the colour components are leveled according to the density gradient magnitude and the maximum density gradient magnitude.

A few repeated settings are then quickly configured by the script and the final output is a colour schlieren representation. The complete script code is included in Appendix B.

4.4 Image post-processing

An *Open Source Computer Vision* (OpenCV version 2.1) library, assembled by members of the public and Intel, has numerous functions for the control of video and still image data. Image post processing is required to adjust and analyze the experimental images taken in order to retrieve subtle details embedded in the data within the image.

The source code, written in C++, opens both the calibration and the schlieren images into memory. Image leveling is applied equally to both images to avoid any mis-adjustment between colour components. This procedure optimizes the range of colour intensities and enhances the level of detail. Both images are then displayed. Incorporated into the software is the ability to apply a threshold to one or both of the images. This allows the user to more clearly see the regions which match most accurately to the selected region. The level of thresholding is adjustable from within the software code.

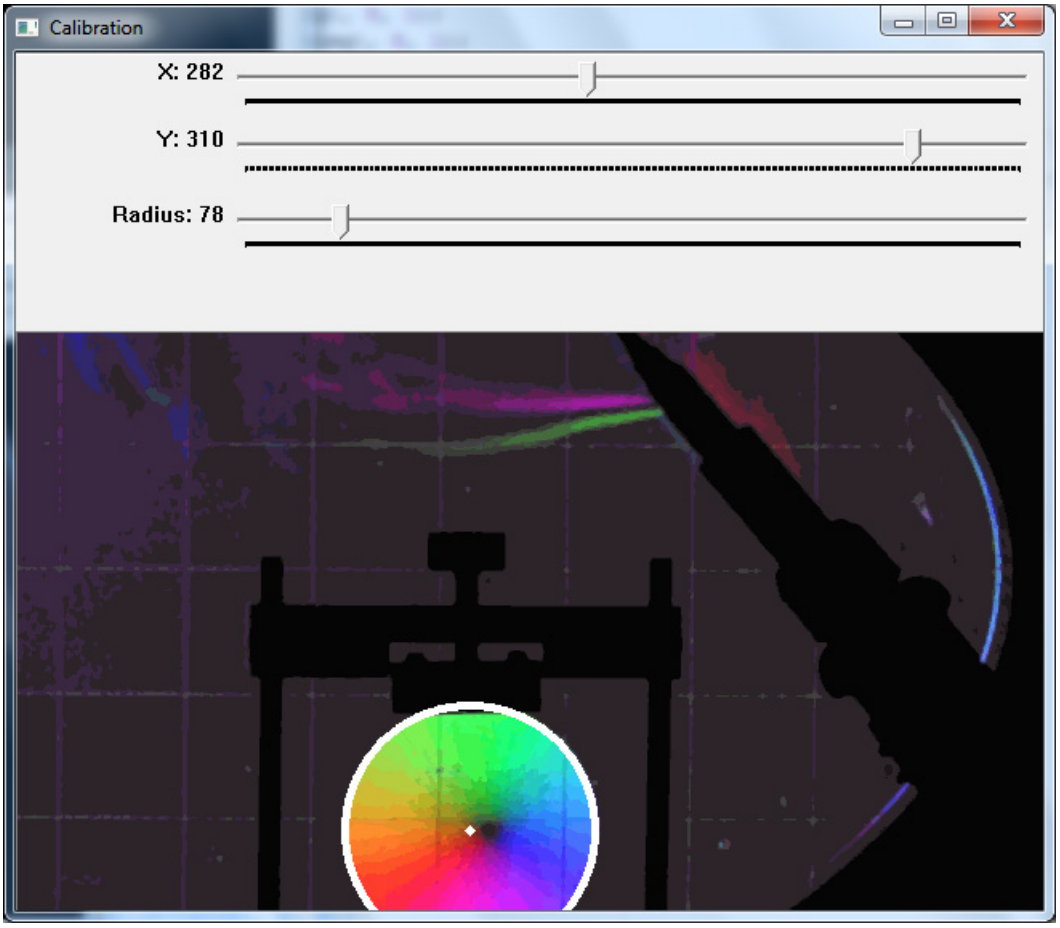


Figure 4.10: Screen shot of OpenCV schlieren software calibration window

The calibration image contains the image taken of the large focal length calibration lens placed into the test section making certain no other fluid flow disturbances present. The photo loaded, shown in figure 4.10, contains both the calibration lens as well as a disturbance caused by a butane powered soldering iron. The ignited hot gasses pass over the heating tip and exit the soldering iron towards the heating tip end through a small $3mm$ exhaust hole. The hole, in this image, is positioned in such a way that the gasses exit normal to the optical axis. This particular soldering iron makes for a good test piece since there is no stray light introduced into the schlieren system. It may also be positioned at any angle so as to produce a schlieren response in different directions.

The calibration window, figure 4.10, has a number of sliding bars on the top of the window which allows the user to position a white circle surrounding the calibration lens in the image. With predefined calibration lens settings defined in the code, this procedure informs the software where the calibration lens is, its radius and its center point, all related to the pixel positions in that image.

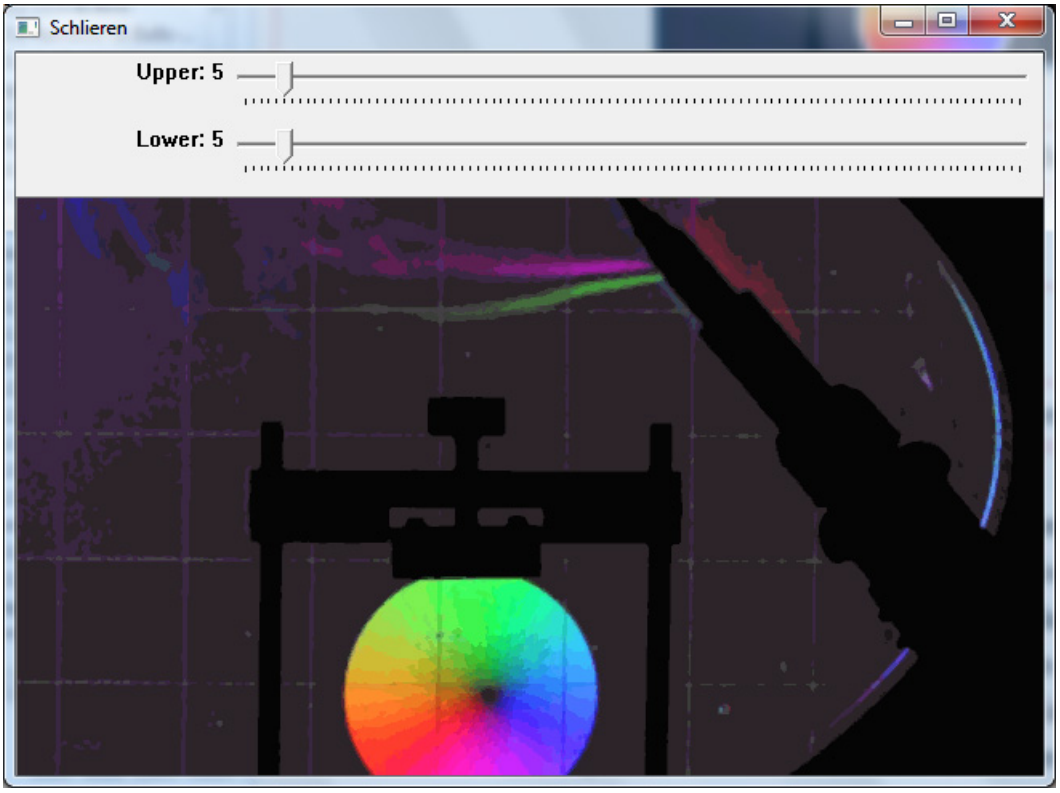


Figure 4.11: Screen shot of OpenCV schlieren software test image window

The test image window, figure 4.11, allows the user to adjust the sensitivity of the colour matching process with the sliding bars at the top of the window. The values indicate the amount of leeway above and below the selected colour which will be highlighted on the image in the calibration window.

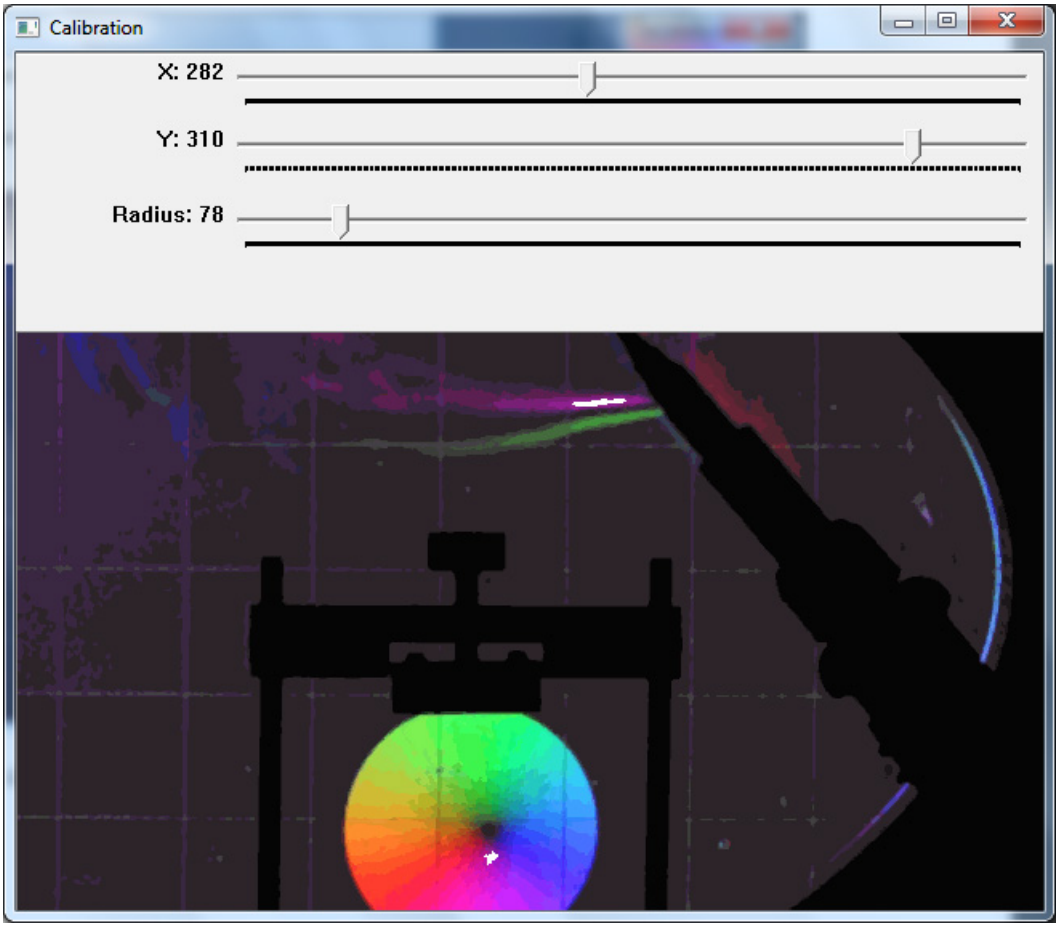


Figure 4.12: Screen shot of OpenCV schlieren software calibration window with selection

As the cursor is positioned over an area of interest on the experimental image, the corresponding region in the calibration image is highlighted, figure 4.12. The software automatically compares the colour combination and intensity levels in the two images and makes a selection in the calibration window.

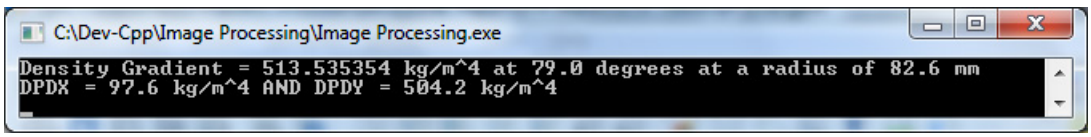


Figure 4.13: Screen shot of OpenCV schlieren software console window

As the user moves the cursor over the selected area in the calibration window, the density gradient magnitude and direction is outputted to the console window, figure 4.13. This data is calculated directly from the calibration lens settings and equation 2.37. If the user clicks on the region in the calibration window which has been highlighted by the software, the data is automatically extracted and saved in a data file. This file can then be directly imported into Microsoft Excel or Matlab for plotting.

Please refer to Appendix B for the OpenCV Code.

4.5 Image integration

An image processing script has been written within Matlab to calculate the density distribution from a density gradient image. The script allows the visualization of a density distribution of a specifiable portion of the input image. Using the theory behind equation 2.31, the image is integrated piece-wise in the x and y directions and the resultant magnitude determined. The resultant magnitude at each point forms an array which is then normalized to fall between 0 (for the darkest points) an 1 (for the brightest points). The reason for this is that the array can then simply be converted to a monochromatic image.

Image integration is not a fixed procedure or algorithm which can simply be applied to an image. There are a number of adjustments to settings which need to be made in order to achieve the desired result. The integration procedure is highly sensitive to noise and thus an entire image should not be integrated but rather a region within that image should be focused on.

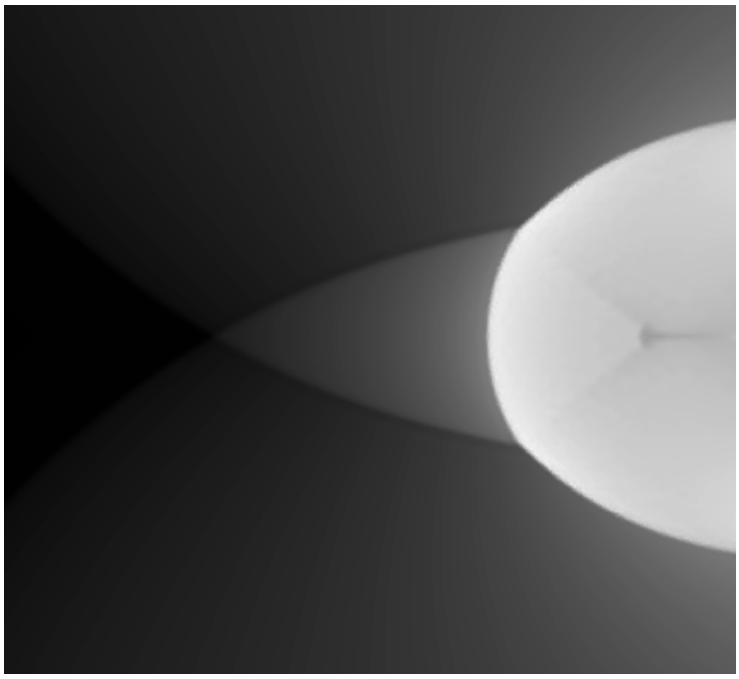
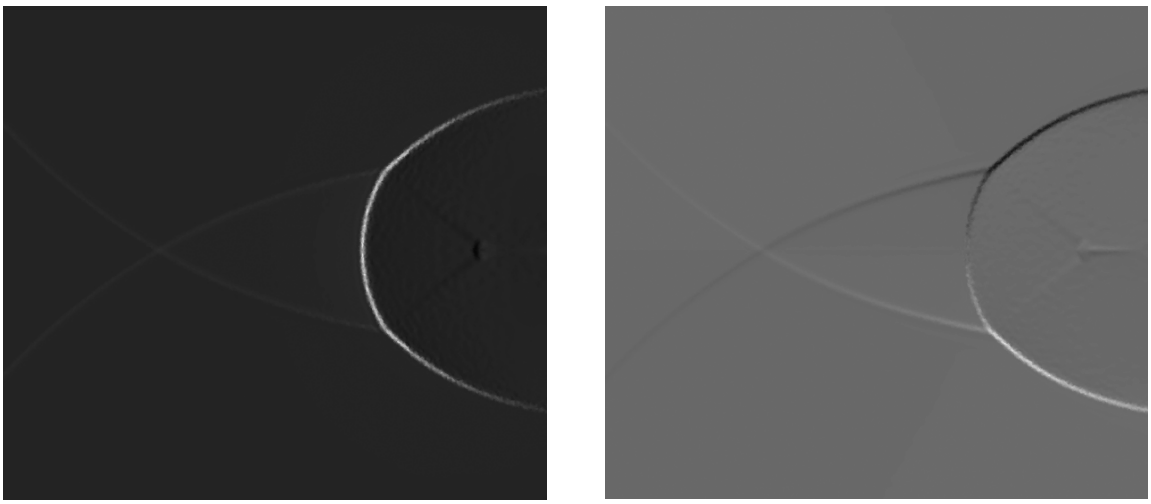


Figure 4.14: Original CFD density distribution image

As part of the design development, a CFD image was used to test the integration procedure, figure 4.14. The reason for using a CFD image is that during CFD computation, the density values are determined and not the density gradient. This means a density distribution image is readily available for comparison purposes. The image in question, figure 4.14, is the CFD density distribution after a shock wave of Mach 1.3 has interacted with a parabolic model. The parabolic model has been removed from the image since its boundaries would interfere with the integration process. The test model details may be found in section 5.5 and the CFD code used is discussed in section 5.4.1.

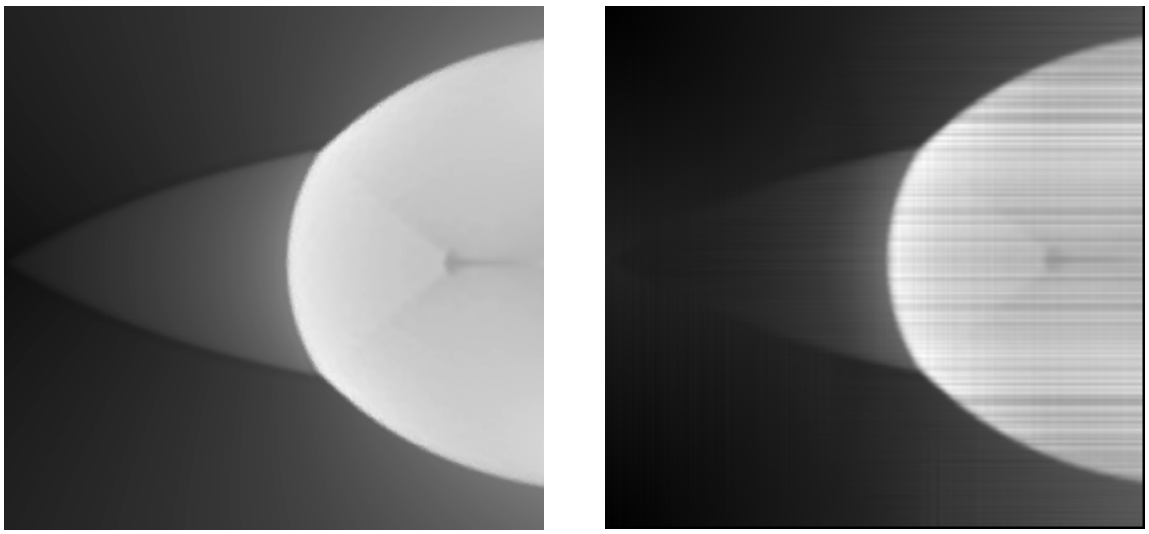


(a) (b)

Figure 4.15: Original CFD image subjected to a first degree derivation producing; (a) Density gradients in the x-direction; (b) Density gradients in the y-direction

The CFD image is subjected to a first derivation procedure thus producing a synthetic schlieren image outlining the shock waves, expansion and compression zones. The derivation procedure produces two images, one containing $\frac{\partial \rho}{\partial x}$ and the other containing $\frac{\partial \rho}{\partial y}$ information, figure 4.15. These two images are comparable to what a monochromatic schlieren system would produce with the horizontal and vertical knife edges.

The colour schlieren photographs taken of real flow regimes are dissected into their respective $\frac{\partial \rho}{\partial x}$ and $\frac{\partial \rho}{\partial y}$ images. These images are then subjected to this script and the outputted images discussed.



(a) (b)

Figure 4.16: Cropped and integrated CFD image (a) compared to similar region of original CFD density distribution image (b)

Once integrated, the image which is produced is compared to the original CFD image. This comparison is shown in figure 4.16 (a) and (b). It is quite clear that the images are not identical in construction, however the general form is similar as expected. The dynamic grey scale range of (b) appears to be reduced in comparison to (a). The most striking difference are the striations which are now present in the integrated density distribution (b). These lines are produced from pixel value rounding in conjunction with noise embedded in the CFD data. The image quality may be improved by using integration windows which are essentially smaller sections of a larger image. If the integration occurs over smaller regions, the extent and influence of noise will be reduced. One problem with this method is that the boundary conditions may become difficult to obtain if one such integration window is selected within a field containing significantly changing densities. It is possible to enter threshold values, blurring factors, reference densities and other settings from within the integration script. These settings drastically influence the image output.

This integration procedure is not specifically used in the viability analysis of the quantitative schlieren method however it has been included as a potential method to gain density distribution information from high quality experimental colour schlieren images. See Appendix B for code source files.

4.6 Optical ray-tracing

Two pieces of open source, GNU Licensed, software were used to gain an understanding of the optics used in this schlieren system, namely OpticalRayTracer (version 3.2 of 2010) and RayOptik (version 0.7.3 of 2003). The java based OpticalRayTracer software, by Paul Lutus, provided a visual insight into the behavior and characteristics of lenses. The main benefit of the software is that all calculations are done in real time and any modifications to the system appear as changes are made. Interestingly, the software takes into account dispersion and displays the different wavelengths of light refracting through lenses.

The more powerful RayOptik software, coded by George Beyerle, was designed for use with Matlab. The software allows for a large degree of freedom when placing optical components and works in 3 dimensions. Items such as mirrors, lenses, cutoffs and light sources can be configured to reproduce a variety of optical systems. Because Matlab is a script based language, the source files are readily editable and the flow of the software is quickly learnt. There are a lot of restrictions to the software in terms of the level of development however the general premise of the software was not to take measurements or use specific numerical results, rather gain an understanding of what might be happening optically and how to improve image quality.

Figure 2.11 is an example of the output of RayOptik and clearly shows the extent of coma in the optical system. Similar images can be compiled of the schlieren optics system and data entered for the various components. Because the software is still under development, and no accuracy is guaranteed, no decisions were made based on the outputs from the software. Both software packages are included on the DVD in Appendix B.

Chapter 5

Apparatus

This section describes all the apparatus and equipment used for the experimentation and numerical solutions.

5.1 Data Acquisition considerations

5.1.1 PC

The center of the Seitz tube operation is based around the PC and its operating software. The software, developed by TLC Software cc, controls and runs all aspects of the tube. The PC is equipped with two National Instruments (PCI-6110) and one (PCI-6224) Data Acquisition Cards (DAC's), which, via the software, monitor and control every sensor and actuator in the shock tube system.

5.1.2 DAC's

Each PCI-6110 DAC provides eight, 12-bit analogue input channels operating with a sampling rate of 5MHz [Instruments, 2004]. These cards are mainly used for the high speed requirements of the system such as the high speed pressure transducers, however, the temperature transducers are also connected via these cards.

The PCI-6224 DAC is mainly used for triggering events surrounding the tube such as the running of the hydraulic motors or triggering the light source. The card provides a combined total of 48 digital inputs or outputs and 32, 16-bit analogue inputs [Instruments, 2008].

5.1.3 Pressure and Temperature transducers

Ambient conditions are monitored by a low pressure transducer and a temperature transducer. They are mounted in the laboratory out of drafts, direct light or any other means which may influence their readings. The pressure sensor has an accuracy of 0.4 mbar while the temperature sensor is accurate to 0.25 °C [Seitz, 2001].

Pressure transducers in the compression chambers monitor the high pressure aspects of the shock tube. They are able to detect the rapid pressure changes induced by bursting diaphragms. The range of pressure to which the transducers can be subjected is 0 to 20 bar which matches the safe operating conditions of the Seitz tube.

High speed pressure measurement is achieved by PCB piezoelectric transducers placed within the expansion chamber. These signals are processed by the high speed DAC's and corresponding PC software to determine the Mach number of the shock wave as well as trigger the light source.

5.2 Shock tube considerations

5.2.1 Details

The Seitz automated shock tube was developed by Michael Walter Seitz during the 1990's in partial fulfillment of his Ph.D. [Seitz, 2001]. The tube is situated in the *Flow Research Unit* (FRU) in the *Mechanical Engineering Laboratory* (MEL) of the School of Mechanical, Industrial and Aeronautical Engineering, at the University of the Witwatersrand.

The automation of the shock tube is controlled by a PC and its connected data acquisition software. The original system was fully automated and included automatic camera shutter operation and diaphragm spooling. Software and hardware updates to the PC, tube and data acquisition systems have since resulted in many of these features to be non-functional.

A double diaphragm technique is employed in the Seitz tube to generate shock waves. User inputted data informs the software of the desired Mach number, the software then informs the user which grade of diaphragms to be used. The diaphragms rupture naturally and no manual pricking is required. A maximum Mach number of approximately 1.8 is attainable with an atmospheric pressure of approximately 0.83 bar.

Figure 5.1 illustrates the basic dimensions of the shock tube. The compression and intermediate chambers together make up the main driver and pressure vessel of the tube. The expansion chamber extends 6 meters, connecting the test section to the intermediate chamber end of the main driver.

The test section depth (along the optical axis) is 76mm while the effective height and width is 180mm and 450mm respectively. The glass has a visible diameter of 300mm although it

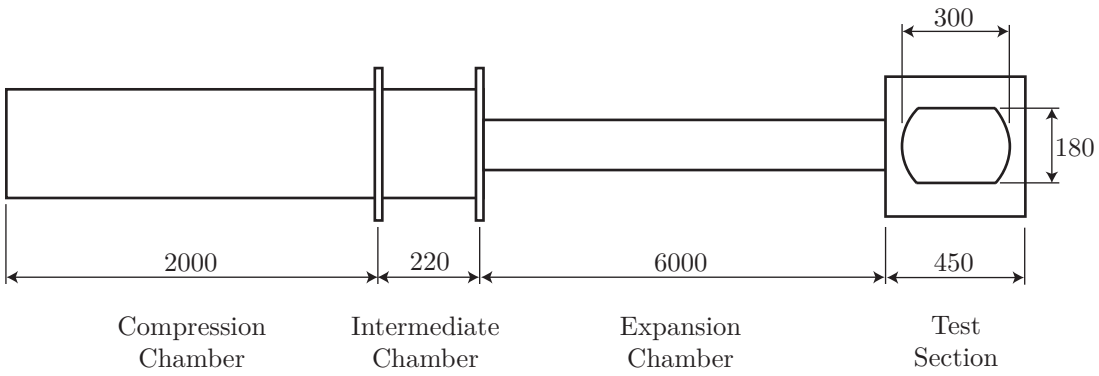


Figure 5.1: Schematic representation of the Seitz shock tube

is slightly larger than this to accommodate seating and positioning in the two doors. The test section is lined, with threaded ports for either pressure transducers or mounting test models. In this way, a large degree of customization in the setup can be achieved. Pressure transducer ports upstream of the test section allow for further sensors and monitors to be installed. Two high speed transducers are fitted to these ports to monitor the Mach number of the shock waves moving along the tube.

Diaphragms are placed at the intersection between the compression and intermediate chambers as well as between the intermediate and expansion chambers. These diaphragms are known as 'Diaphragm 1' and 'Diaphragm 2' respectively. The diaphragms are made of polyester and are available in different grades and thicknesses to allow for numerous combinations and thus different burst pressures and Mach numbers.

The main driver is actuated by means of a computer controlled hydraulic motor which slides the compression and intermediate chambers together for testing and apart for diaphragm replacement and cleaning. The internal dimensions are not constant along the length of the of the compression chambers as the cross sectional area decreases. The main compression chamber's circular cross section is contracted into a rectangular section with dimensions of 180mm x 180mm. The intermediate chamber then reduces this area further down to an area of 180mm x 76mm where the smaller dimension is the test section depth along the optical axis. The maximum operating pressure of the system is rated to 20 bar however the current laboratory pressure is limited to 15 bar and the system is operated on a regulated 5 bar pressure.

5.3 Optical considerations

The following apparatus breakdown comprises all the optical instruments used in the setup of the colour schlieren system around the Seitz shock tube. The general arrangement of the equipment is also discussed.

5.3.1 General arrangement

Accurate positions of each component are not strictly possible to obtain since the components are adjusted constantly to obtain the best image quality. All components are on the same vertical plane and care must be taken to accurately align the optical axis between components.

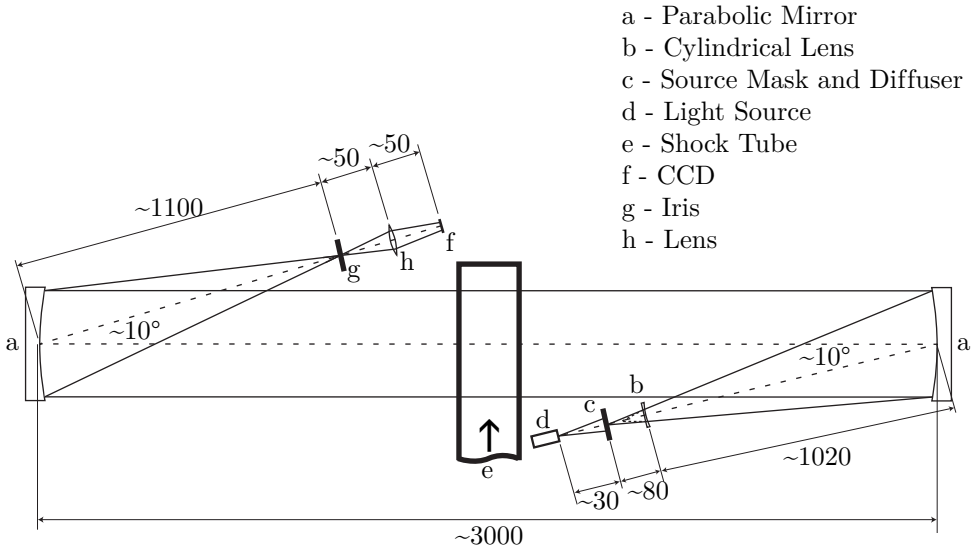


Figure 5.2: Schematic layout of apparatus in plan view

The general arrangement of the apparatus follows that of the standard Z-type schlieren system, figure 5.2. The indicated dimensions are approximate since the focal lengths of the parabolic mirrors differ from the values specified as well as from each another. The alignment and positioning of the optics is not simply by calculation but rather fine manual adjustment until the best possible image clarity is achieved on the CCD sensor.

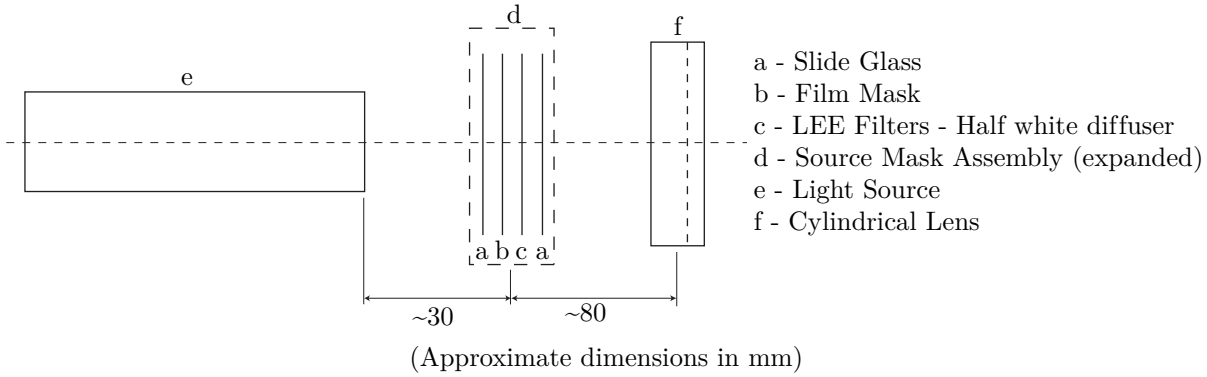


Figure 5.3: Light source schematic side layout

The light source of the schlieren setup is a crucial part of the optical system in terms of

optical clarity and system performance, figure 5.3. A number of light sources configurations were experimented with but the general arrangement remained the same. Since the system requires some sort of diffuser, the actual light source is positioned such that the maximum amount of evenly distributed light falls on the source mask film. Whether the LED light source or the xenon light source is used, the principle remains the same. Essentially the vertical plane in which the diffuser lies in acts as the new effective light source. The light traveling in the vertical plane passes unaffected through the cylindrical lens however the light in the horizontal plane is skewed and creates a virtual focal point just in front of the source mask to counteract astigmatism.

An important aspect, of the viability of this schlieren technique to produce quantitative results, is the range, resolution and magnification of the optical system. The experimental results are discussed in section 7.3. The range is described in sub-section 5.3.3.1. Magnification between source mask and iris diaphragm should ideally be kept to a minimum. Any magnification, whether enlargement or reduction, indicates the optics are not symmetrically arranged from the two schlieren heads. Image magnification occurs only after the iris, on the imaging sensor side, and the focusing lens is adjusted to fill the imaging sensor in order to obtain the highest image resolution possible. The system magnification is thus equipment specific, however, in this case the magnification from test section to imaging sensor was approximately 0.087. This means an imaging sensor image 11.5 times smaller than the actual test section.

5.3.2 Mirrors

The colour schlieren system employed around the Seitz Tube uses 254 mm diameter parabolic mirrors. The focal length is approximately 1100 mm which yields an f-number in the region of 4.33. The mirrors are both mounted on adjustable heavy base stands and can be positioned easily and relatively accurately.

5.3.3 Lenses

5.3.3.1 Calibration Lens

A large focal length plano-convex lens is used as means of calibrating the system as well as for a quantitative analysis.

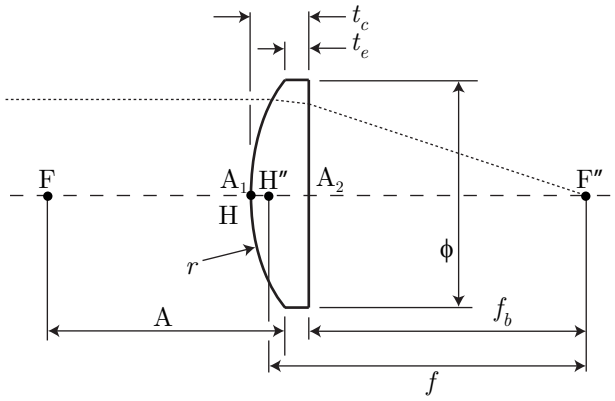


Figure 5.4: Calibration lens schematic

f [mm]	ϕ [mm]	f/#	f_b [mm]	t_c [mm]	t_e [mm]	r [mm]	f @ 523nm	f @ 633nm
10000.0	50.8	231.6	9995.8	6.4	6.3	5151.0	9915.8	10000.2

Table 5.1: Table of calibration lens data

Figure 5.4 in conjunction with table 5.1 outline the specifications of the calibration lens used. The optical material is laser quality BK7 glass with a surface figure of 10 - 5. The focal length is typically accurate to 0.5%.

The calibration lens allows the effective range of the system to be examined. In theory, by invoking equation 2.37, we find the calibration lens has the capacity to represent density gradients in the range from $0kg/m^4$ to $145kg/m^4$ for an air refractive index, $\eta = 1.001$ and a Gladstone-Dale constant, $k = 230mm^3/g$. This assumes the test section glass doors introduce negligible amounts of light deflection.

5.3.3.2 Cylindrical Lens

A cylindrical lens is used to correct for the schlieren system astigmatism which is generated by the parabolic mirrors being offset to the optical axis.

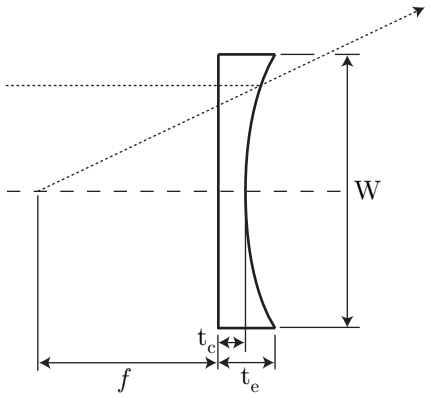


Figure 5.5: Cylindrical lens schematic

f [mm]	WxL [mm]	t_e [mm]	t_c [mm]	f_b [mm]	r [mm]
-300.0	30 x 30	5.0	4.3	-302.8	155.70

Table 5.2: Table of cylindrical lens data

Figure 5.5 in conjunction with table 5.2 outline the specifications of the calibration lens used. The optical material is laser quality BK7 glass with a surface figure of 20 - 10. The focal length is accurate to 3% at 546.1 nm. Dimension L is the length of the lens.

5.3.4 Cameras

The cameras used to capture images of the flow phenomenon varied between two digital SLR still cameras (Nikon D90 & Fuji S3 Pro) and a single high speed camera (Photron SA5).

5.3.4.1 Digital SLRs

DSLR cameras were used exclusively for single shots using either the LED or the Xenon light sources. For setup purposes, the Nikon D90 has a live view feature which in conjunction with the constant LED mode makes the results from any system adjustments clearly visible on the high quality LCD screen. Newer technology in the Nikon image processing CPU's also results in improved noise reduction, larger resolution and greater transfer speeds.

Digital SLRs have mechanical shutters and thus their maximum shutter speeds are limited to around 1/8000th of a second for top end models. This results in a different approach and additional equipment to capture a schlieren image. A pulsed light source defines the exposure of the flow field whist the camera is set to receive the pulse of light. The camera uses a mode known as bulb mode which allows exposure durations of up to 30 minutes.

The cameras ISO must be set according to the amount of light landing on the sensor. ISO settings of 400 to 3200 were used depending on the tests being conducted, light sources, exposure of the source mask film etc.

5.3.4.2 High speed camera

The high speed Photron digital camera was used in conjunction with the camera boot flash illumination system to produce video results using the colour schlieren system. Various settings are required to be set in order to achieve optimum results. Although the camera is sophisticated, it is still unable to capture full resolution video at frame rates above 7000fps. Resolutions above this threshold are reduced considerably as the frame rate is increased. A frame rate of 100000fps results in a frame being captured every $100\mu s$, which for shock wave research is inadequate as many of the flow phenomenon may have dissipated in that time. Frame rates in the region of 50000fps, which results in an image every $20\mu s$, are used

to capture the formation of finer flow details such as Von Karman vortices. This frame rate limits the overall resolution which can be dumped to 0.12 Mega pixels. Film resolutions are approximately 320x430 pixels for a frame rate of 46500fps [Photron, 2011].

The camera has an additional setting, partly controlled by the frame rate, which specifies the exposure time per frame. The minimum exposure time,$1\mu s$, is crucial to achieve a blur free crisp shock image. The exposure setting depends on the amount of light entering the system, hence the reason for the SLR boot flash as described in section 2.4.

5.3.5 Light sources

A number of different light sources have been used with the colour schlieren system with the intention to obtain the highest quality images possible. Each light source used exhibited characteristics which improved and degraded image quality and thus the best existing light source was chosen. The design and construction of an LED powered light source was also undertaken to improve cost efficiency and performance.

5.3.5.1 Xenon flash lamps

The Hamamatsu Xenon flash lamps used are modular and thus different bulbs can be used with different cooling jackets/shield cases and power supplies depending on what the requirements of the light system. The system is repeatedly triggered internally to aid in optical setup or switched to receive a TTL trigger input from the computerized shock tube systems.

The initial light source used employed a 1.5mm arc length Xenon flash lamp bulb (L2437) in conjunction with the shield case (E2608). The illumination pulse width, with the discharge capacitor set to $0.2\mu F$ and a discharge voltage of $1kV$, was the in the region of 1.5µs. This bulb requires an input power of 15 watts and outputs 0.05 - 0.15 J/flash. The power supply (C3684) for this combination outputs up to 1000 v Dc up to a maximum of 15 watts.

A larger 3mm arc length Xenon flash lamp (L6604) was used in conjunction with a cooling jacket (E6611) to dissipate any heat buildup within the lamp. The higher powered bulb required 60 watts of power input while supplying 1 J/flash optical energy output. A larger power supply (C6096) is required to cope with the additional power demands. The illumination pulse width was in the region of 2.9µs.

5.3.5.2 Continuous light sources

With the high speed camera unit setup, the illumination duration required is significantly longer than that which the single pulse xenon strobes can produce. Thus a semi-continuous or continuous light source is required.

High power halogen bulbs, approximately $50watt$, produce a significant amount of visible and infrared light, however, the large percentage of infrared light has the potential to damage

sensitive optical components and imaging sensors. Considerable caution should be taken when operating high powered continuous light sources in conjunction with powerful lenses around devices such as exposed CCD/CMOS sensors since a focused point of light will very easily destroy the sensitive equipment.

The design of the LED light source includes a continuous mode which, given the improvements to the Seitz tube software system, could provide a more accurate system for high speed camera work. The new routines allow the duration of the pulsed output to be controlled to within 1µs. This means the LED's illumination pulse could be used to provide light not only to the single image SLR capture method but also to the high speed camera capture method. Provided adequate heat dissipation, the LED's could remain on for setup purposes but at a lower current draw.

5.3.5.3 Semi-Continuous light sources

A semi-continuous light source is essentially a long duration flash lamp providing constant light output over thousands of microseconds. The Canon EX430 SLR flash allows a large amount of light to enter the high speed camera for various pulse durations and intensity levels.

This flash is by no means a point source of light as the flash tube within the flash unit is a few centimeters long. The light passes through a large adjustable focusing system and out through the flash head which has an area of around 10 square centimeters. The light intensity is directly proportional to its duration and is controlled directly by the power output setting on the flash unit.

The flash can be fired without the use of an SLR as the electrical circuitry within the unit operates on a simple switch mechanism. An electronic circuit,which was constructed in-house, closes the circuit by means of a MOSFET device after receiving a TTL trigger input. This simple circuit causes the flash to fire with virtually no significant electronic delays.

5.3.6 Stands & alignment aids

Due to the high accuracy required and the nature of optical systems, equipment which is stable, easy to adjust and modular has been installed for the Seitz shock tube. The equipment, supplied by Optosigma, includes the following:

- Optics rails which allow the translation of lens holders and equipment carriers along an axis. The rails are connected magnetically to the existing stands and are easily adjusted.
- Lens holders of different sizes are used to locate optical lenses centrally and without damaging the edges of the glass.

- A laser diode with a cross hair projection pattern. The laser can be placed at the focal point of the primary mirror and the beams can be followed through the system. This drastically improves the accuracy of any aligned optics as well as reduces time to set the system up.
- Micrometer adjustable, 3-axis equipment carriers are used to locate items such as SLR cameras, critically positioned lenses, light sources, source masks or iris diaphragms. All the carriers positions are lockable and are marked in millimeters which aids in the positioning or re-positioning of optics.

5.3.7 Iris Diaphragm

A finely adjustable iris diaphragm. The diaphragm can be mounted in a lens holder which in turn is attached to a micrometer equipment carrier. This combination allows very precise cut-offs to be obtained thereby improving image quality quite significantly. With an aperture ranging from 1mm to 20mm, the 12 bladed Optosigma mounted iris diaphragm allows precise adjustment of the light passing through to the imaging sensor. For testing, the iris aperture diameter should match that of the inner ring of the source mask diameter, measured vertically. Due to the systems optical magnification as well as the desired sensitivity level requirement, the precise aperture diameter cannot be stated herein, however, it should be approximately 6mm.

5.4 Numerical solution considerations

This section aims to detail the hardware and software aspects of the numerical solutions and simulations.

5.4.1 Software

A number of different software packages have been used to code, analyze or simulate various aspects of the research undertaken for this dissertation. Two pieces of C++ authoring software were used to generate the various sub-programs used in this dissertation. Visual Studio 2010 Express (VS2010E), freely available from Microsoft, and DevC++, freely available from Bloodshed Software, are used. Two different packages were used simply because Luke's code was complied in VS2010E whilst OpenCV was easier to compile in DevC++. Both environments are very similar interface wise and provide equal capabilities.

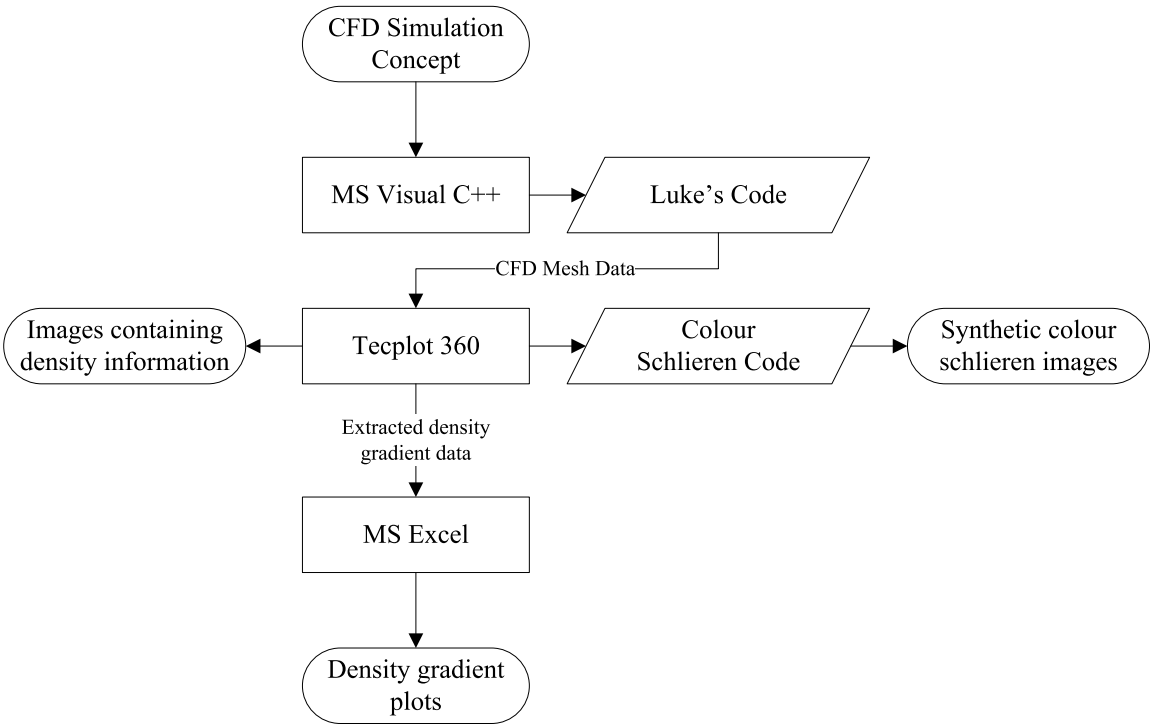


Figure 5.6: Flow diagram of software used to obtain colour CFD images

Luke's code is the result of a Masters dissertation complied by Dr Luke Felthun in 1995. The code, which is compiled in the C++ environment, is based on a Euler solver and allows both two and three dimensional simulations to be run, [Felthun, 1995]. A basic flow diagram of the inputs and outputs of the software is illustrated in figure 5.6.To date no attempt has been made to modify the code to allow for multi-thread computation which unfortunately results in extremely long simulation times.

However, the code has proven to provide accurate results. The software outputs a number of time stepped files according to predetermined settings within the model code. The files contain mesh data such as relative X and Y co-ordinates of the mesh nodes, density, pressure energy and velocities. This data is then analyzed and used to generate colour schlieren images, which can be correlated to experimental images.

Tecplot 360 (Build 12.0.0.4231 of 2009) is used to view the raw CFD files and to view the results from the colour schlieren script. The software has a number of inbuilt features which makes viewing the results of the CFD simulations easy yet somewhat powerful. Any of the CFD variables can be plotted as an overlay on the mesh, thereby making correlations between mesh quality and CFD results simpler.

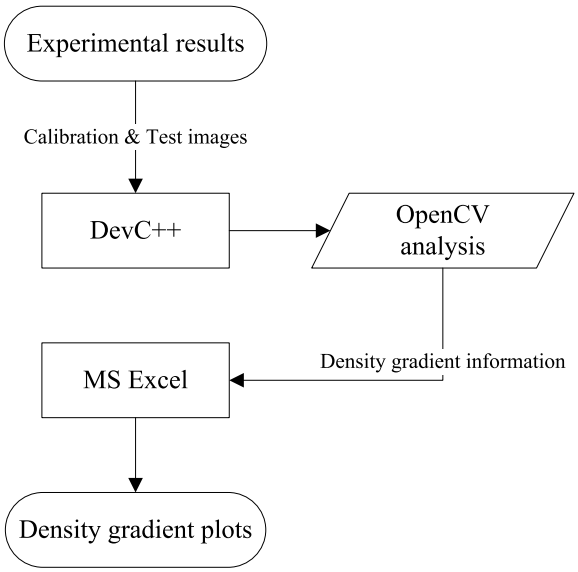


Figure 5.7: Procedure and software used to obtain quantitative density gradient plots

Software, generated in the C++ environment and using the OpenCV image processing library, automatically enhances both images equally to allow for quantitative evaluation. *Regions Of Interest* (ROI) in the experimental images can be selected and as this is done, the corresponding regions on the calibration image are highlighted. A flow diagram of the software inputs and outputs is shown in figure 5.7.Since calibration lens characteristics are coded into the software the density gradients magnitude and direction can be found for each point on the lens. See section 4.4 for more details on the exact use and coding.

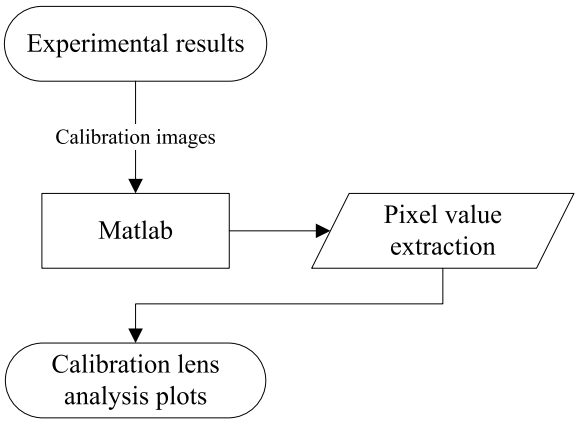


Figure 5.8: Use of Matlab to extract pixel information for calibration image analysis

Matlab (7.3.0.267 - R2006b) is used to generate the colour schlieren source masks and run the RayOptik open source software. It has numerous features which make the adjustment and modification of digital image data arrays simple yet powerful. In this way, the digital source masks can be accurately designed onscreen with short turnover times between any modifications as well as the visualization of optical systems possible. Matlab is also used to extract pixel value data from experimental calibration images in order to analyze the response of the lens to the light passing through it, this, is shown in figure 5.8.

Initially, Adobe Photoshop (CS5) provided the best platform to generate the source mask images, however, the requirement for more accurate source mask dimensions and quick modifications led to the use of Matlab. Photoshop was still used to modify and enhance experimental images when the colour schlieren system was under development.

5.4.2 PC

The hardware used to run the simulations, process image data, code various scripts and store the large amounts of CFD and image data was an AMD Athlon 64 x 2 Dual Core 5400+ personal computer. The CPU's were set to 2.8 GHz and it was running with 4.00 GB RAM. The operating system was Windows 7 64 bit Ultimate running on a 500 GB hard disk drive which provided ample storage space for the simulation and image data.

5.5 Test model

The test model which was used is a focusing parabolic reflection model. Milled from aluminium and polished, the model is designed to focus a given shock wave thereby generating high pressures and consequently large density gradient magnitudes. The symmetric nature of the model results in density gradients forming in all directions and this fact makes the model an ideal test piece for a omni-directional schlieren system.

Due to the symmetric nature of the model, the produced density gradient directions and magnitudes may be compared to one another in order to verify the uniformity of the schlieren systems sensitivity.

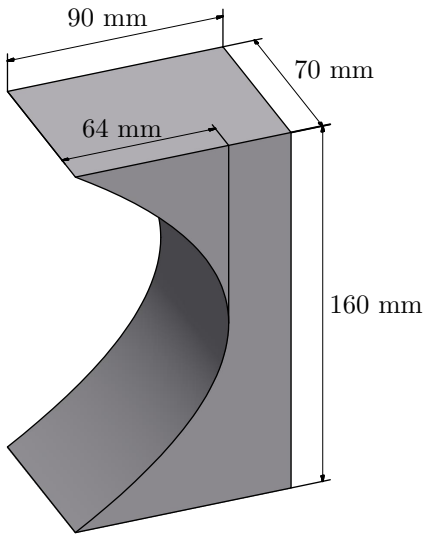


Figure 5.9: Test model

The specifications of the model may be seen in figure 5.9. The curved surface varies according to the function $x = \alpha y^2$ where $\alpha = 0.01$.

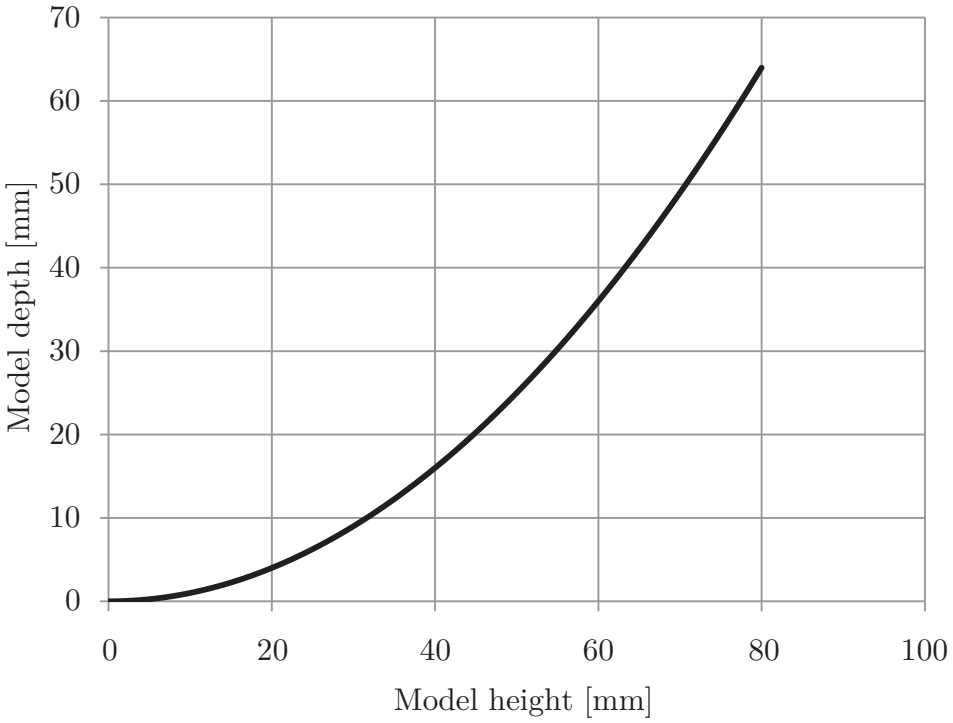


Figure 5.10: Model curved surface plot

Figure 5.10 shows the development of one of the faces of the surface curve, relative to the model depth and height. The curve in this instance is mirrored about the Y-axis to generate the part geometry illustrated in figure 5.9.

Chapter 6

Research Methodology

The experimental and computational procedures and precautions which were undertaken are presented in this section.

6.1 Experimental procedure

6.1.1 Overview

The following sections outline the experimental approaches and procedures taken as well as any pertinent repeatability considerations and precautions.

6.1.2 Light source

Part of this research topic was to investigate the efficacy of a high powered LED light source pulsed to replicate the effects of more conventional xenon flash lamps. A number of existing circuit designs were analyzed and tested in order to produce a more accurately defined square waveform light pulse.

Much of the development was not on the optical aspects of the light source but rather the electrical development of the circuit. Since the design and capabilities of modern LED's are changing on a daily basis, little research has been conducted on the effects of pulsing LED's with a significant current overload for short durations. For this reason, the research into developing a high intensity very short duration light source has predominantly been based on trial and error as well a visual inspection of the results of any light pulse tests.

The testing and design methodology was based on the following steps:

- Different LED configurations were assembled and tested and their relative performances noted for varying pulse durations. Ideally a light meter should be used to determine the exact amount of light produced for a given electronic setting. This would require a sophisticated and finely calibrated light meter which was unavailable during testing.

- A number of electronic adjustments were made to the way the LED was pulsed. It is however possible to vary the response of the LED with the voltage being supplied to the high power side of the circuit. The voltage supplied to the LED causes the current drawn by the LED to increase quite significantly and therefore increase the luminous output of the diode. A range of voltages were selected and the current was monitored for a given LED. A visual inspection of the intensity of the light and the hue of the light was compared to the standard xenon flash lamps as a reference.

- An oscilloscope was used to monitor the pulse waveforms produced by the circuitry to ensure the pulses were being produced correctly and accurately. The circuitry was adjusted and set to produce pulses with exactly $1\mu s$. The oscilloscope was also used to monitor the voltage over a 1Ω resistor as this allowed the current being drawn by the LED and pulled through the MOSFET to be observed and tuned.

- When the circuitry settings were as fine tuned as possible, the light source was setup around the test section and aligned with the optical apparatus. A number of images were captured of the test section with the calibration lens present. Each image was captured with varying ISO sensitivity settings to determine whether the light source had the required power and spectral distribution capabilities to produce a high quality schlieren image.

Precautions

- The LED supply voltage must be set and monitored closely since there is a risk that the maximum operating voltage and current of the LED will be exceeded for such low duty cycles. If there is a circuit switching malfunction, the LED may be forced to remain on and be subjected to a voltage which exceeds the maximum allowable for the particular LED and cause components to burn out including expensive high power LED's.

- As with any sensitive circuitry and IC's there is a risk of *Electro-Static Discharge* (ESD) damaging or destroying the components. For this reason, caution must be taken to handle the more sensitive components with care and avoid touching exposed components unnecessarily.

- Short circuiting components may not only damage the said component but may damage a significant portion of the circuit in the process. If any short circuits are found or suspected, all power should be removed and a full inspection of the circuit conducted to avoid expensive mistakes.

6.1.3 Source Masks

The source masks construction process unfortunately involves a fairly large degree of variation. The digital design process is relatively flawless since the digital images are saved in a loss-less format however in the printing process, reproduction errors are unavoidable. The following procedure is follow to produce the source masks:

- The digitally produced images are sent for printing and a transfer to photographic media. After high *Dots Per Inch* (DPI) prints are produced, they are attached to a photographic air wall and illuminated as evenly as possible without introducing any reflections or shadows.
- The printed images are then photographed onto low 100 ISO fine grain Fuji film. This part of the development of the source masks is particularly difficult since the exposure of the camera needs to be perfect to get the black regions of the masks suitably black whilst accurately reproducing the colours. A number of exposures of each source mask are taken in order to compare and choose the most accurate slides.
- Comparing different types of source masks means the system should be aligned and setup in exactly the same way each time. The slides were placed in the slide holder as close to the previous slides position as possible. A test image was then captured with the calibration lens in the test section and this allowed for the comparison of the various source masks.

Precautions

- The source masks were designed according to the schlieren system thus once the source masks are finalized, the schlieren system cannot undergo any significant adjustments or modifications
- Printing the images and capturing photographic replicas will introduce colour distortions and as such will result in non verbatim copies of the digital images. This is one of the main reasons the colour hues generated by the calibration lens are analyzed.
- Another issue during the photographic reproduction of the masks is the barrel distortion introduced by the camera lens which was used to transfer the printed images to film. If a significant amount of distortion was introduced, the source masks would no longer suit the schlieren system and would result in the background illumination being uneven and/or varying sensitivity with direction.
- The alignment of the source mask on the camera film is visually centered through the view finder of the camera and is by no means the most accurate method of alignment. A similar issue is the placement of the film segment in the slide holder as the position of the film is not absolute.

6.1.4 Seitz shock tube

A brief overview of the procedure and precautions of running tests using the Seitz Automated shock tube is given in this section. The development of an accurate quantitative colour schlieren system to analyze domain characteristics within a compressible flow field required a shock tube system to generate repeatable flows as well as predictable shock patterns. Digital SLR still cameras were used to capture the images of the flow field in high resolution. Since the shock or flow field characteristics themselves were not of particular importance, the quality of the image obtained was prioritized and for this reason, still images were not necessarily captured at regular intervals.

The majority of the shock tube functions and operations are automated and thus it is important to ensure the various sensors and monitors are functioning correctly before any tests are conducted. The sensor data is relayed through the PC terminal to allow the user to confirm any readings and monitor the system. The imaging system composing of the light source trigger output can be manually triggered in order to capture calibration images and test the alignment of the optics before a shock test is run.

The following list is not exhaustive however the main operation of the shock tube is outlined:

- The shock tube operates on the laboratory's 15 bar compressed air supply and thus the level of the compressor reservoir needs to be of a sufficient level to correctly run the system. Compressing of the reservoir takes a few hours and could delay testing or produce incorrect results if not checked regularly.
- The shock tube systems have been changed and modified over the years and as such there are number of quirks with the electronic system. All components, including transducer amplifiers; signal conditioners; DAC's and PC's, should be switched on a few minutes prior to testing. This allows the system to achieve a stable temperature and state before commencing testing.
- The shock tube has a multitude of transducer ports running down its length and these ports should be double checked, before testing, for any loose fittings. The tube also has a number of mounting options for the models which are installed in the test section. The holes which are not used for the model mounts should be plugged with the appropriate bolts and the smoothness of the surface in the test section, surrounding the flat surface of the bolt, checked.
- The model must be mounted accurately and securely and caution must be taken when positioning the model so as to not damage or scratch the test section glass surfaces. As the model is tightly secured, the gaps between the model and glass doors should be approximately the thickness of a standard piece of paper. There should be no pressure exerted by the model on the glass doors as this may result in significant damage to either of the glass doors.
- Once the model is secured, the test section should be cleared of all dust and prior testing diaphragm fragments. This may be done by inserting high pressure air at the diaphragm position and blowing out any foreign objects towards the test section.

- The doors are to be secured using all three bolts to a torque of approximately 50Nm.
- The diaphragms are loaded into both positions with a thickness specified according to the test Mach number which is desired.
- When the shock tube system is ready and all personnel are clear from the operating mechanics of the compression chambers, the test may be commenced. Various electronic settings are requested by the controlling terminal, the most pertinent being the delay of the light source trigger. Once all configurations have been made, the tube will run automatically.
- Once the test is completed, the system will request the tube to be vented and the compression chambers will once again open, ready for the next test cycle.

Precautions

- It is important to frequently monitor the optical system as any bump or movement of any optical component will drastically alter the readings or images captured.
- Not completely venting the system prior to opening the compression chamber may be dangerous as there will still be air pressure within the tube.
- The tube should be cleared of fragmented diaphragm debris after each test however it is possible to complete at most 3 tests before fragments begin to appear in the test section.

6.1.5 Repeatability considerations

The shock wave interactions and flow characteristics are not themselves the central study of this research but rather the performance and efficacy of a colour schlieren system. It is important that the flow characteristics are of a nature such that they may be analyzed using such a system however, the repeatability of the shock tube is perhaps more important. For images to be compared with different adjustments and optical configurations, the flow regime must remain as constant as possible.

The xenon light sources when used for colour schlieren work are highly repeatable however when used with monochromatic systems, the light producing electric arc has a tendency to sway from side to side in the unit itself. The degree of movement may be relatively small however, this movement may influence the optical sensitivity if the arc is not aligned perpendicularly to the knife edge cut-off. Since the colour schlieren system relies on a source mask and diffuser, the sway of the light has no effect on the optical sensitivity.

6.2 Computational procedures

6.2.1 Overview

The computational procedures involved all the numerical simulations, programming, analysis and comparisons.

6.2.2 CFD

The CFD software is particularly versatile in that many adjustments can be made to the code to produce the desired mesh complexity, accuracy of the solution and various data logging features. The following subsections outline the adjustments made to the software to produce the CFD results which were used to validate the experimental colour schlieren images.

6.2.2.1 Solver

The inherent CFD solver is specific and cannot be modified significantly. Euler equations are used as the set of equations to govern the inviscid flow by conservation of mass, energy and momentum. Various software variables are set according to desired outputs and are listed below:

- The domain of the solution is listed as a maximum number of mesh cells. This value gives an indication of the maximum possible cell density for a given geometry.
  - EulerDomain = 1000000
- The ratio of specific heat, Gamma γ, of the gas at a constant pressure to heat at a constant volume which happens to be 1.4 for air.
  - s.gamma = 1.4
- The density of the air, Rho ρ, matched to the local air density conditions.
  - rho = $0.981 kg/m^3$
- The local ambient air pressure, Pressure P, matched to the local conditions.
  - pr = 83200 pa
- Mesh initial velocities for moving mesh simulations. These variables are both set to zero as no moving meshes are used for these simulations.
  - u = 0 m/s
  - v = 0 m/s

- The incident shock Mach number, M, is specified as per the average experimental test Mach number returned by the shock tube software systems.
  - m = 1.33
- The local speed of sound, a, is specified according to local temperature and pressure conditions.
  - a = 340.294 m/s
- Initial maximum and minimum cell sizes are defined to begin the simulation. Once the simulation reaches a desired threshold point, the values can be redefined to produce a finer or coarser mesh to suit the simulation and improve efficiency.
  - s.hMax = *percentage of a specific geometry dimension
  - s.hMin = *percentage of s.hMax
- Code has been included to allow for dynamic mesh adaption during the simulations. The mesh is improved and refined according to basic criteria such as the maximum pressure difference between cells.
  - p4 = 0.04 pa
- The Courant Friedrichs Lewy condition is initialized relatively high to capture shock at inlet, but can be reduced after a specified time or threshold to speed up the simulation.
  - cfl = 0.3

A few other variables are specified according to the desired number and rate of files to be outputted, the total simulation time and mesh adaption criteria.

6.2.2.2 Mesh

Using the variables discussed in section 6.2.2, the software automatically generates an initial mesh over the domain.

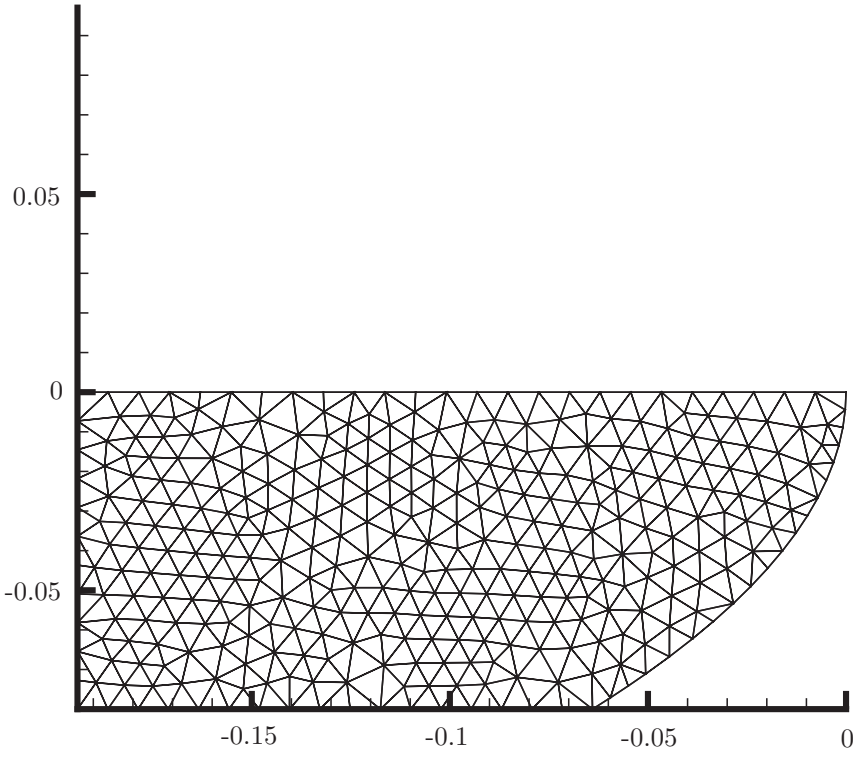


Figure 6.1: Initial mesh conditions

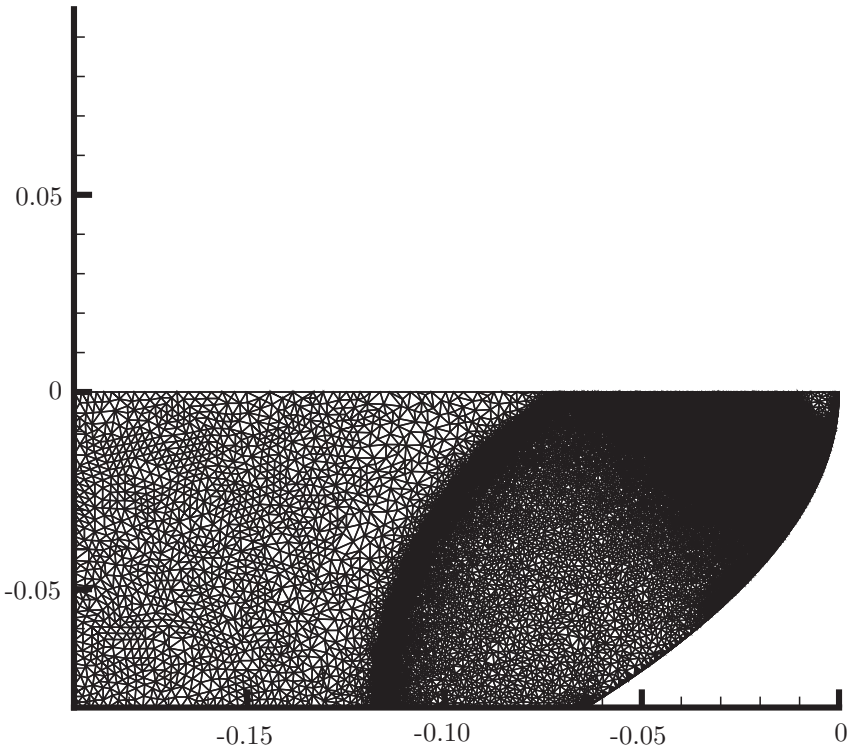


Figure 6.2: Refined mesh

An example of the the initial mesh generated by the software is illustrated in figure 6.1. The number of points and elements at this stage are 346 and 618 respectively. The mesh which used 0.000512 seconds into the simulation is shown in figure 6.2. The number of points and elements in this refined mesh are 30544 and 60386 respectively. It is therefore clear how the software has adjusted and refined the density of the mesh according to the local pressure gradients. This allows the software to run more efficiently with a leaner mesh structure.

6.2.2.3 Precautions

There are few precautions to heed before running CFD simulations, the following list outlines a few important points:

- It is advised to check the geometry before allowing a simulation to run until completion. The obvious reason for this is that if the geometry contains errors then the simulation technically means very little to wards a final converged solution.
- The mesh settings will influence the final results and thus the initial mesh and the mesh refinement schemes should be monitored for their efficiency as well as their ability to produce repeatable results.
- The initial conditions at the inlet, including the Mach number, pressure and air density should match the local conditions surrounding the experimental rig as closely as possible. This is since the CFD results are required to validate the experimental results and vice versa.
- Ideally, a number of simulations should be conducted with a variety of mesh configurations to self-validate the CFD results. This method will reduce the likelihood of a mesh induced error and thus allow a relatively good set of data for experimental results validation.
- Unfortunately, the CFD code is not refined for use with multicore systems and thus is relatively slow to solve simulations. It is advised to run the CFD code on a machine with the highest possible single core speed to resolve the solutions the fastest. The code does not allow saving of and continuing the simulation at later stages so prematurely stopping the simulation will result in the simulation having to be restarted from the beginning.

6.2.3 Source mask generation

The source mask design is conducted in the Matlab environment.

- Procedure:

- The first stage of the source mask generation is to determine the minimum schlieren system angle which can be used for experimentation. This angle is crucial to determine the astigmatic difference between the sagittal and tangential focii and in conjunction with the cylindrical lens focal length, the distortion ratio of the source masks may be determined.
- A -300mm focal length cylindrical lens and a schlieren system angle of 10 degrees are specified
- The desired colour arrangement and the relative positions of the colours are specified as well as the option to grade the colour intensity depending on the radial position from the center of the source mask.
- The script is run and the final source mask images are saved in a loss-less tiff file format which introduces zero image compression and allows for the best quality prints.
- The images are then sent for high resolution printing, see subsection 6.1.3. See figure 4.2 for the possible combinations.

There are a few limitations to the script thus far which are outlined below:

- Limitations
  - The size of the source masks are currently limited to the frame size of standard 35mm film. It is possible to modify various ratios and sizes within the script to allow for different sized film to be used.
  - The software does not allow for easy modification of specific colours in the continuously blended colour mask. If, for instance, a hue of magenta did not replicate correctly during the photographic procedure to produce the mask, the digital image could be modified in such a way so as to produce the correct hue during physical production. Matlab uses colour maps which are applied to the digital source masks and perhaps these maps could be modified to correct for incorrect hues.
- Precautions
  - The generation of the digital source masks are based on the image capture of a Matlab plot. As such, the initial image which is captured has a border around the source mask which need to be cropped in order to produce a symmetric image. There are variables included in the script to take care of this, however, on a system with a larger screen resolution these variables may be required to be modified.
  - The optical considerations employed in the script to generate the source masks in a distorted fashion are based on simple optics. There are likely to be more complex optical aberrations which have not been incorporated into the software and thus for any new schlieren setup it is recommended to place a perfectly circular aperture in the source mask plane, include the cylindrical lens and place the imaging sensor in the final cut-off plane. This will produce a distorted image

of the source mask in which the exact distortion ratio may be extracted and applied to the new source masks. This method allows for a precise measurement of the source mask distortion as well as the source mask colour reproduction to be analyzed.

6.2.4 Synthetic schlieren generator

This script operates from within the Tecplot environment and requires specific variables to be embedded into the solution files.

Procedure:

- A simulation is run using CFD software, namely Luke's Code. The software outputs a number of time stepped files which contains all the relevant data including variables and the mesh structure. This file is then loaded into Tecplot.
- The colour schlieren script may be modified to a certain degree to output specific results to match experimental conditions. Some of the features of the script adjusted to allow for validating of the experimental results are:
  - The rotation of the colour hues through 90 degrees was required to obtain an adequate correlation between the experimental and computational results.
  - The colour representation was flipped about the Y-axis, again to match the experimental results.
  - The upper and lower density gradient magnitudes were fine tuned to provide the most accurate results and emulation of the experimental results.

Limitations:

- The script works specifically with symmetric flow simulations however, it could be modified to accept non-symmetric geometry.
- The code is scripted and thus it is inherently slower than raw code to produce synthetic colour schlieren results.
- The thresholding system used to improve the visual quality of the images is perhaps not as refined as it could be and thus a more advanced algorithm may be devised to reduce density gradient noise.

Precautions:

- It is important to note that the results which are presented visually have been derived from CFD data. This infers that there will be a significant increase in data-noise present in the final images.
- No provisions have been included in the code in the event of alterations to the Luke's code format of the raw CFD data files. As such, the synthetic colour schlieren code may not function correctly, or at all.

6.2.5 Comparison software

The validating and comparison software is based in C++ and operates using an open source image processing library called OpenCV. Refer to section 4.4 for more information on the workings of the software as well as screen shots.

Procedure:

- The software is not fully automated and thus a C++ environment is required to use the software and make variable adjustments. From the C++ interface, the following specifications may be modified:
  - The file paths pointing to the location of both the calibration and test images.
  - A percentage the images are to be scaled/reduced by so as to fit them on one screen.
  - To help combat noise in the images a simple Gaussian blur is applied to the images. The pixel area over which the blur is created may be specified in order to enhance or reduce the effects of the blur.
  - There is an option in the code to threshold or posterize the images. This helps to enhance the contours of the changes in hue and intensity within the images.
- Once the images are loaded, the user is required to position a circular mask over the calibration lens image.
- As the user selects regions of interest on the experimental test image, the corresponding regions matched by hue and hue intensity are selected on the calibration lens image. It would be required that the user adjust the thresholding bars in the experimental window to reduce the size and number of selected blobs in the calibration window.
- Once the desired region has been fine tuned, the mouse cursor would be positioned over the selected blobs and the relative information would be outputted to the command window. This information may then be plotted in a third party application.

Limitations:

- OpenCV programmers are still refining the blob detection library at the time of writing and thus this feature has not been implemented into the code. Essentially, the feature would allow the location of a given blob to be automatically detected in conjunction with details about the blob such as mean pixel values, total size etc. This would thus negate the step requiring users to move the mouse cursor over the selected blobs, instead, the blobs location could be automatically stored and plotted internally by the software which would be far more efficient and accurate.
- Unfortunately, due to codec issues, the software is unable to read RAW file formats directly. The images are required to be converted to a standard Jpeg or Tiff file format before using the software.

Precautions

- It is important to vary the variables by a small amount each time. The OpenCV software is constantly under development and bugs are found and fixed regularly.
- It is important to position the circular mask over the calibration lens to correctly size the mask. Once the mask is sized correctly, the position of the mask should be such that the dark spot of the calibration lens coincides with the center of the circular mask. This is to make sure that the region of zero density gradient on the physical calibration lens matches the region of zero density gradient on the circular mask.

Chapter 7

Results and Discussion

This chapter details the observations, results and a discussion of all the experimental and numerical procedures conducted.

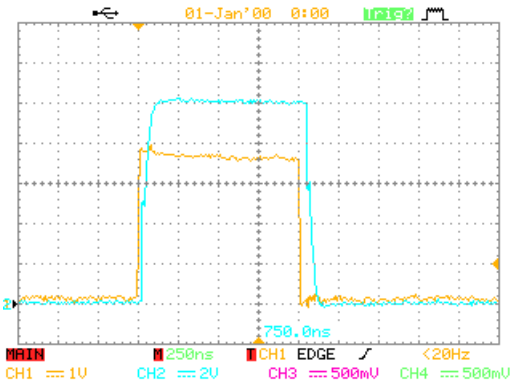
7.1 LED light source

The concept of a high powered, microsecond pulsed LED light source is discussed in this section. The various results, observations and circuits will be detailed as well as the final specifications of the circuit.

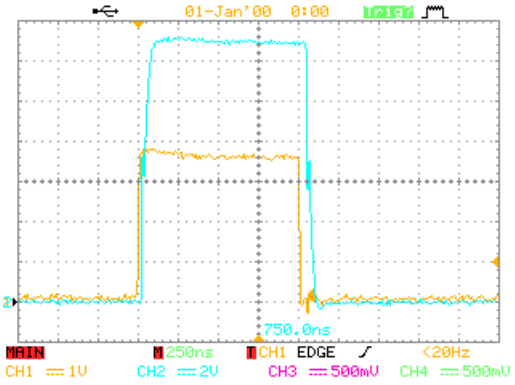
7.1.1 Circuit performance

The results in this section illustrate the performance of the circuitry. A number of systematic tests were run whereby components were changed one at a time and the results monitored. This method of testing allows the performance of each component to be analyzed and thus the effect of the component on the circuit as a whole may be determined.

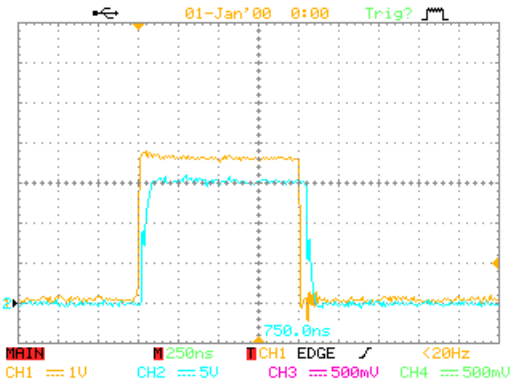
Refer to the sub-figures in figure 4.3 for the relevant oscilloscope connection points mentioned herein.



(a) 10v Supply



(b) 12.5v Supply



(c) 15v Supply

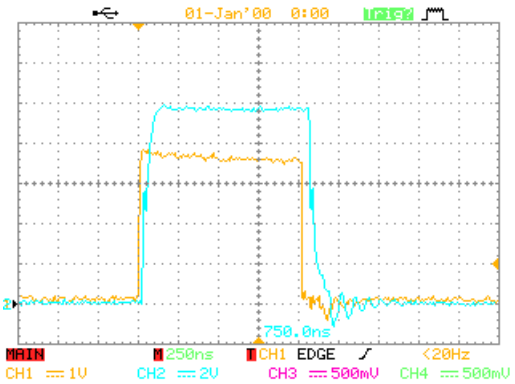
Figure 7.1: 4427 IC and 74121 IC voltage outputs for 3 supply voltages with no load circuitry connected

The voltage output from the 74121 IC (CH1) as well as the voltage output from the 4427 IC (CH2) for 3 different supply voltages is presented in figure 7.1. The oscilloscope is connected to point A for channel 1 and point B for channel 2 with the shield grounded at point E. No additional loads other than the MOSFET are connected to the output of the 4427 IC and these results purely reflect the outputs from the pulse generating IC's. A $100k\Omega$ resistor is used to connect the gate of the IRL520 MOSFET and pull any stray voltages and fluctuations down to $0v$. The source pin of the MOSFET is connected to ground by means of a $1k\Omega$ resistor only whilst the drain of the MOSFET is not connected to anything except the oscilloscope,

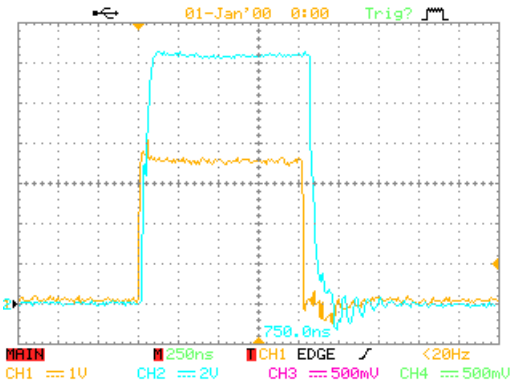
It is apparent that the 74121 IC is repeatedly outputting between 3.7 ~ 3.8 volts to the input of the 4427 MOSFET driver IC regardless of the input source voltage. The total pulse duration as specified by the resistor and capacitor combination is set to $1\mu s$ for this and all further tests. This pulse duration would allow for a crisp clear image with little blurring at the Mach numbers being investigated. The rise and fall time of the 74121 is in the region of $30 \sim 40ns$ as specified in the IC documentation. These times are illustrated in the measurements as virtually no pulse lag may be noticed on this scale. The waveform is almost square however, there are oscillations being produced from the output of the IC when the pulse completes.

The 4427 IC is outputting the corresponding source voltage up to a safe maximum of 15v without a regulator monitoring the voltage supplied to the 4427. There is a shift in the pulse to the right indicating a marginal pulse delay in the region of $50 \sim 80\mu s$. This delay is introduced by the 4427 IC and the associated wiring. The produced waveform from the 4427 is not as square-like as the 74121 as the rising edge tends to bend towards the peak of the pulse. A similar thing occurs during the end of the pulse falling edge, the pulse has a tendency to spread out. These characteristics of the 4427 are generated by the internal circuitry attempting to control the pulse width as accurately as possible and avoiding under or over damping the signal.

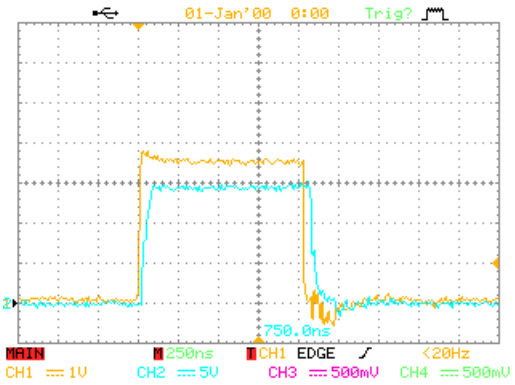
There is no significant difference between the waveforms for the three voltages tested other than the output voltage reflecting the level of the source voltage.



(a) 10v Supply



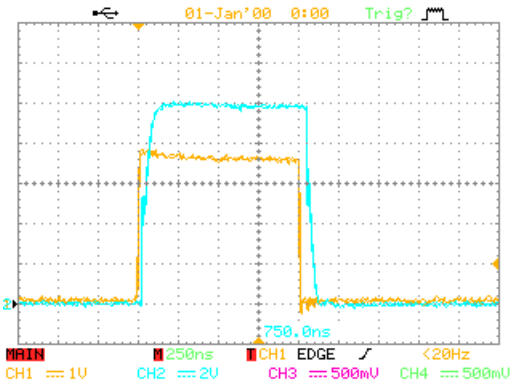
(b) 12.5v Supply



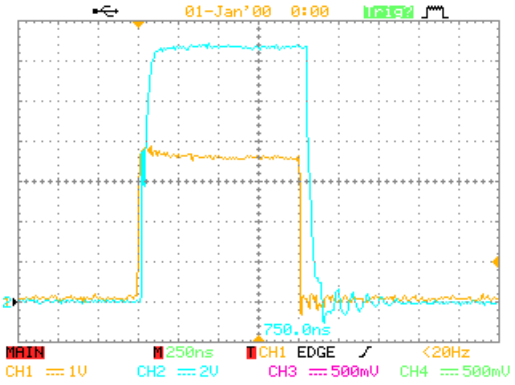
(c) 15v Supply

Figure 7.2: 4427 IC and 74121 IC voltage outputs for 3 supply voltages with the 9x9 LED array connected

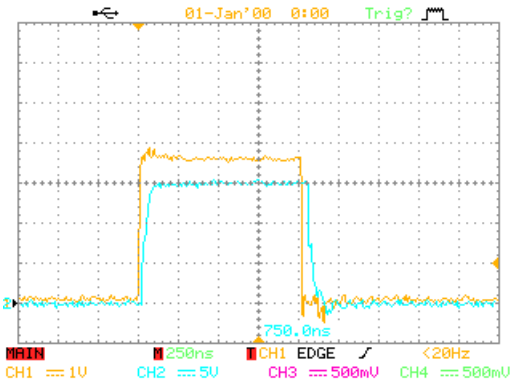
Figure 7.2 shows the voltage outputs from the two pulse generating IC's for the 9x9 LED array. The circuit and connections are exactly as per the initial tests however, now the LED's cathode has been connected to the MOSFET drain pin. The only significant visible difference in the IC chip outputs is the extent of the voltage oscillations once at the falling edge of the pulse. The intensity of the oscillations seems to increase with the supply voltage. There is little to no difference in the offset delay of the pulse outputs when connected to this LED array.



(a) 10v Supply



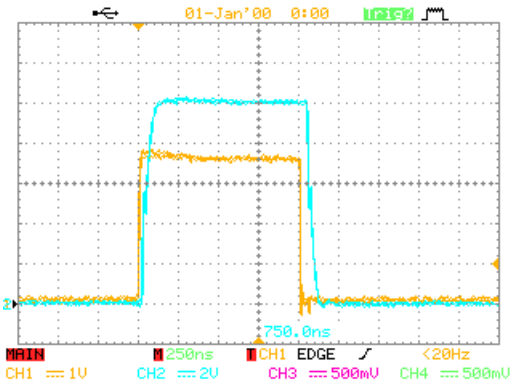
(b) 12.5v Supply



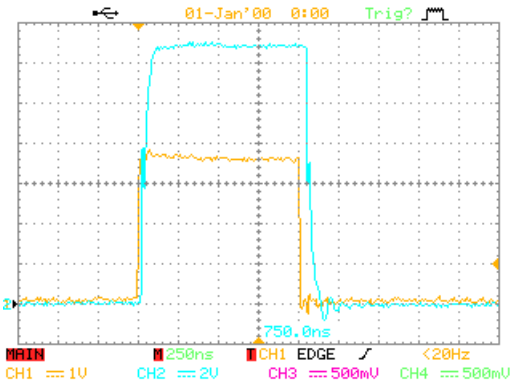
(c) 15v Supply

Figure 7.3: 4427 IC and 74121 voltage outputs for 3 supply voltages for the single Cree MC-E LED

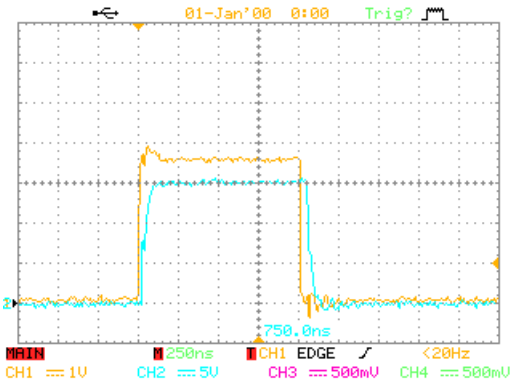
Figure 7.3 shows the voltage outputs from the two IC's. note the oscillations when the gate is closed. the outputs are for the single Cree MC-E LED. Again, very little difference between the initial no load conditions and these LED conditions may be noticed.



(a) 10v



(b) 12.5v

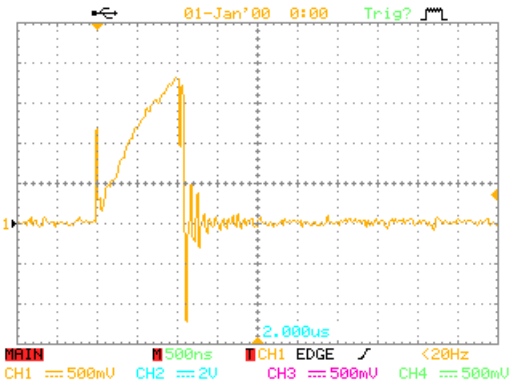


(c) 15v

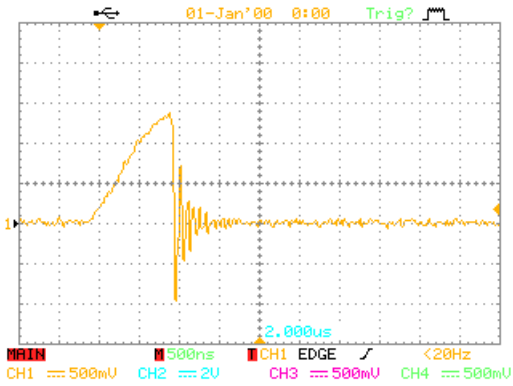
Figure 7.4: 4427 IC and 74121 voltage outputs for 3 supply voltages for the Cree MC-E LED array

Figure 7.4 shows the voltage outputs from the two IC's. note the oscillations when the gate is closed. the outputs are for the 3 Cree MC-E LED array. The larger powered LED array has very little influence on the output of either IC chip.

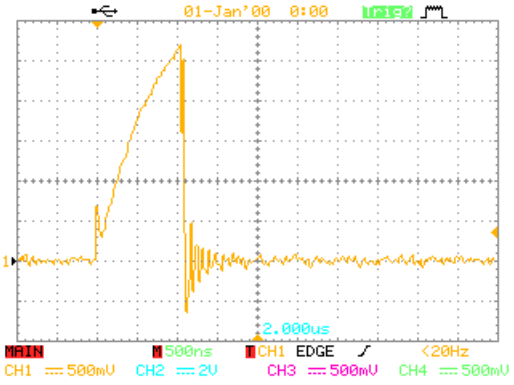
We can deduce from this, and the previous tests regarding the fluctuation of the IC chip outputs, that the quality of the signals from both IC chips should not deteriorate by any significant amount provided the source power supply has the capacity, in terms of current, to supply the demands of the LED's. The only significant effect the different LED's had on the IC outputs is the degree of oscillation when the pulse ends.



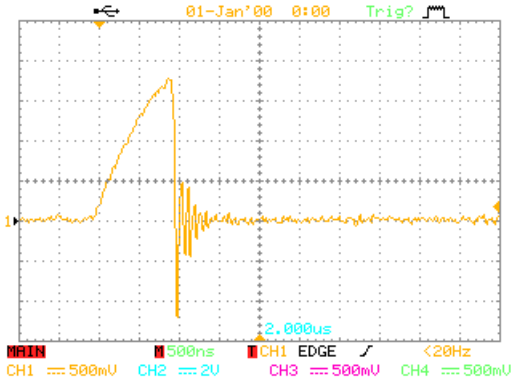
(a) 10v with 4427 driver



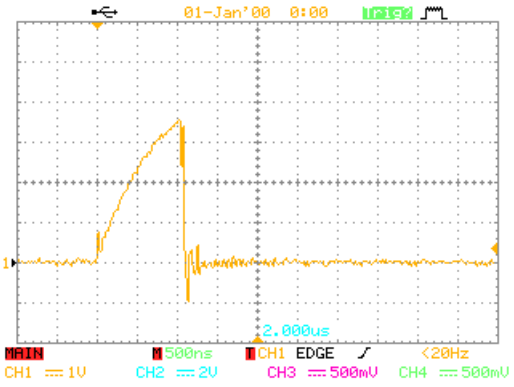
(b) 10v without 4427 driver



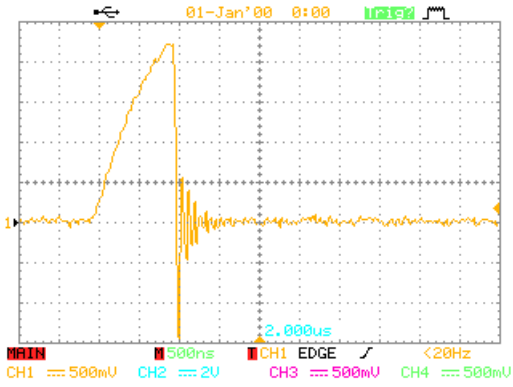
(c) 12.5v with 4427 driver



(d) 12.5v without 4427 driver



(e) 15v with 4427 driver



(f) 15v without 4427 driver

Figure 7.5: Current draw for the 9x9 array

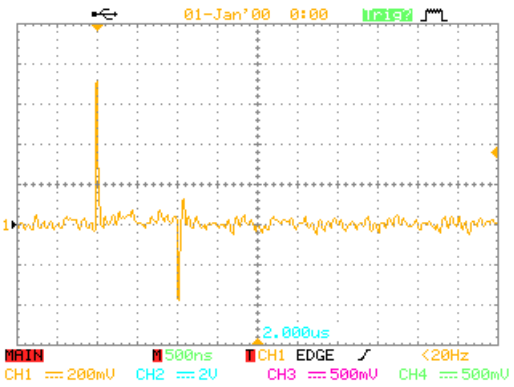
The circuit uses the 74121 IC and the 4427 IC to generate and boost the signal respectively. The 4427 is a MOSFET driver since it will activate upon receiving a low input voltage and supply a much larger voltage. It essentially acts as a solid state relay and switches the source power to drive the MOSFET instead of the low voltage from the 74121 IC.

Figure 7.5 illustrates the effect the 4427 IC has on the current draw by the connected 9x9 array of LED's for 3 different voltages. The oscilloscope monitor is connected to point C with the shield grounded at E. This arrangement allows the oscilloscope to measure the voltage drop over the 1Ω resistor R4 and thus the voltage recorded may be directly converted to the

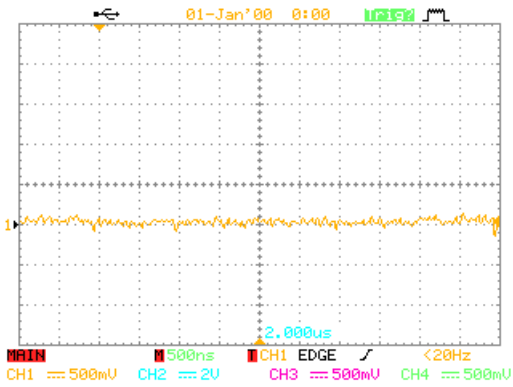
amperage flowing through the connected LED.

Supply Voltage [volts]	Without 4427 [amps]	With 4427 [amps]	Percentage Gain [%]
10.0	1.40	1.75	20.0
12.5	1.75	2.75	57.1
15.0	2.25	3.50	55.5

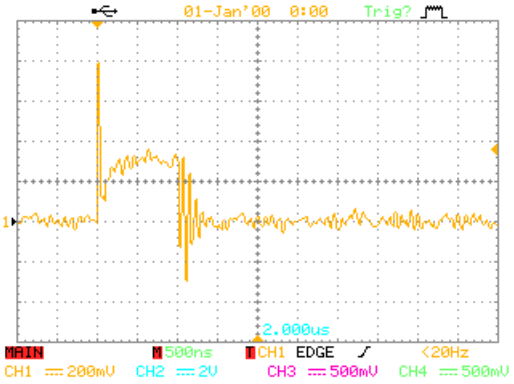
Table 7.1: Table comparing the amperage drawn by the 9x9 LED array with and without a MOSFET driver



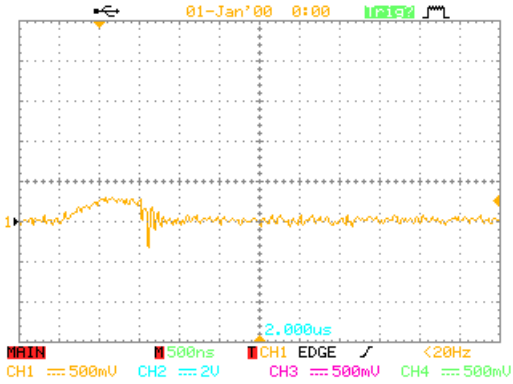
(a) 10v with 4427 driver



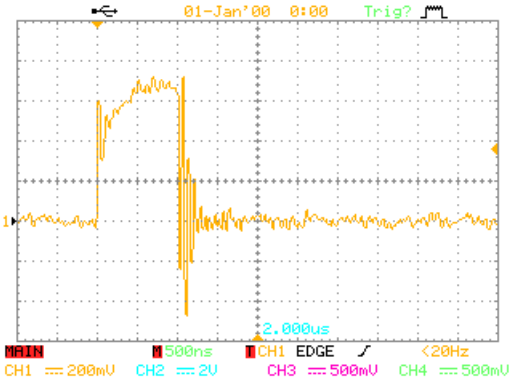
(b) 10v without 4427 driver



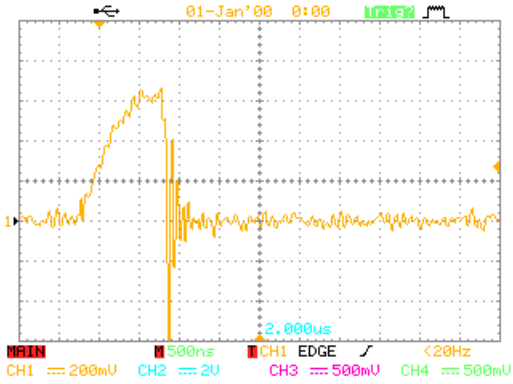
(c) 12.5v with 4427 driver



(d) 12.5v without 4427 driver



(e) 15v with 4427 driver



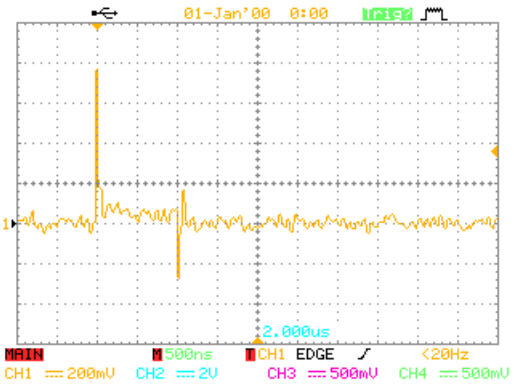
(f) 15v without 4427 driver

Figure 7.6: Current draw for the single Cree

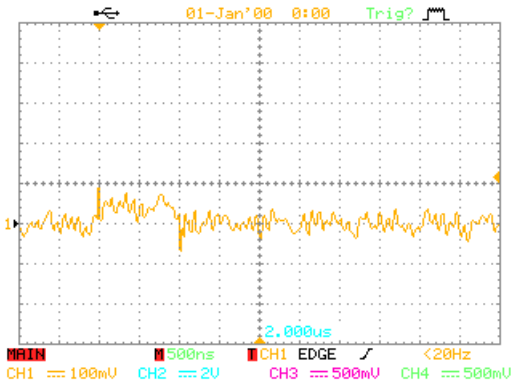
Figure 7.6 shows the current draw from the single Cree MC-E of LED for 3 different voltages. The oscilloscope monitor is connected to point C for channel 1 with the shield grounded at E.

Supply Voltage [volts]	Without 4427 [amps]	With 4427 [amps]	Percentage Gain [%]
10.0	0	0	0
12.5	0.25	0.35	40.0
15.0	0.60	0.70	16.7

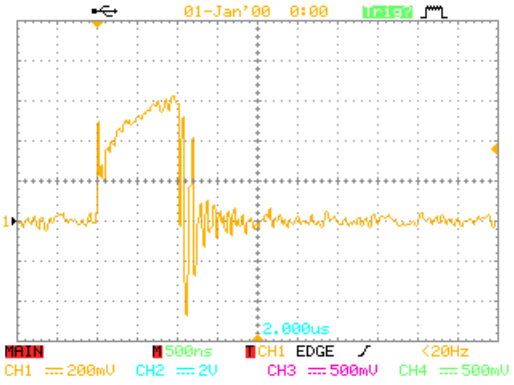
Table 7.2: Table comparing the amperage drawn by the single Cree MC-E LED with and without a MOSFET driver



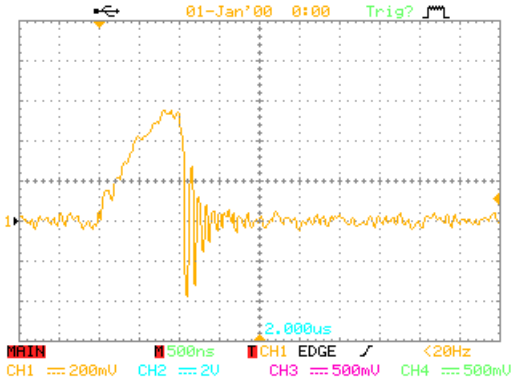
(a) 10v with 4427 driver



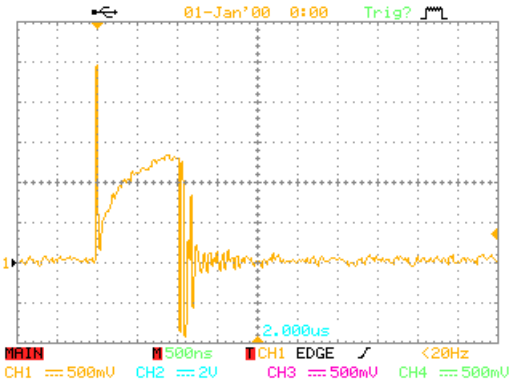
(b) 10v without 4427 driver



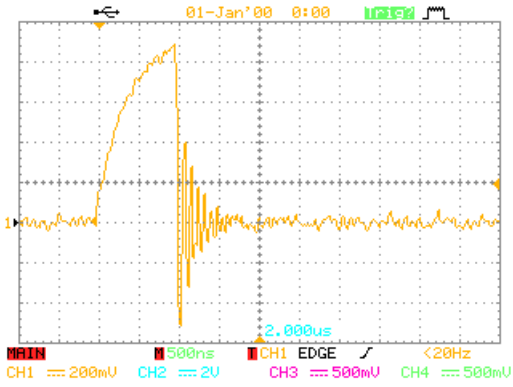
(c) 12.5v with 4427 driver



(d) 12.5v without 4427 driver



(e) 15v with 4427 driver



(f) 15v without 4427 driver

Figure 7.7: Current draw for the Cree array

Figure 7.7 shows the current draw from the Cree MC-E array of LED for 3 different voltages. The oscilloscope monitor is connected to point C for channel 1 with the shield grounded at E.

Supply Voltage [volts]	Without 4427 [amps]	With 4427 [amps]	Percentage Gain [%]
10.0	0.05	0.05	0
12.5	0.50	0.60	20.0
15.0	0.90	1.25	38.9

Table 7.3: Table comparing the amperage drawn by the Cree MC-E LED array with and without a MOSFET driver

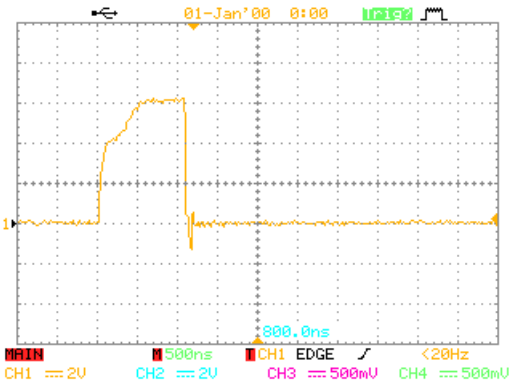
Referring to the results presented in tables 7.1, 7.2 and 7.3as well as figures 7.5, 7.6 and 7.7, it is quite apparent that the inclusion of the 4427 IC MOSFET driver has a profound effect on the current draw of the LED's.

The illumination profiles ,due to the inclusion of the 4427 IC, result in the various LED's turning on quicker and drawing a higher current than they would without the 4427. It is perhaps not as apparent with the lower current drawing 9x9 LED array, but the illumination profile becomes more square for the higher power Cree LED's. This phenomenon is particularly visible in figure 7.7c and 7.7d. The inclusion of the 4427 causes the voltage, and thus current draw, to increase much more rapidly into and through the LED. Thus the luminous output of the LED will increase.

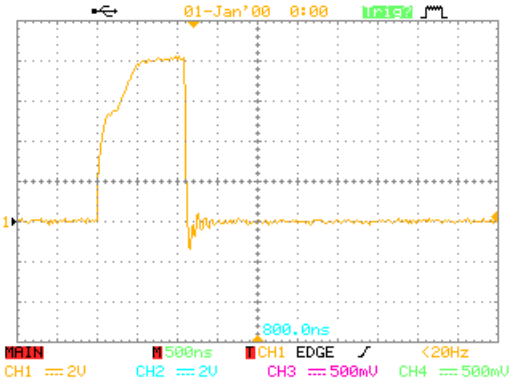
A similar effect is visible in figure 7.5c and 7.5d, however, the overall shape of the illumination profile is much the same. There is an initial peak showing a greater current draw at the moment power is applied to the LED.

Current draw by all of the LED's way surpasses the recommended maximum current stated by the manufacturers. Typically, the 5mm white LED's draw a current of around $20mA$ each at 3.2 volts. The 9x9 LED array is now drawing up to 3.5 amps at a low voltage of 15v. The LED's are arranged in parallel and thus the voltage drop over the LED's remains constant while the current draw increases. This infers that the current passing through a single LED is in the region of 390ma, approximately 20 times the stated maximum amperage.

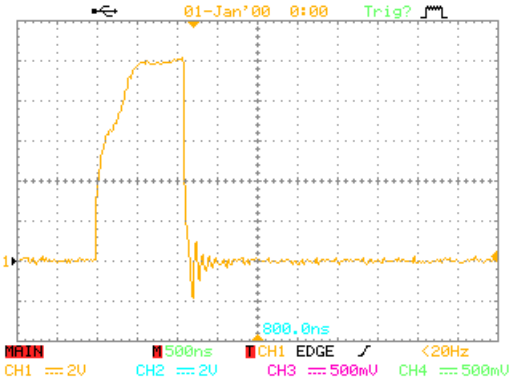
The typical forward voltage drop for the Cree MC-E LED's is 11.9v and thus at a supply voltage of 10v, the current will be very little due to the exponential relationship between voltage and current. This is apparent in figures 7.6 and 7.7. A current draw of $350mA$ is expected at 12v according to manufacturers specifications and this is the result which was obtained for the single diode.



(a) 10v



(b) 12.5v



(c) 15v

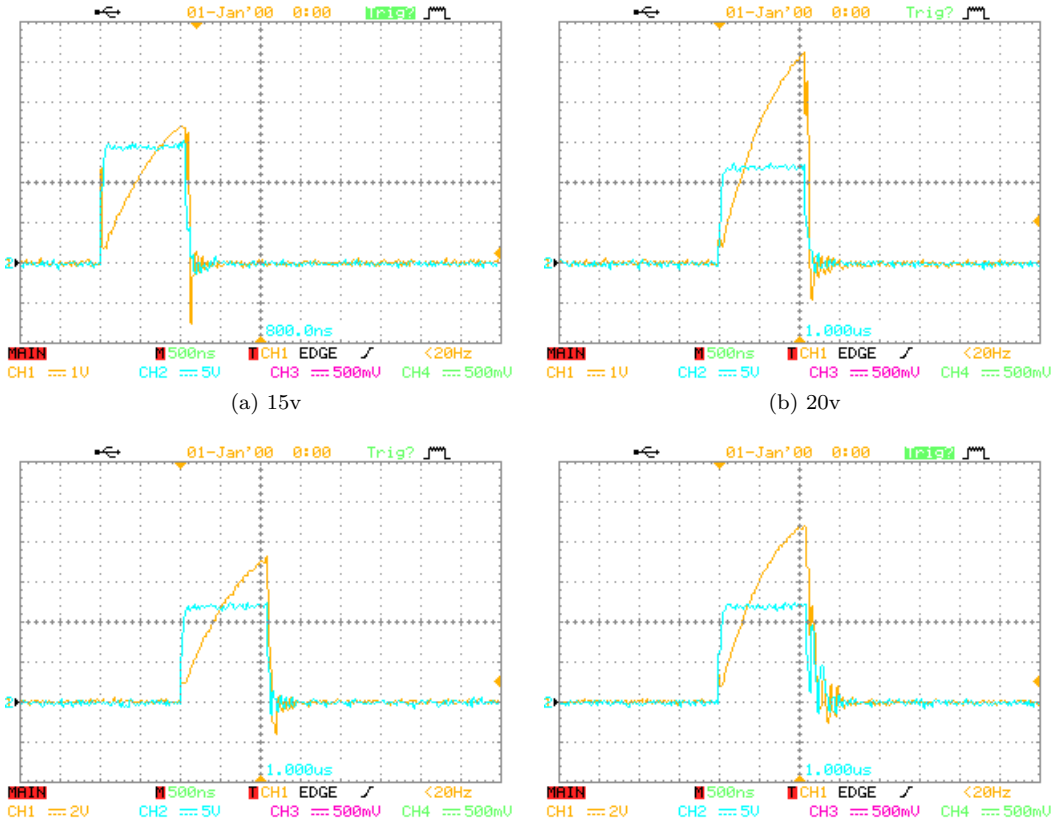
Figure 7.8: Short circuit MOSFET current for three supply voltages

Figure 7.8 shows the current passed by the MOSFET through a 1ohm resistor for three supply voltages. The oscilloscope monitor is connected to point C for channel 1 with the shield grounded at E. The LED has been short circuited to generate these results.

Supply Voltage [volts]	Amperage [amps]
10	6
12.5	8
15	10

Table 7.4: Table illustrating the amperage which may be passed by the MOSFET during short circuit at low voltages

Referring to figure 7.8 and table 7.4 it is clear that the circuit as a whole has the capacity to allow up to 10 amps of current to flow through the MOSFET for voltages up to 15 volts. Interestingly, the MOSFET seems to take in the region of $500ns$ to fully turn on regardless of the supply voltage. The rising edge has a step which seems to occur two thirds of the way up the maximum current spike. This may perhaps be due to internal circuitry of the MOSFET as the signal supplying the MOSFET is very square-like and most likely not the issue. If a similar phenomenon occurs with the LEDs attached, this may be the reason for any delays in the LEDs illumination. After $500ns$ of the pulse, the current flow through the MOSFET is stable and the falling edge is free from noise and any significant jitter.



(a) 15v (b) 20v

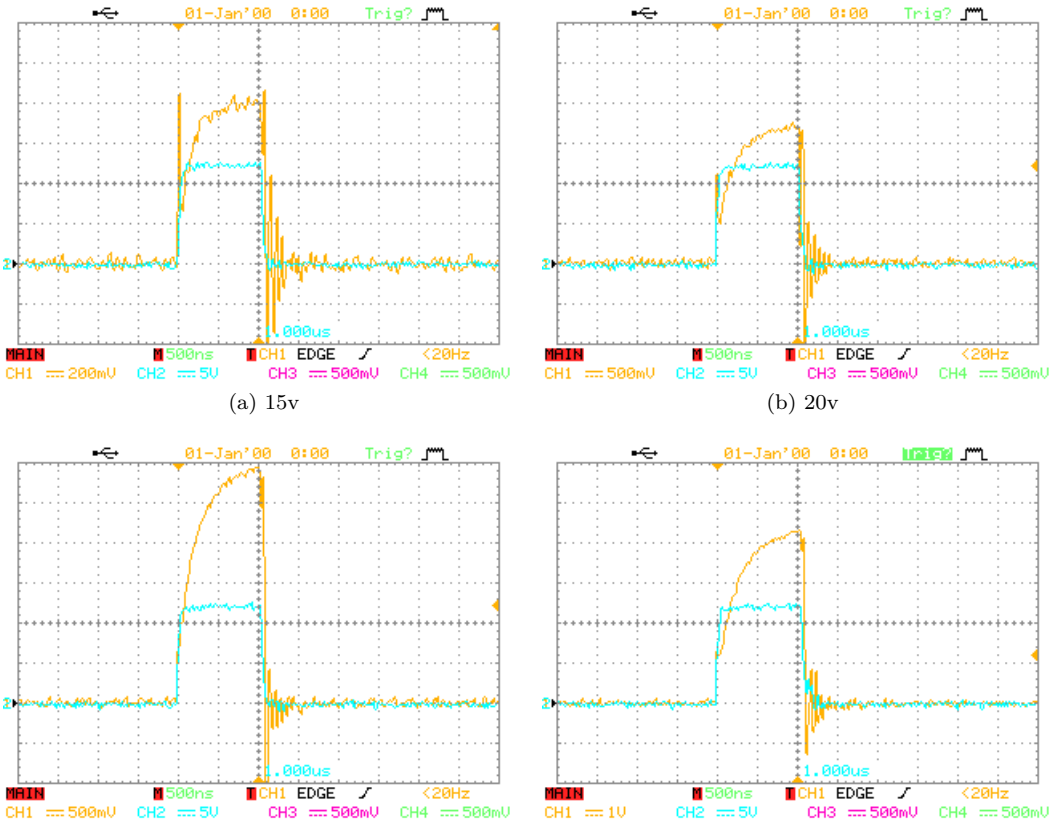
(c) 25v (d) 30v

Figure 7.9: MOSFET supply voltage and 9x9 LED array current for four high voltages

Figure 7.9 illustrates the MOSFET input voltage waveform (CH2, point B) and the current drawn by the 9x9 LED array (CH1, point C)

Supply Voltage [volts]	Current Drawn [amps]
15	3.5
20	5.2
25	7.1
30	9.0

Table 7.5: Table of current drawn by the 9x9 LED array for high voltages



(a) 15v (b) 20v

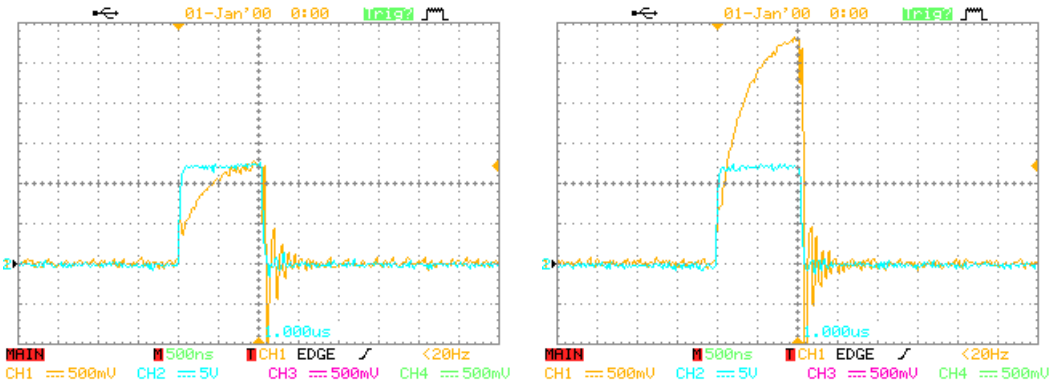
(c) 25v (d) 30v

Figure 7.10: MOSFET supply voltage and single Cree MC-E LED current for four high voltages

Figure 7.10 illustrates the MOSFET input voltage waveform (CH2, point B) and the current drawn by the single Cree (CH1, point C)

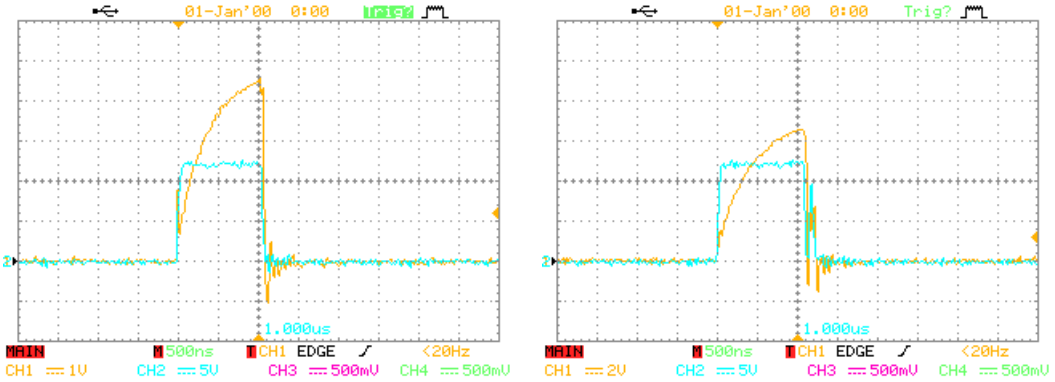
Supply Voltage [volts]	Current Drawn [amps]
15	0.80
20	1.75
25	2.90
30	4.20

Table 7.6: Table of current drawn by the Cree MC-E LED array for high voltages



(a) 15v

(b) 20v



(c) 25v

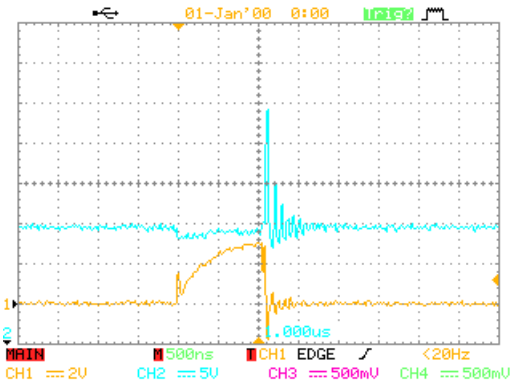
(d) 30v

Figure 7.11: MOSFET supply voltage and Cree MC-E LED array current for four high voltages

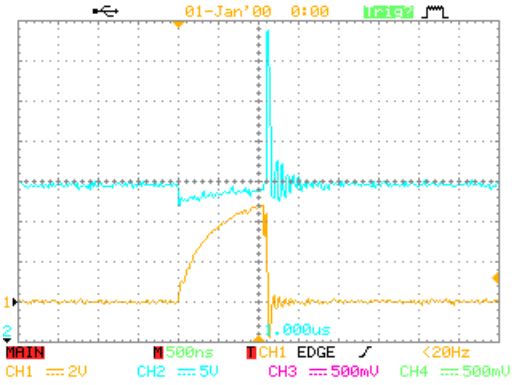
Figure 7.11 illustrates the MOSFET input voltage waveform (CH2, point B) and the current drawn by the 3 Cree LED array (CH1, point C)

Supply Voltage [volts]	Current Drawn [amps]
15	1.25
20	2.75
25	4.50
30	6.50

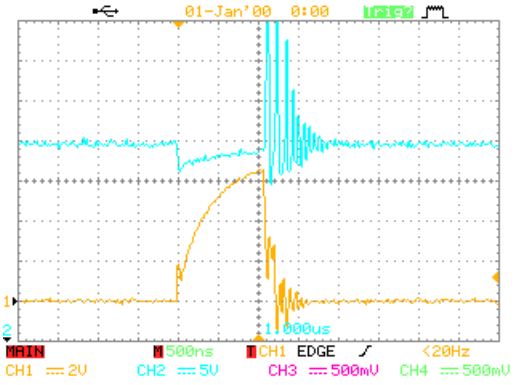
Table 7.7: Table of current drawn by the Cree MC-E LED array for high voltages



(a) 20v



(b) 25v



(c) 30v

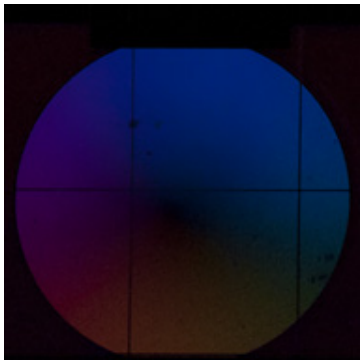
Figure 7.12: Source voltage fluctuation with the Cree MC-E LED array at three high voltages

Figure 7.12 shows the source voltage fluctuations with a large current drawing LED array at higher voltages. The oscilloscope monitor is connected to point C for channel 1 and D for channel 2 with the shield grounded at E.

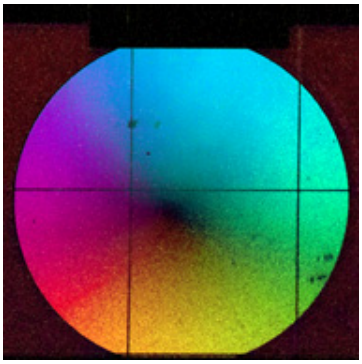
7.1.2 Observations

A number of observations were made during the testing of the LED circuit and the most pertinent are itemized below:

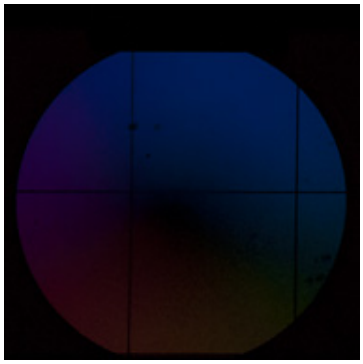
- During extended constant constant operation modes, the higher powered LED's do start getting hot and thus adequate heat dissipation systems were used to keep the LED's running at optimum temperature.
- The circuit triggering system worked flawlessly with the Seitz computerized shock tube. The LM74121 accepted the TTL signal output and triggered the LED on the falling edge input signal.
- The Seoul P7 LED was found to be very susceptible to EOS in the form of ESD. Two of these LED's failed during preliminary circuit testing with no visible damage to the internal diodes. No adjustments were made to the circuitry between testing other LED combinations and the Seoul LED's and so it was assumed the LED's were not compatible with this type of pulsed operation. For this reason, no data or electrical response was found for their performance with the circuits mentioned herein.
- The visual spectral output varies depending on the LED being tested as well as the source voltage supplied to the LED. This is known as spectral or chromaticity shifting and results in a different colour being emitted from the LED when it is significantly overdriven. The measurement of this shift is beyond the scope of this dissertation, however the effects may be visually observed when operating this pulsing circuit at higher voltages. The problem of spectral shifting in a colour schlieren system which relies on colour as a quantitative measure is detrimental to the efficacy of the system.
- As is expected with higher source voltages, any power dissipation in the circuit is increased and thus the voltage regulators are required to dissipate more energy to keep their relative outputs constant. Heat sinks and adequate airflow are required to keep the power transistors cool and in their operating ranges.
- There was concern that perhaps the 1Ω current monitoring resistor was limiting the current flow through the LED's and as such it was removed for a visual inspection of the brightness of the LED pulses. No difference was noticed in the brightness of any of the LED's. This method is not ideal as the LED's are being significantly overdriven and as such if there is a fault with the circuitry which causes the LED's to remain on, they may burn out almost instantly. There is also no way to measure the current passing through the LED's in this case.



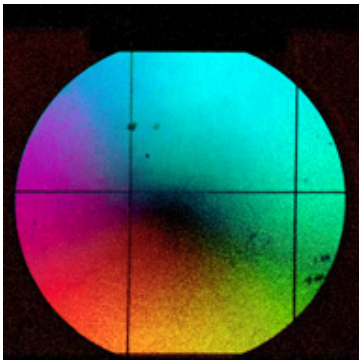
(a) ISO3200 RAW



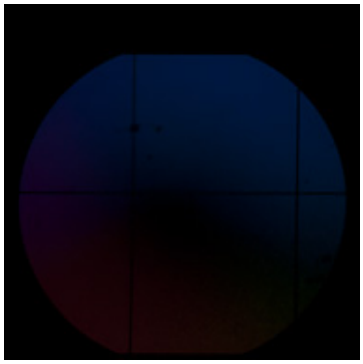
(b) ISO3200 Edited



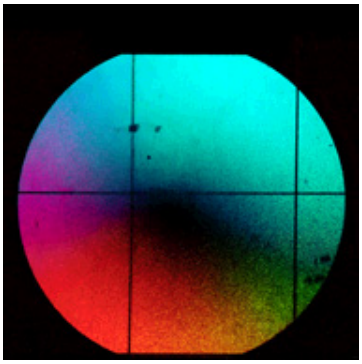
(c) ISO2000 RAW



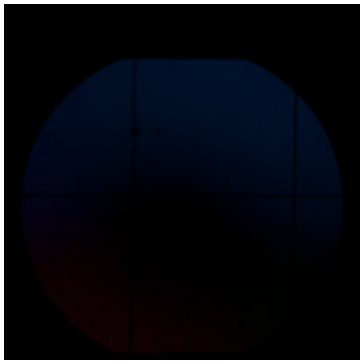
(d) ISO2000 Edited



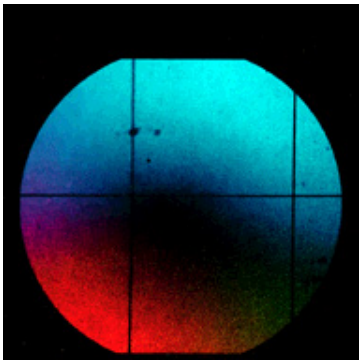
(e) ISO1250 RAW



(f) ISO1250 Edited



(g) ISO800 RAW



(h) ISO800 Edited

Figure 7.13: Images of the calibration lens placed within the test section at various ISO settings

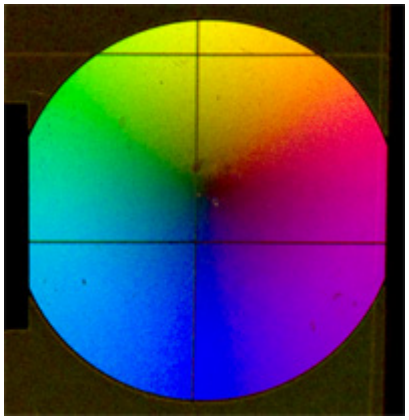
The above figure illustrates the performance of a single Cree MC-E LED operating with a $10\mu s$ pulse width, triggered using the Seitz system. The images on the left are unedited whilst the images on the right are the corresponding edited photos for a given ISO setting.

7.2 Data processing & analysis

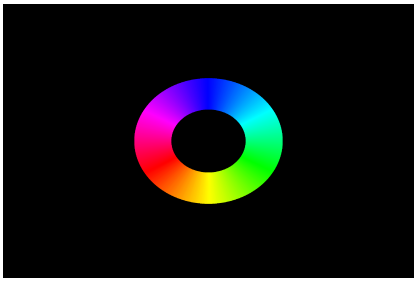
Computation, analysis and preparation of the data is undertaken by software and presented in this section.

7.2.1 Source mask analysis

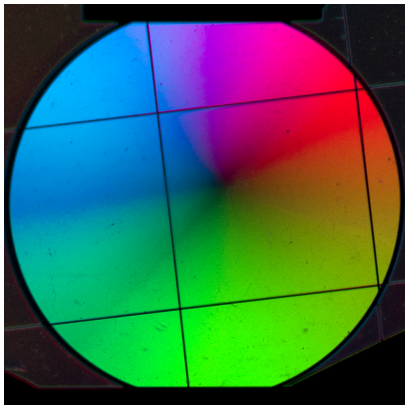
The source masks used in this colour schlieren system are one of the most critical components as they are the components which impart directionality information into the light passing through the test section. For this reason, the colour reproductions must be high quality. Unfortunately, the production process introduces fluctuations in the design in terms of colour reproduction, print quality and source mask dimension ratios. The images of the calibration lens shown herein were captured using the Cree LED powered light source operating in constant 'ON' mode. This light source was used to examine the spectrum of produced colours as well as to prove its potential in this schlieren application.



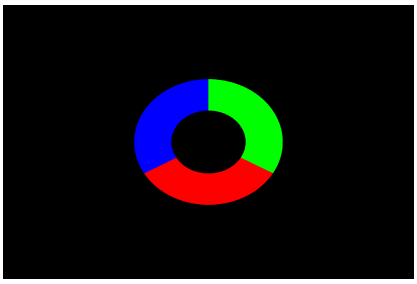
(a) Calibration lens - Source mask A



(b) Source mask A



(c) Calibration lens - Source mask B



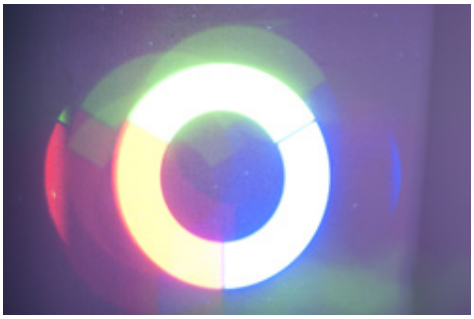
(d) Source mask B

Figure 7.14: Source mask comparison

The results, illustrated in figure 7.14, compare the two most viable source mask designs. Ignoring the direction indication of the source masks and simply analyzing the quality of the colour reproduction is is quite evident that source mask A yields improved results over source mask B. The colour blending using source mask A is more gradual and fewer bands of colour are exhibited. For this reason, based purely on a visual examination of the images, source mask A is the preferable option for this schlieren setup. All images captured utilized source mask A unless otherwise stated or illustrated.



(a) Normally exposed image

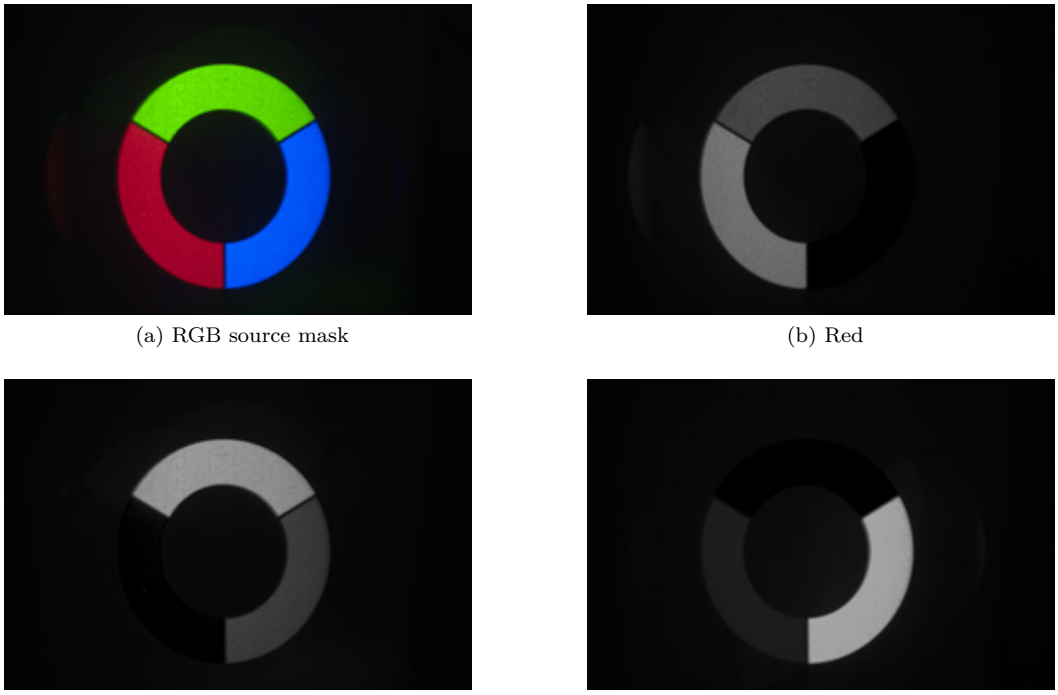


(b) Over exposed image illustrating internal system reflections

Figure 7.15: Source mask in cut-off plane

The most efficient way to determine the quality of the source masks is to place the imaging sensor in the cut-off plane. This results in images captured such as those shown in figure 7.15. Figure 7.15a illustrates a digital replica of the original source mask once the light has passed through the entire system except for the iris diaphragm. This method thus provides a good indication of the quality of the source masks, the interference from the optical system, the correction of the cylindrical lens for astigmatism and the colour combinations which are captured by the imaging sensor. This source mask design was not used for any of the captured schlieren images but rather for experimental purposes discussed in this subsection.

Figure 7.15b is an over exposure of image A and shows the internal reflections within the optical system. This is in part due to the slight misalignment of the various optical components as well as internal refractions and reflections. There are multiple 'duplicates' of the main source mask image scattered around the image and it is these duplicates which will cause problems in terms of quantitative studies.



(a) RGB source mask

(b) Red

(c) Green

(d) Blue

Figure 7.16: Source mask in cut-off plane illustrating RGB response

Dissecting the source mask and splitting it into its three colour components we arrive with the results displayed in figure 7.16. Each monochromatic colour channel has been extracted and displayed individually, illustrating the problem of light of different wavelengths 'leaking' through the source mask filter.

	Red Third	Green Third	Blue Third	Average Black
Red Component	165 (65%)	95 (37%)	0 (0%)	8 (3%)
Green Component	4 (2%)	205 (80%)	80 (31)%	8 (3%)
Blue Component	42 (16%)	1 (0%)	245 (96%)	8 (3%)

Table 7.8: Table containing pixel values for each channel for each segment of the source mask

This 'leaked' light essentially contaminates these channels and results in the full range of colour hue's not being being produced. Table 7.8 provides a numerical reference to this problem. The values have a possible maximum of 255 and the percentages indicate the extent of the contamination. This further results in the full range of density gradient directions and magnitudes not being efficiently represented. The blue third is the most accurate region as it contains the least contaminated light from other channels whilst maintaining a high response rate. The red region contains on average, a blue intensity of 16% of the available intensity with little green.

The calibration lens and the method used to quantify the experimental images will inherently take into account this channel contamination but will result in fewer possible hues and intensities in the final schlieren image.

7.2.2 Tecplot post-processing

The results contained in this section pertain to the post processing of the data files outputted by the CFD code. A number of time stepped CFD simulation images have been included to provide for an improved understanding of the flow characteristics. The CFD images have been chosen to most accurately coincide with some of the photographic images taken to allow for system performance validation.

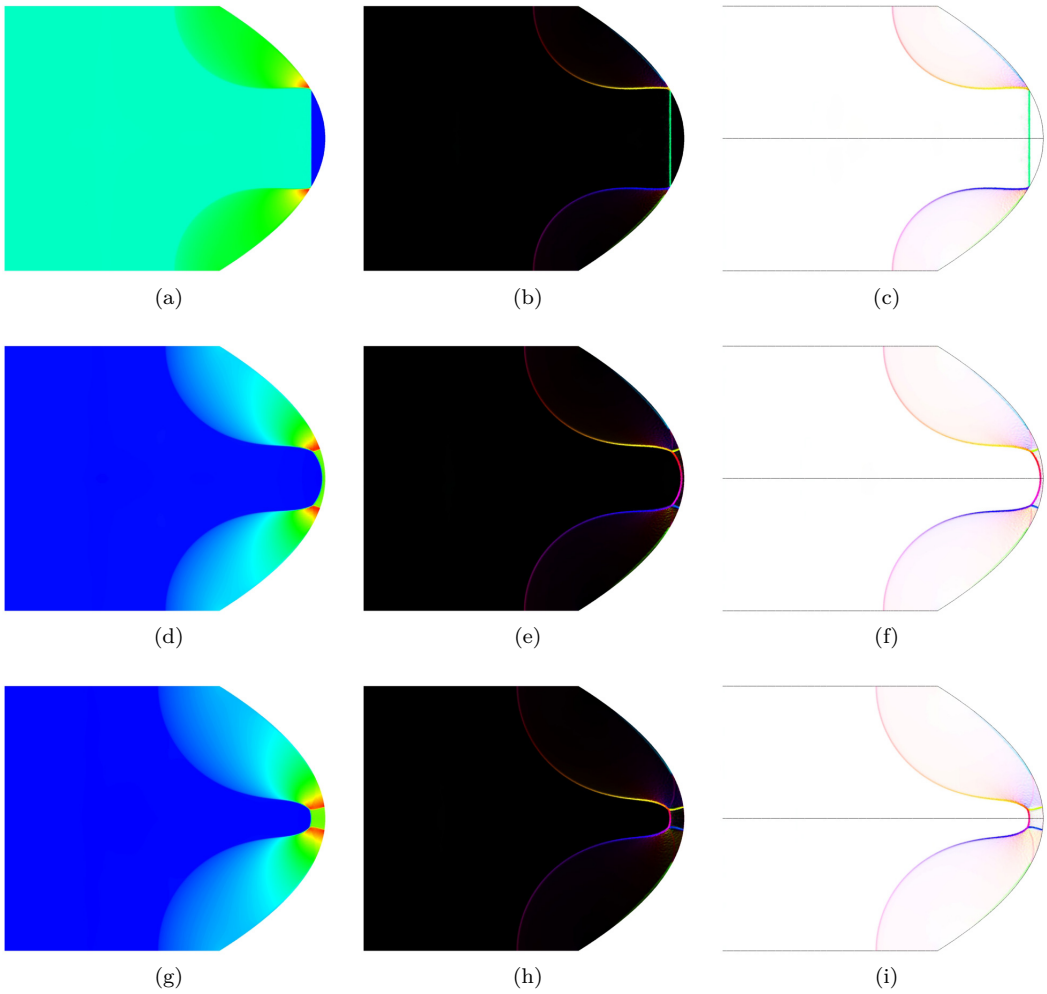


Figure 7.17: CFD simulation images with corresponding colour schlieren interpretations

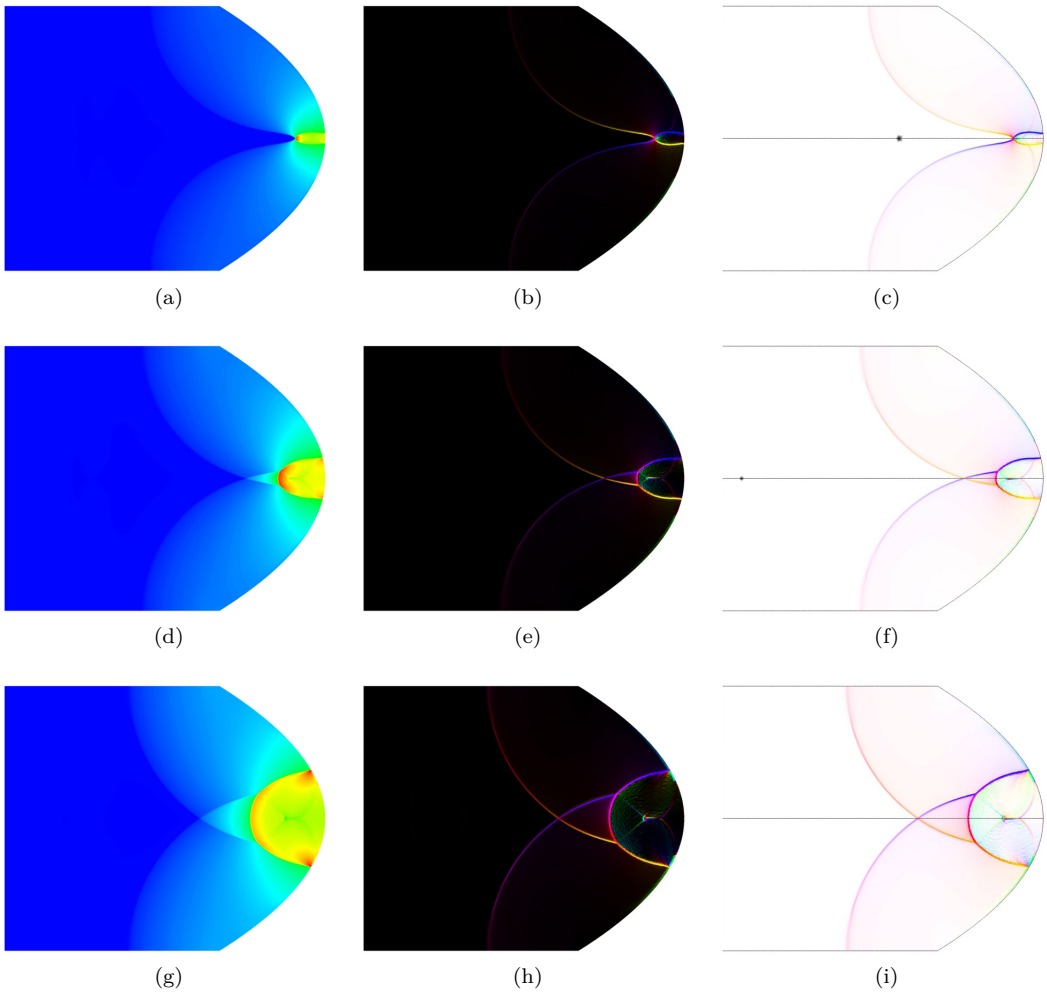
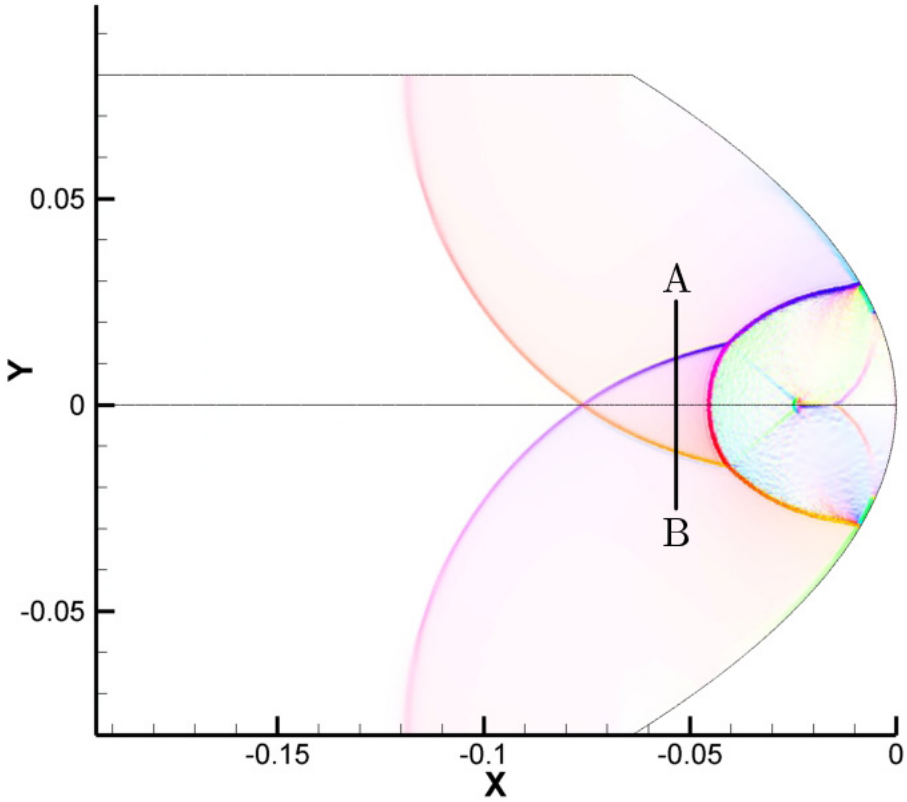


Figure 7.18: CFD simulation images with corresponding colour schlieren interpretations

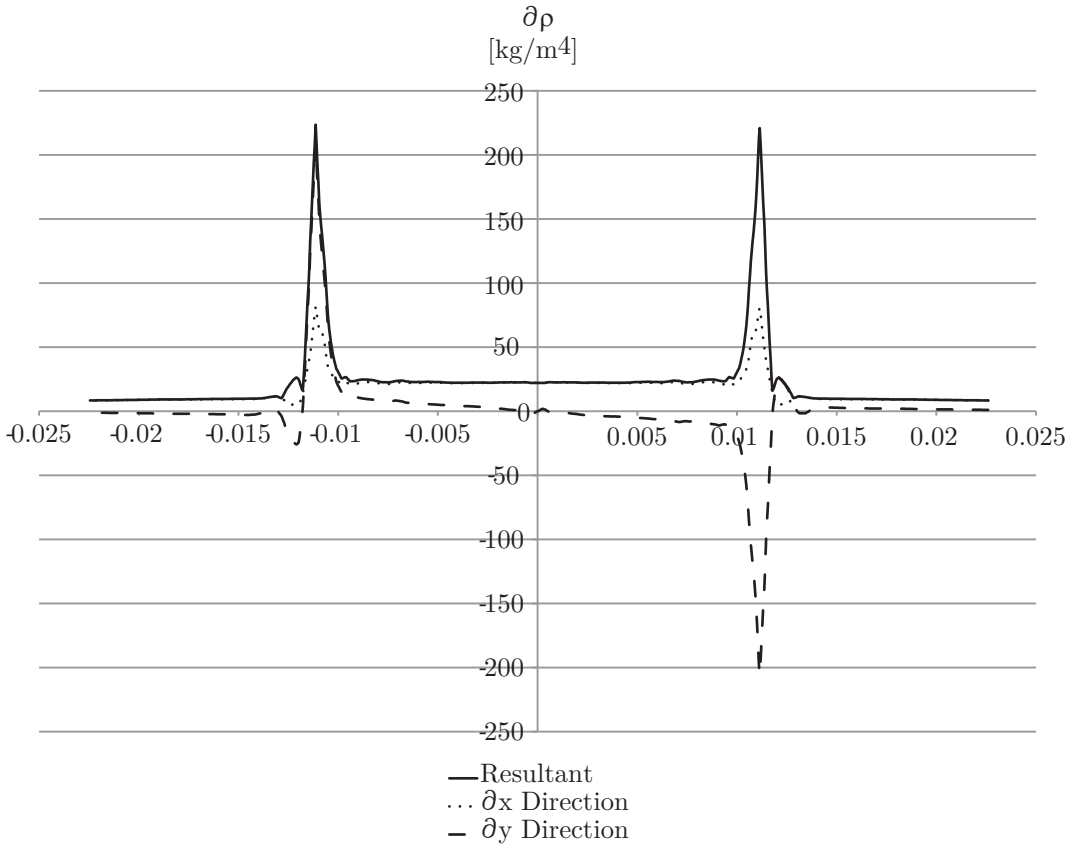
The CFD results generated by Lukes code, Tecplot and the colour schlieren script are presented in figures 7.17 and 7.18. The sub-images are time stepped in approximately $20\mu s$ intervals. The left most column represents the raw CFD data displaying density contours while the middle and right most columns illustrate the density gradient magnitudes in colour schlieren form with a black and white background respectively. The white background allows the colours, specifically in low density gradient magnitude regions, to be more easily inspected in comparison to the black background images.

Figure 7.17a has a slightly different contour map to those of the following time steps. This difference in colour is simply due to the fact that the shock wave has not yet reached its maximum distance and reflected off the parabolic model.

The colour reproductions and intensity with respect to density gradient direction and magnitude respectively are well defined and portrayed by the synthetic colour schlieren code. It is apparent that the code accounts qualitatively for the variation of the density gradient magnitude by means of altering the colour intensity. This is perhaps clearer with the black background images as colour details on black appear to have less contrast than on white.



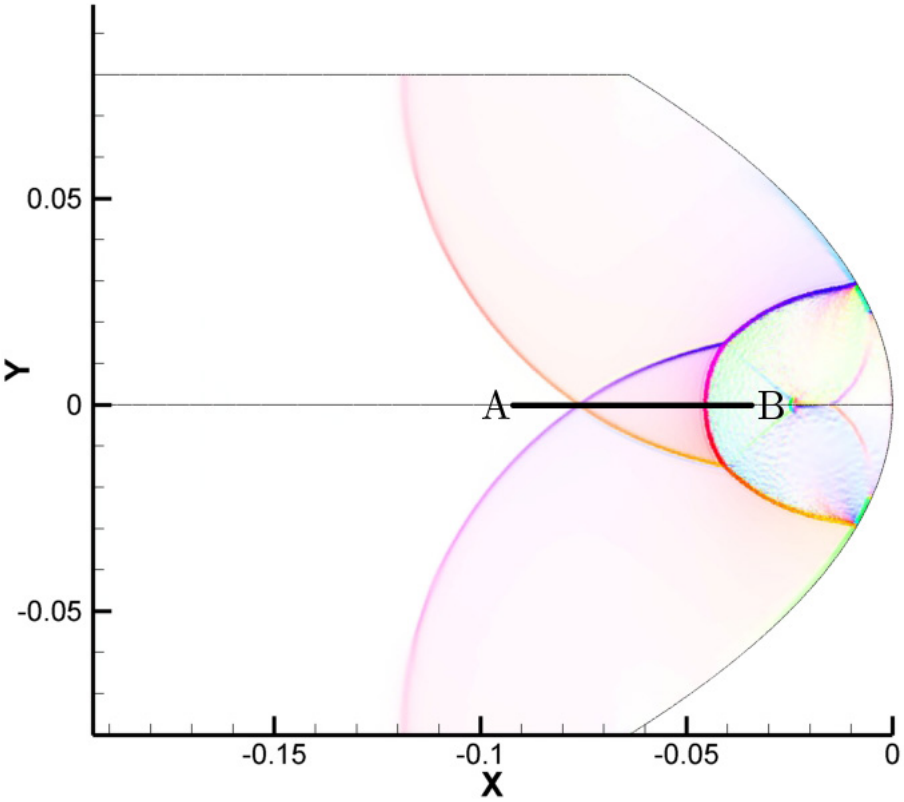
(a)



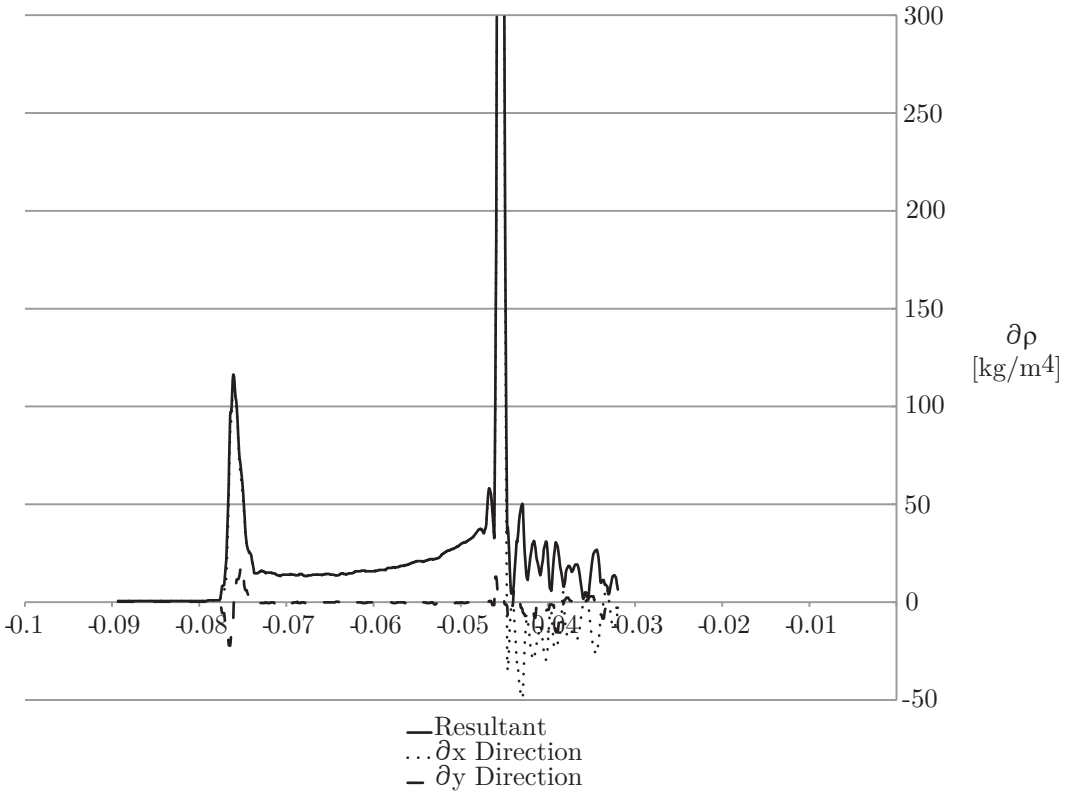
(b)

Figure 7.19: Vertical data

CFD data is readily extracted from the Tecplot images using the in-built functions to extract data to a file along user defined poly-lines. Figure 7.19 shows the data extracted along a vertical poly-line crossing two shock waves traveling in opposite directions. This region was chosen since the density gradient magnitudes over the shock waves would be in excess of what the calibration lens might be able to return and thus the limits of the lens would be examined. The region inside the main expansion 'bubble' containing the foci of the shock reflection contains a fair degree of noise and thus for lens comparison purposes, a region with as little noise as possible was chosen. The density gradients in front of the 'bubble' are relatively strong and seem to contain little noise which is ideal for a comparison to calibration lens data.



(a)



(b)

Figure 7.20: Horizontal data

Similarly, data was extracted along a horizontal line as in figure 7.20. Data was extracted along this line as the data set includes a relatively weak shock with density gradients which the lens should in theory be able to resolve. The data set also includes a significantly more powerful shock wave as well as noisy data within the shock reflection 'bubble'. The noisy data will give an indication of how the lens manages to resolve apparently fluctuating density gradient magnitudes according to the CFD results. Both figures contain plots of the extracted data and each vertical axis has been limited by the maximum density gradient magnitude which may be resolved by the calibration lens.

7.2.3 OpenCV

OpenCV is the software library based in C++ used to analyze the experimental images obtained. Upon loading the calibration lens image into the system and informing the software of the exact lens location and specification, the colour information is extracted, compared within the software and the results extracted and plotted. The light source used to capture shock reflections is the xenon flash lamp as the LED system was incapable of reaching the desired illumination pulse times. This resulted in degraded image quality and lower colour reproduction. The source mask used for all schlieren work in this subsection is shown in figure 4.2d.

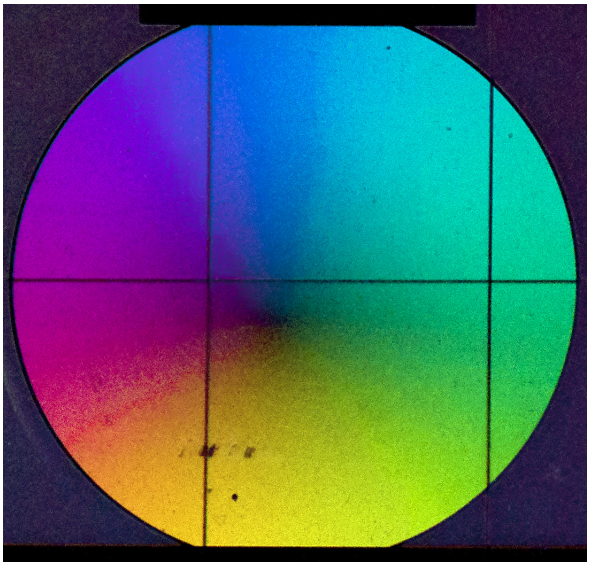


Figure 7.21: Calibration lens used for pixel analysis

The calibration image, shown in figure 7.21, exhibits a non-concentric dark spot of zero density gradient magnitude. The image has been leveled to achieve an optimum response and the experimental images were leveled by the same amounts in each channel. Positive density gradients in the Y and X directions were taken to be up and right respectively from the dark spot.

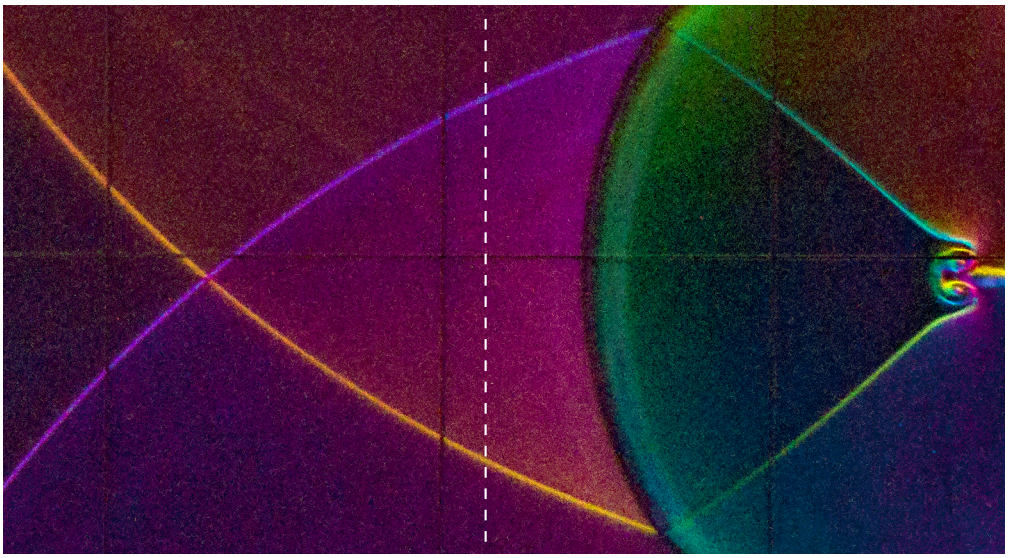


Figure 7.22: Experimental image, vertical data extraction

Data has been extracted along a straight line and shown in figure 7.22. The data was extracted approximately midway between the dashed line. Due to the RAW file formats, the images exhibit a fair degree of noise and this results in a more significant pixel value variation in comparison to JPEG file formats. The degree of noise present in the image is also a result of the low light intensity and inefficiency of the schlieren system.

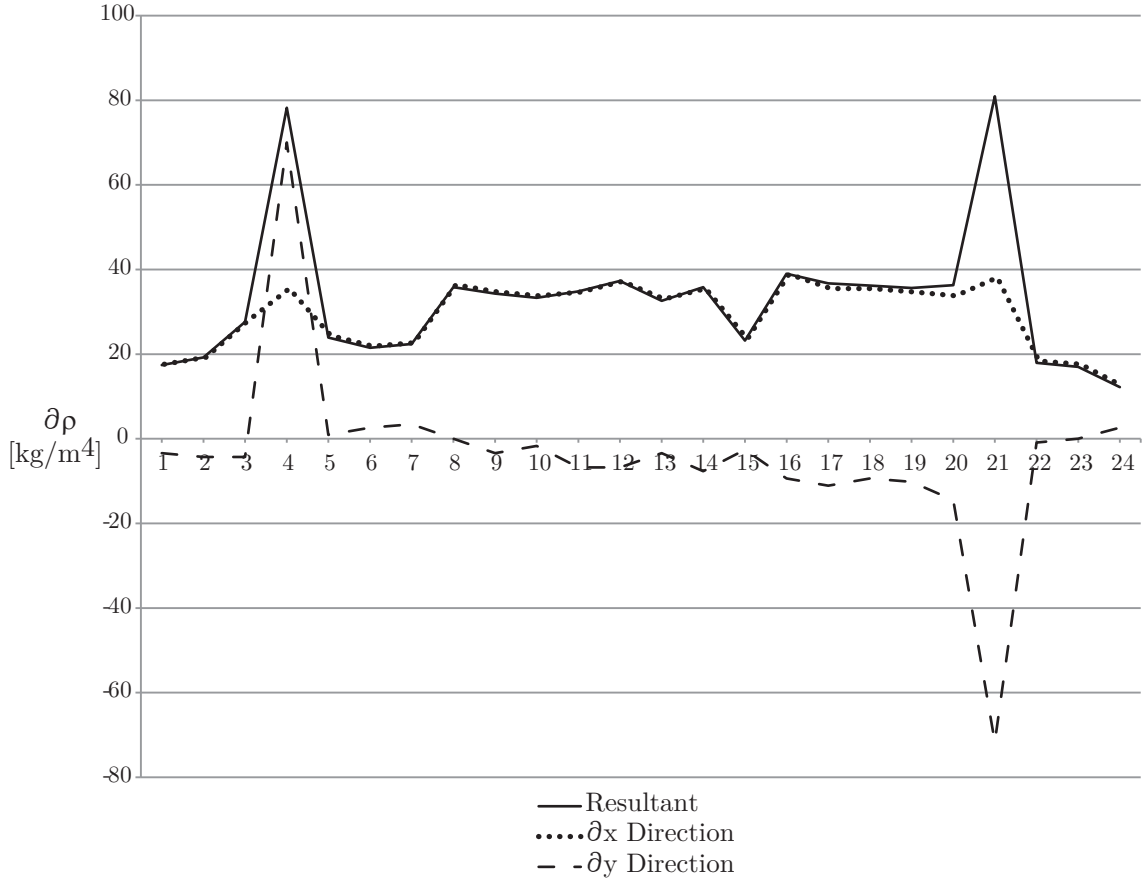


Figure 7.23: Plot of vertical data

Figure 7.23 is a plot the data extracted from figure 7.22. The plot contains the density gradients magnitudes in the X and Y directions as well as the resultant density gradient magnitude. As expected for a vertical data extraction, there is little variation in the Y direction except over the shock reflections and the density gradient magnitude is an approximately constant $30kg/m^4$ throughout the region between the two shock reflections. Positions 4 and 21 are the upper and lower shock positions respectively.

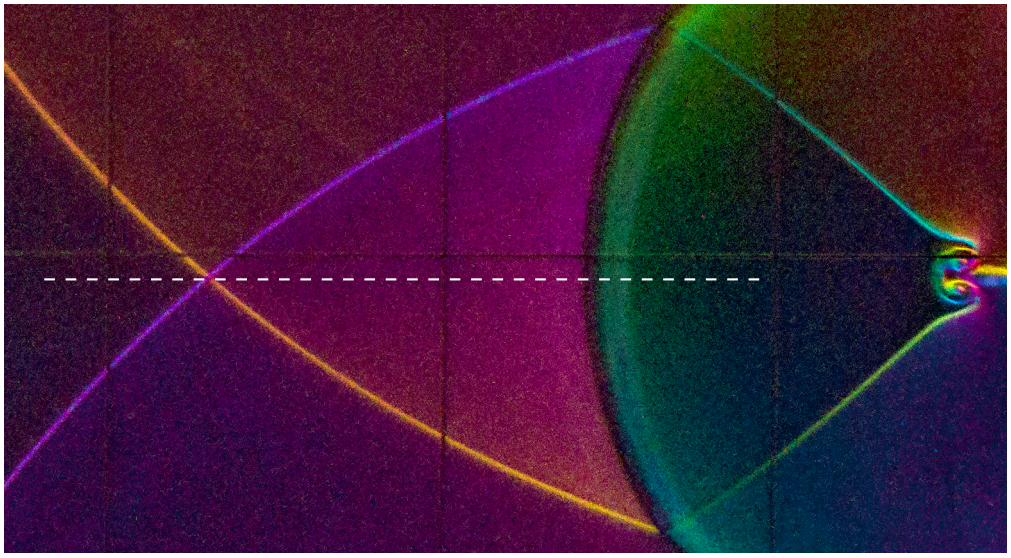


Figure 7.24: Experimental image, horizontal data extraction

A similar pixel evaluation is applied to the same image in a horizontal line. This is shown in figure 7.24. Again, the pixel values are extracted from between the dashed line sections and occasionally taking an average due to pixel variations.

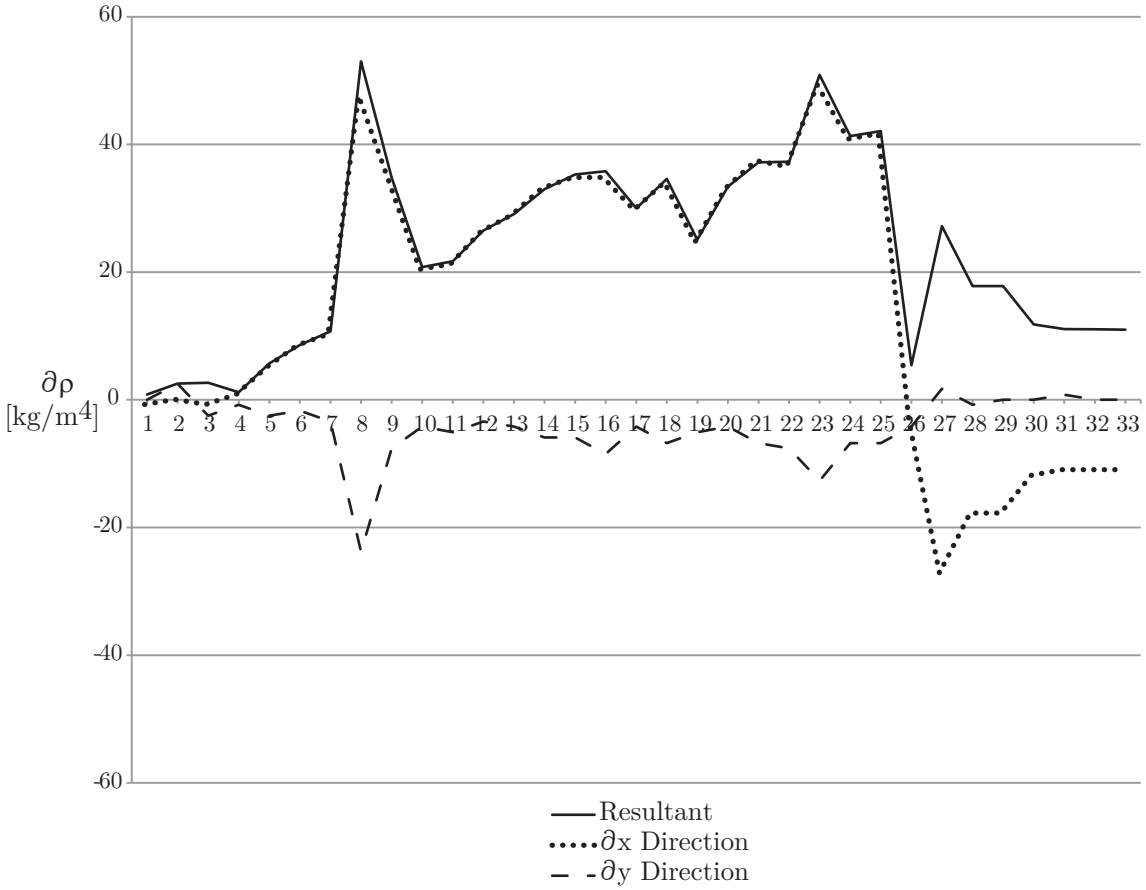


Figure 7.25: Plot of horizontal data

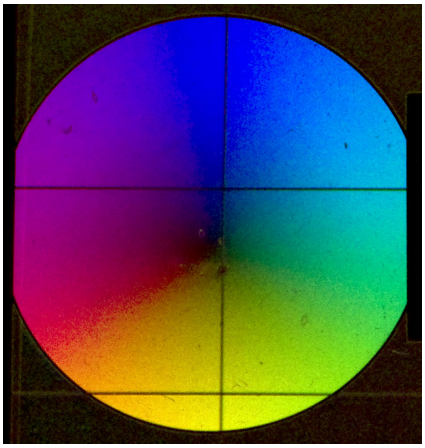
The results are plotted, figure 7.25, and again contain X and Y directions as well as the resultant density gradient magnitude. This data similarly shows little Y direction density gradient fluctuations along the length of the line with the X direction exhibiting most of the density gradient magnitude change. Positions 8 and 26 are the reflected shock intersections and the main reflected shock respectively. The density gradient magnitude is expected to rise from point 8 at the intersection of the weaker shock reflections up until the main reflected shock at position 26 and this is the overall trend in the extracted data.

In comparison to the CFD results, figures 7.19 and 7.20, the experimental data, figures 7.23 and 7.25, shows similar trends and values.

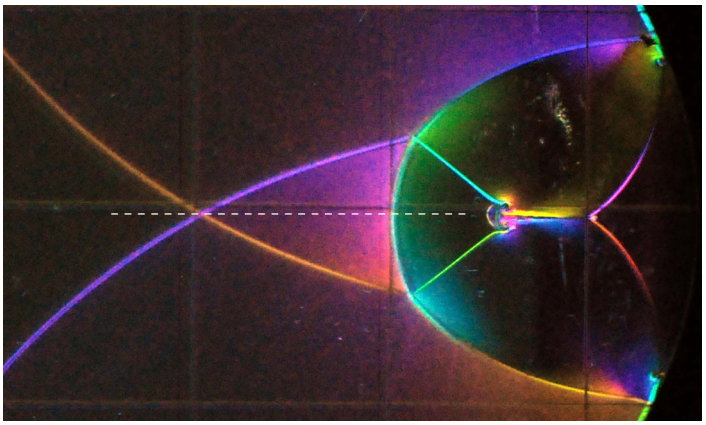
Examining the vertical case, the CFD density gradients in the X direction see fluctuations upon crossing over the shock wave reflections and tend to stabilize between them at approximately $22.1kg/m^4$. In relation to the experimental data, little to no fluctuations are present over the shock wave reflections however, there is a degree of correlation in the value of the recorded density gradient between the CFD and experimental results. The average density gradient recorded experimentally, between points 5 and 20, was $32.4kg/m^4$. Density gradients in the Y direction follow a common trend in both CFD and experimental images with the CFD results indicating a maximum in the region of $225kg/m^4$ over the shock reflections. Due to limitations by the calibration lens, the experimental results could potentially only yield a maximum of $155kg/m^4$. The experimental results show a maximum of $80kg/m^4$ over the shock waves and the reason the results are not exhibiting the full density gradient range may be due to lack of light passing through the system for this particular test or the iris diaphragm may have been stepped down too much in the attempt to improve sensitivity. Between the two peaks, there is a generally low density gradient magnitude which makes sense in light of the shock wave scenario. Similarly, the CFD results yield very low density gradients in this region. The resultant density gradient magnitudes in both directions have similar trends.

The horizontal case passes through the intersection of the reflected shock waves as well as the powerful main shock wave reflection. Again, examining the X density gradients in the CFD case, the density gradients reach large values over the two shock waves but significantly more so over the main reflected shock. The shock wave intersection returns a density gradient value of just over $110kg/m^4$ whilst over the main reflected shock it is essentially infinite as expected. The CFD data returns a large degree of noise within the main reflected shock bubble due to mesh and solver inconsistencies when the density data is derived. Examining figure 7.24 is it apparent that the colour saturation leading the main reflected shock is very low and this indicates a powerful refractive index as most of the light passing through these points are being bent out of the schlieren system and not recorded. The shock intersection results in a calibration lens value of $53kg/m^4$ being obtained. The magnitudes before the intersection are almost null with the magnitudes after the intersection slowly increasing up until the leading edge of the main reflected shock. After the main shock, within the shock bubble, the density gradients gradually decrease although to a higher level compared to before the shock intersection. Density gradients in the Y direction in both CFD and experimental images are in alignment however, there is marginally more response

in the experimental data in this direction. Both methods yield density gradient fluctuations within the shock regions of approximately $20kg/m^4$.



(a) Calibration image



(b) Experimental schlieren image

Figure 7.26: Improved quality images subjected to OpenCV analysis

Higher quality images, figure 7.26, were subjected to an analysis with OpenCV. These JPEG images contain less pixel noise than the RAW file formats and as such, the density changes are averaged slightly over the extents of the image. The optical system was adjusted in such a way so as to obtain even sensitivity in all directions as well as a uniform dark background. The dark background helps improve the contrast, highlighting small illumination changes in the imaging plane.

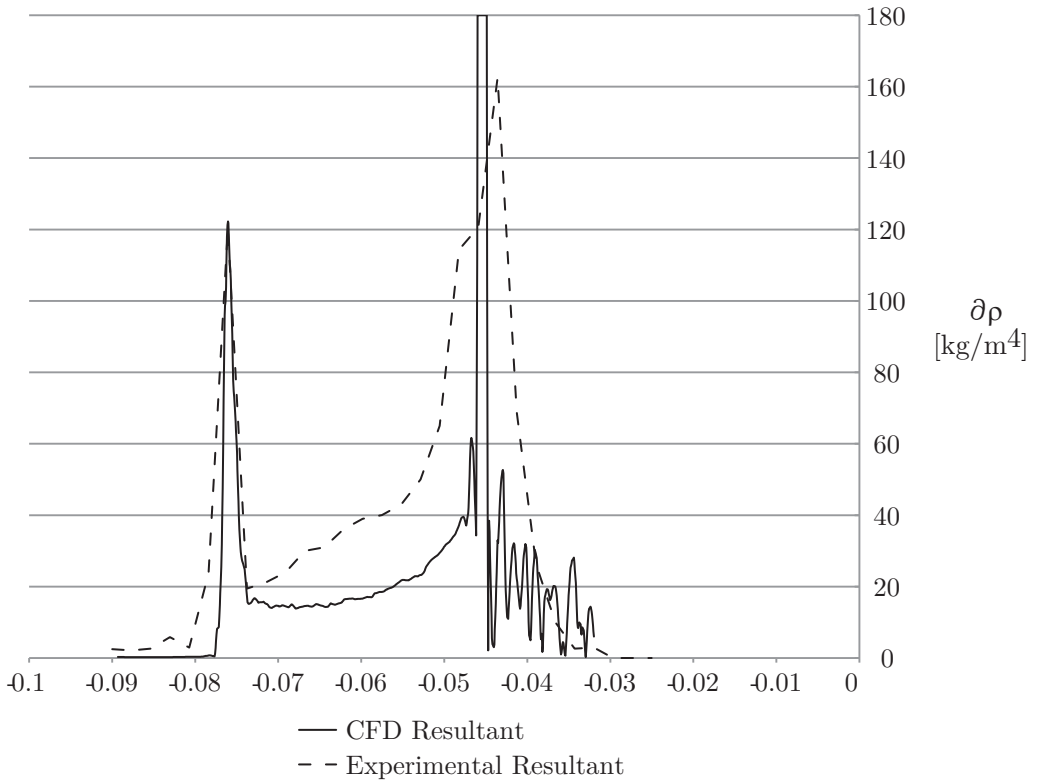


Figure 7.27: Plot of resultant density gradient magnitude for CFD and experimental results

Extracting the pixel values and comparing hues against the calibration image, the resulting density gradients are extracted from the OpenCV program and are shown in figure 7.27. As in the previous horizontal density gradient analysis, the region within the main shock bubble exhibits high oscillatory CFD noise. The intersection of the two reflected shock waves yields an experimental resultant density gradient magnitude of approximately $120 kg/m^4$ while the large bow shock magnitude is significantly higher and undetermined by the calibration lens method.

There is a gradual increase in density gradient between the two shock peaks as indicated by the CFD results. The experimental results exhibit this trend, however, the magnitude is reported to be much greater than the predictions of the CFD results. This may be partly due to the duration of the light source pulse. When the light is passing through the test section, a cumulative average of the flow characteristics are being recorded. This would result in an increased light intensity being recorded and thus the software will return larger density gradient magnitudes.

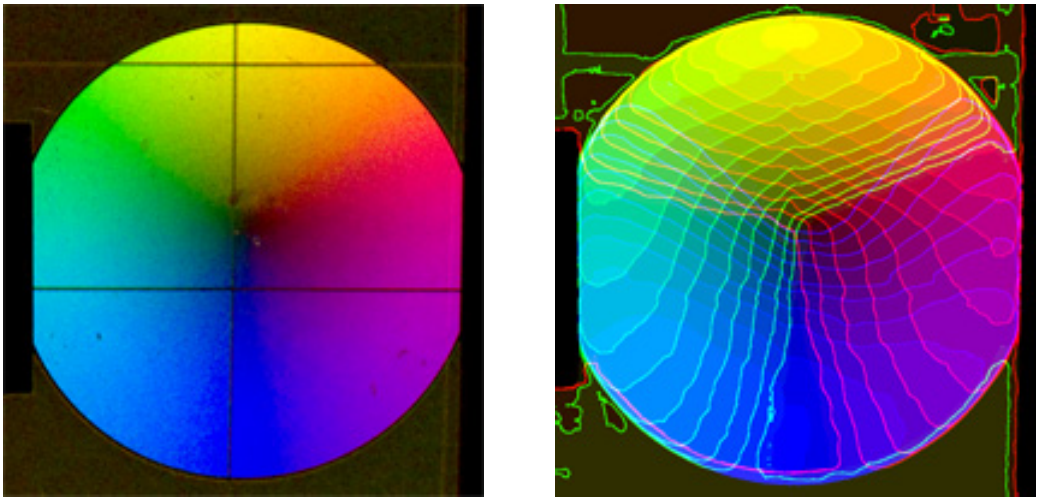
7.3 Schlieren system

The results pertaining to the physical schlieren system are presented here and include many of the images captured as well as particular methods of system and optics analysis.

7.3.1 Optical response

The optical response of the schlieren system is important, not only to ascertain the efficacy of the quantitative potential but also to improve the qualitative visual results. This schlieren system relies heavily on colour reproduction and thus the quality of the source masks as well as the optical system is crucial to obtain a high quality experimental image. The light source used for the images presented in this section is the Cree high power LED in constant 'ON' mode.

A high definition video clip has been included in Appendix B. The video clip shows the test section with the calibration lens in place and a butane powered soldering iron at various positions showing the response of the optical system. The light source in this video clip is a high powered Cree MCE which results in great colour depth and contrast.



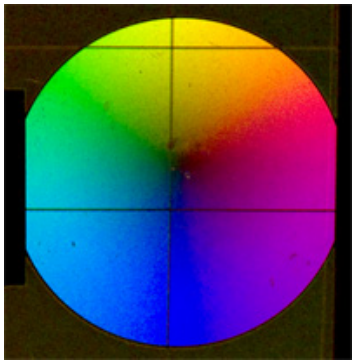
(a) Calibration lens (b) Calibration posterization

Figure 7.28: Calibration lens and corresponding posterization

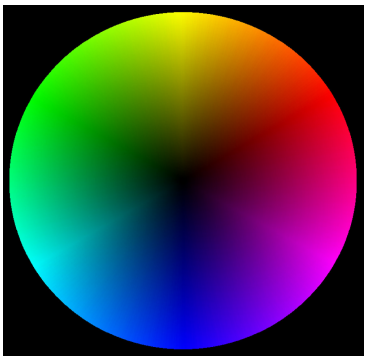
With the schlieren system setup as accurately as possible, the calibration lens was placed into the test section and the doors securely fastened. A number of images were captured by finely adjusting the iris diaphragm aperture as well as the position of the aperture to obtain figure 7.28a. This image of the calibration lens has been cropped to include only the lens and the levels of the image have been enhanced. The process of thresholding or posterization have been applied to this image which results in figure 7.28b being produced. Thresholding reduced the number of available colours a pixel may be, to a specified number. This essentially forces the pixels to 'jump' to the closest matching pixel value and what results are these contour-like lines outlining the regions with constant hue and intensity.

This technique gives an idea of the resolution capacity of the system. The resolution is not linear and varies with the intensity of the density gradient present in the test section as well as with the density gradient direction. This is examined in greater detail later in this section.

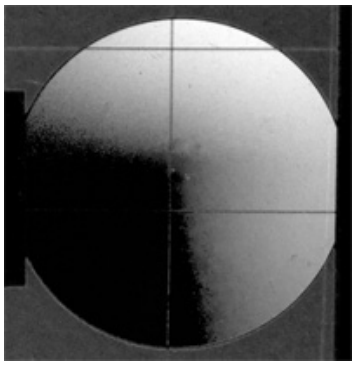
This application of thresholding allows the response of the calibration lens to the light passing through it, to be observed qualitatively. The response of the lens to increasing density gradient magnitudes in each direction with increasing lens radius may be seen. It is also pertinent to note that the combinations of each colour channel at each point around the lens area can be determined.



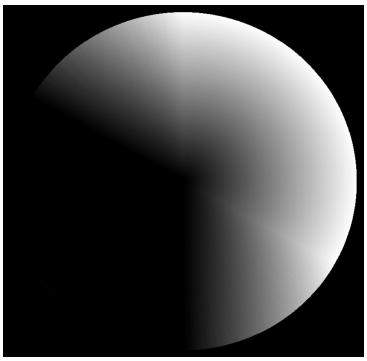
(a) Experimental RGB



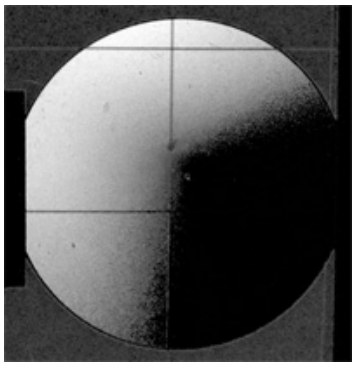
(b) Theory RGB



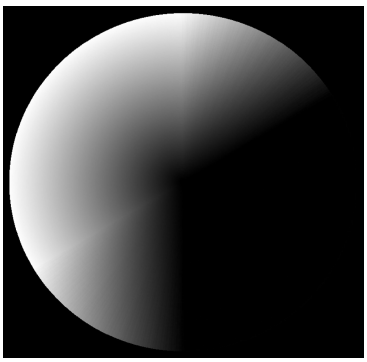
(c) Experimental Red



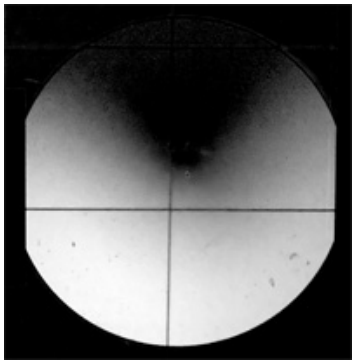
(d) Theory Red



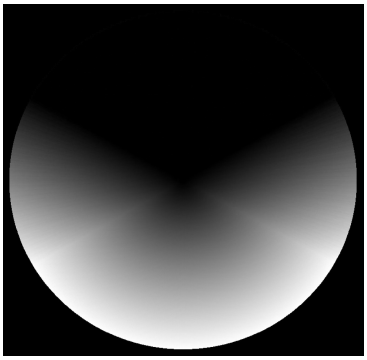
(e) Experimental Green



(f) Theory Green



(g) Experimental Blue



(h) Theory Blue

Figure 7.29: Calibration lens image decompiled into monochromatic RGB components

Before the calibration lens may be used to quantitatively analyze experimental images, the lens must itself be subjected to an analysis. Figure 7.29 illustrates the splitting of good quality experimental and theoretical images into their three monochromatic channels namely red, green and blue.

The procedure of splitting the images into their components is achieved with any reasonable desktop photo editing suite and the experimental results reflect the theoretical estimation. The computationally generated 'lens' has been graded linearly from the center of the lens to the circumference of the lens however, this grading may not reflect the actual grading relationship found in the experimental images. The colour distributions should be as closer match as possible to the theoretical distributions in order to obtain the largest range of hues in any given experimental image.

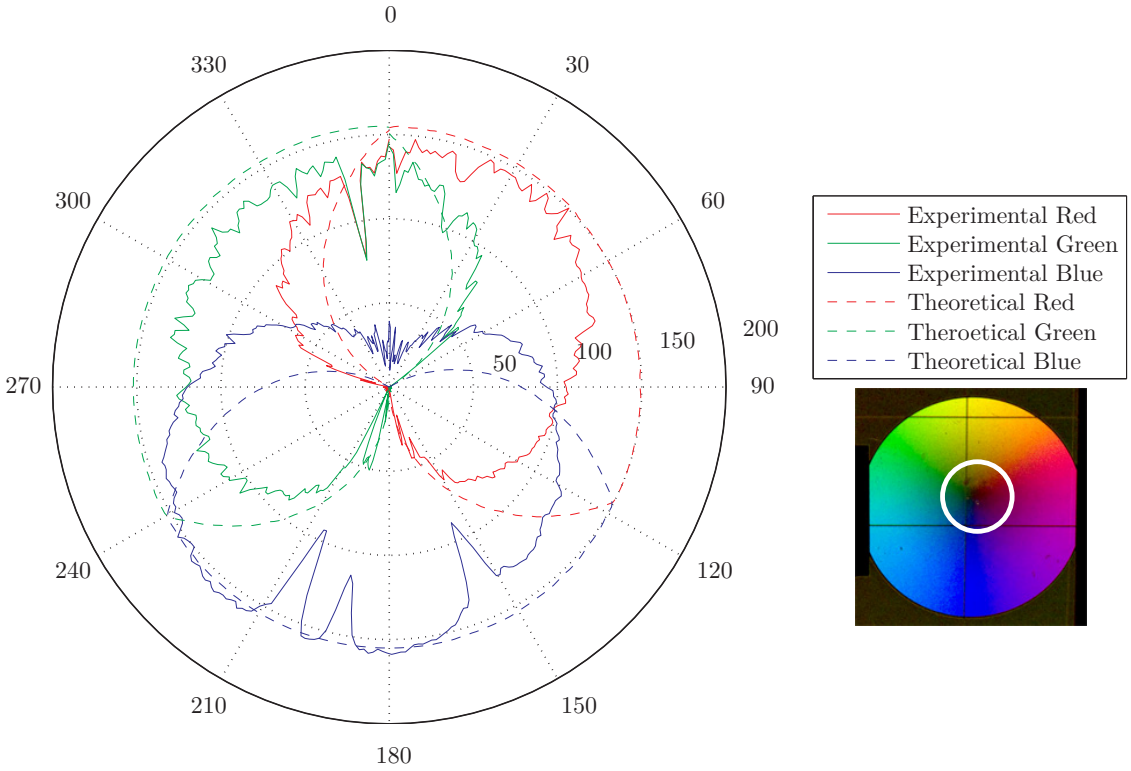


Figure 7.30: 33% calibration lens radius

A more mathematical method of determining the response of the calibration lens to the light passing through it is to extract pixel values and compare the values to what may be expected. Figure 7.30 is a polar plot of the separate monochromatic channel pixel values extracted around the white circular line in the sub-image. The orientation of the polar plot is chosen to match the orientation of the sub-image and thus the colour components at each point may be observed. The image of the calibration lens in the test section has been subjected to an image leveling in order to most accurately portray each colour channels response. This method highlights the optical and imaging response to density gradient magnitude and direction.

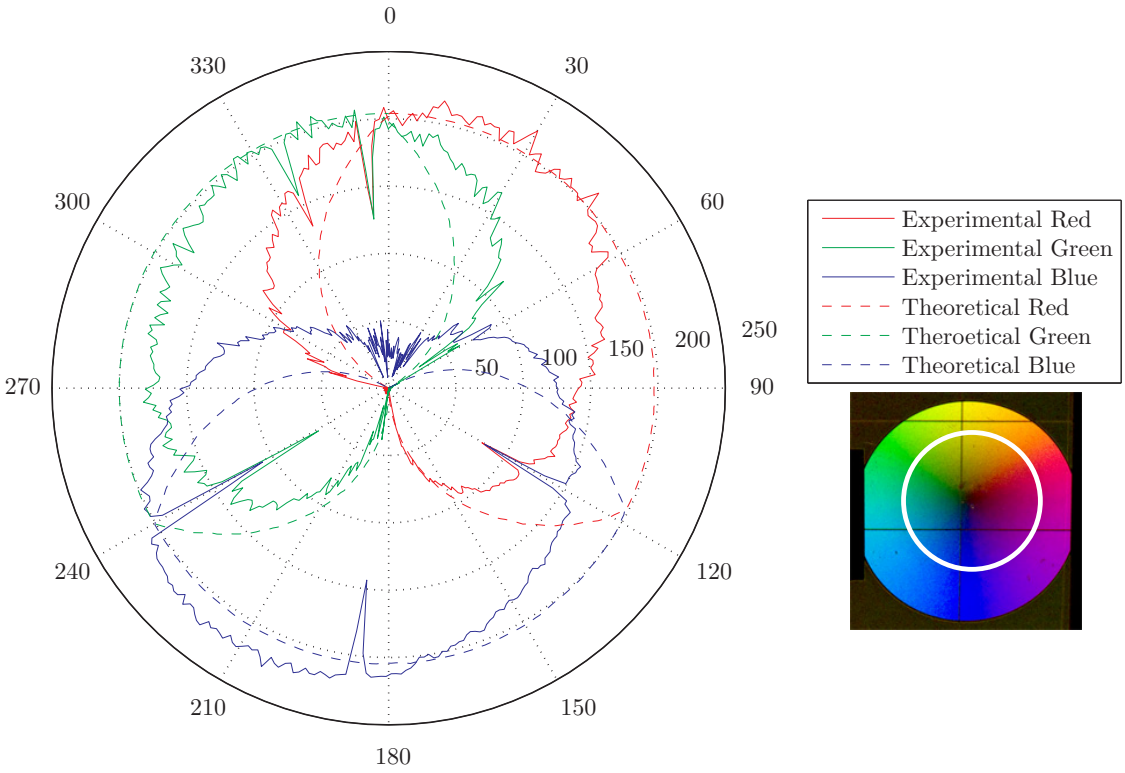


Figure 7.31: 66% calibration lens radius

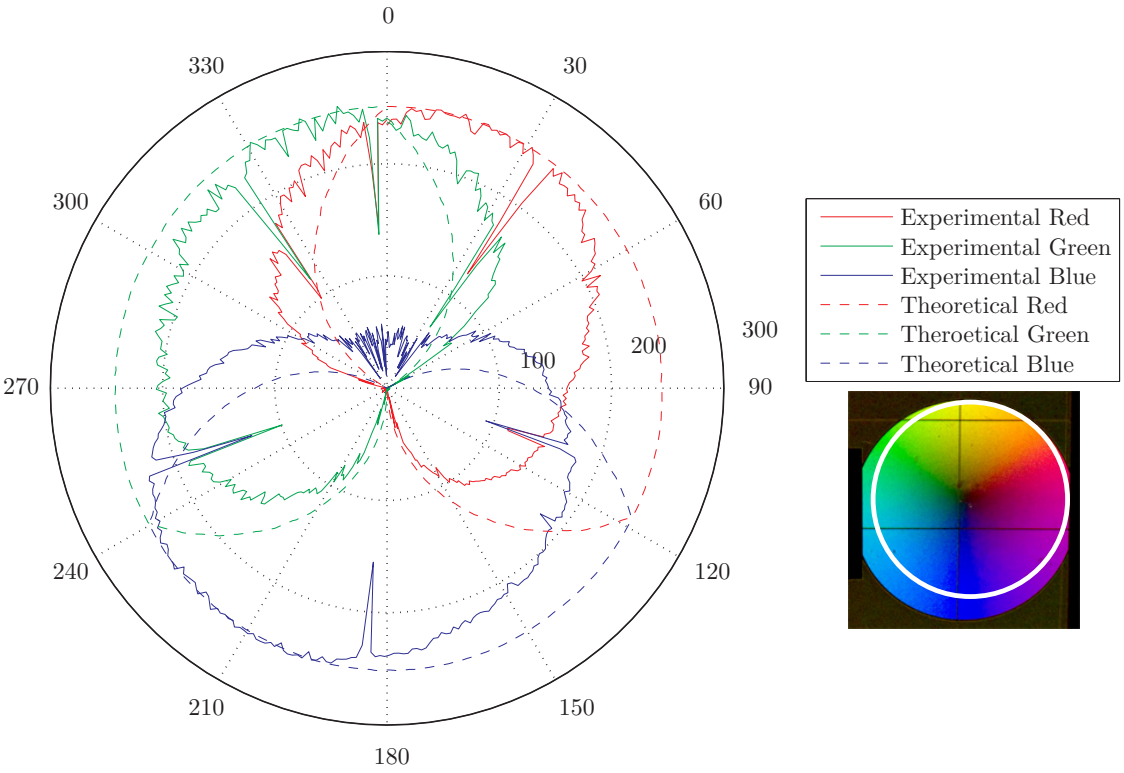


Figure 7.32: 100% calibration lens radius

Figures 7.31 and 7.32 portray the pixel values at 66% and 100% of the calibration lens radius respectively. It is important to note that the white circle is not centered about the physical center of the lens but rather about the position on the lens which exhibits the darkest region. This dark region is the point on the lens which represents zero density gradient magnitude. Further information on the possible reasons for this offset may be found in this section. In all the experimental data extracted from this single calibration lens image, dips and peaks in the data are caused by the various grid lines crossing the test section and thus the pronounced dips and peaks will be ignored in further analysis.

Together with the experimental data, theoretical data is also plotted to provide an approximate reference to what the colour response should be in order to achieve a full colour spectrum. Upon examination of the polar plots it is apparent that there is a significant level of blue noise present in the image. This is due to the inherent sensitivity of the imaging sensors to the blue spectrum. Low level ambient and stray light seems to influence the blue channels before the red and green channels.

The general matching of the theoretical and experimental results is clear however all three plots exhibit a lack in full intensity colour mixing between the red and blue channels creating magenta and similarly, to a lesser extent, between the red and green channels to form cyan.

A similar method of pixel extraction and analysis was conducted in a linear fashion illustrating the response to density gradient magnitude as a function of radial lens position in a single density gradient direction. Pixel values are extracted and split into their monochromatic channels along the white line joining the dark spot on the lens and the outer edge of the lens.

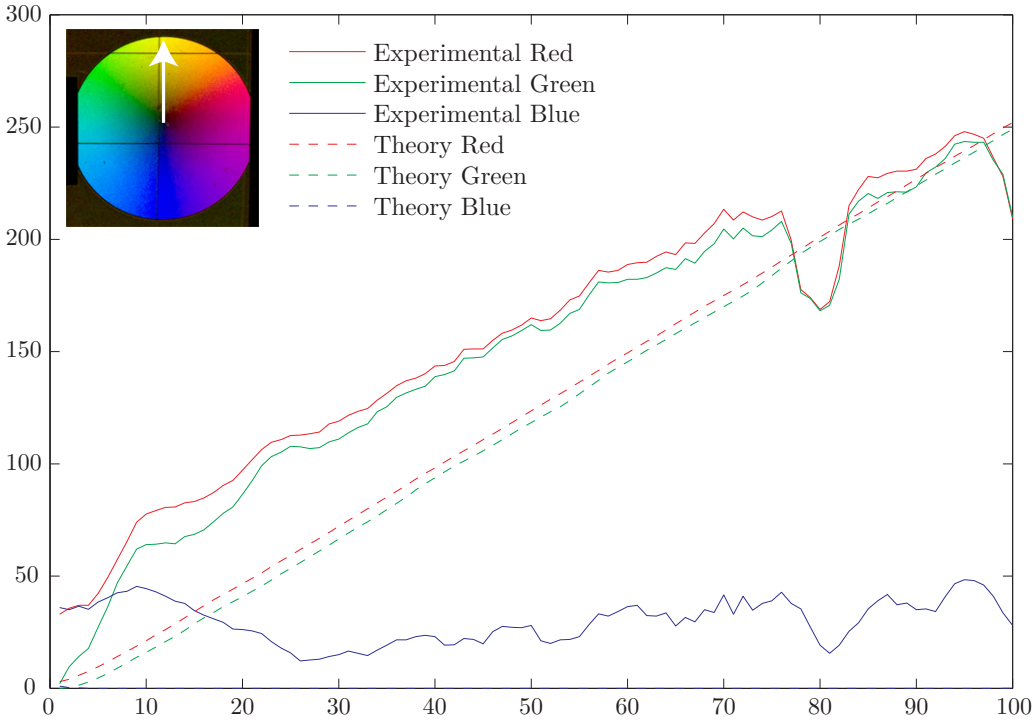


Figure 7.33: Calibration lens response - Yellow

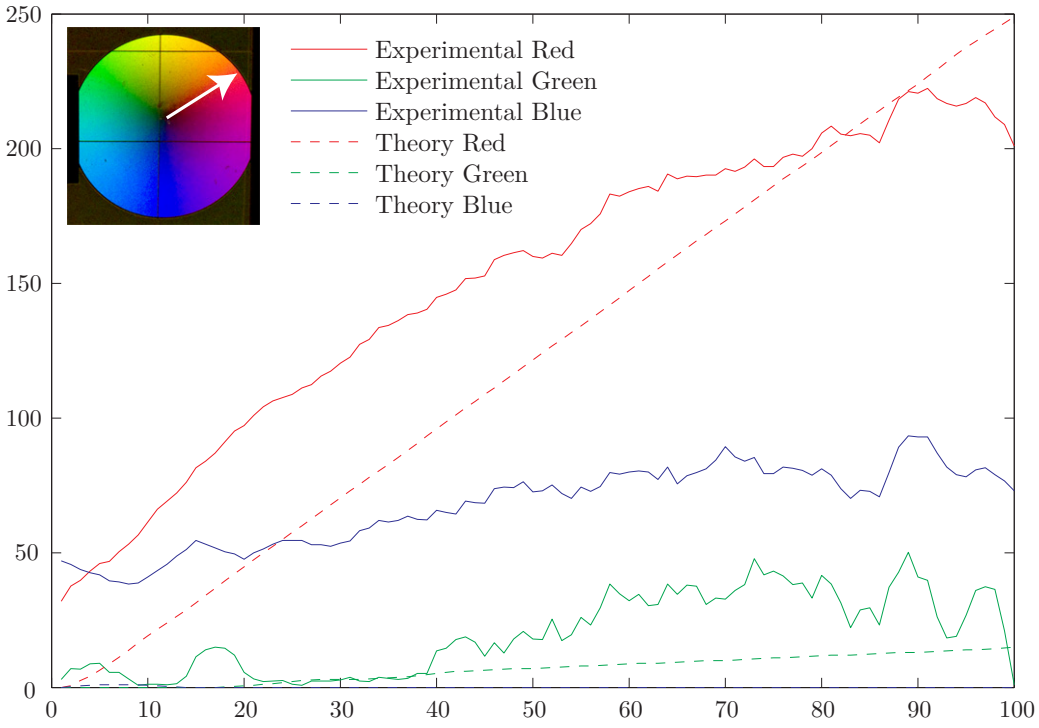


Figure 7.34: Calibration lens response - Red

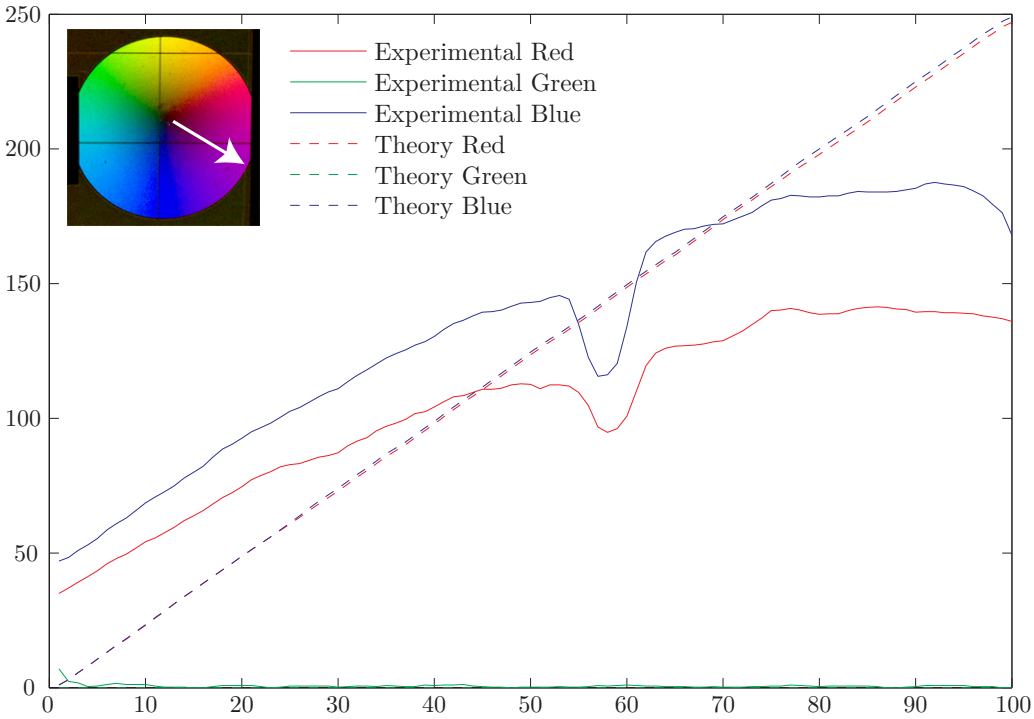


Figure 7.35: Calibration lens response - Magenta

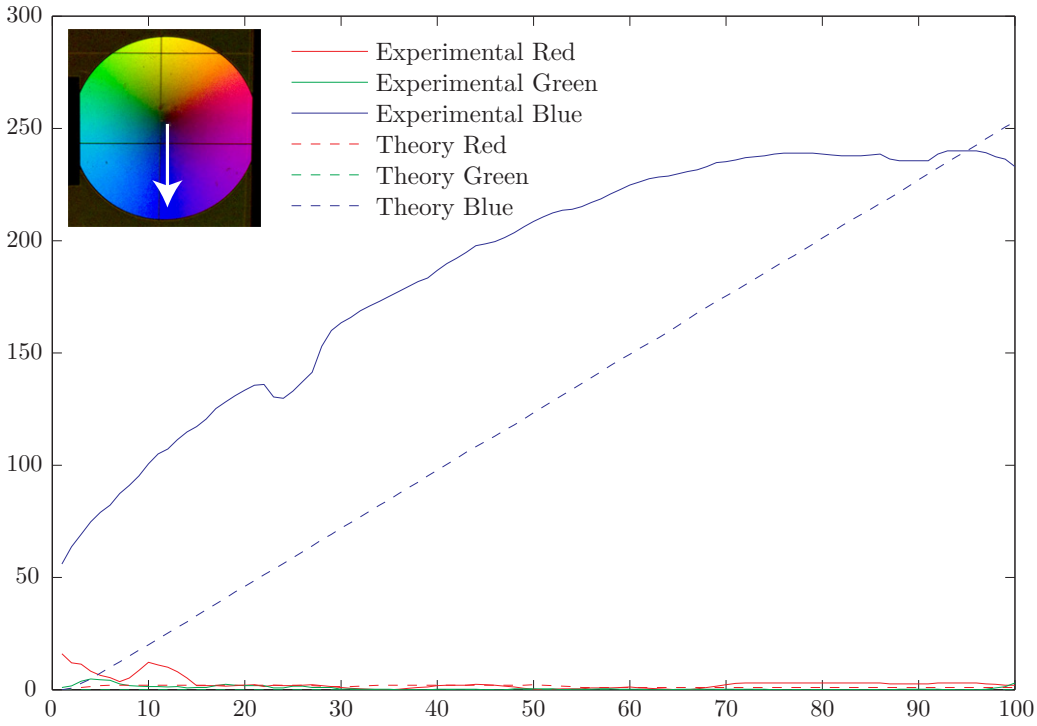


Figure 7.36: Calibration lens response - Blue

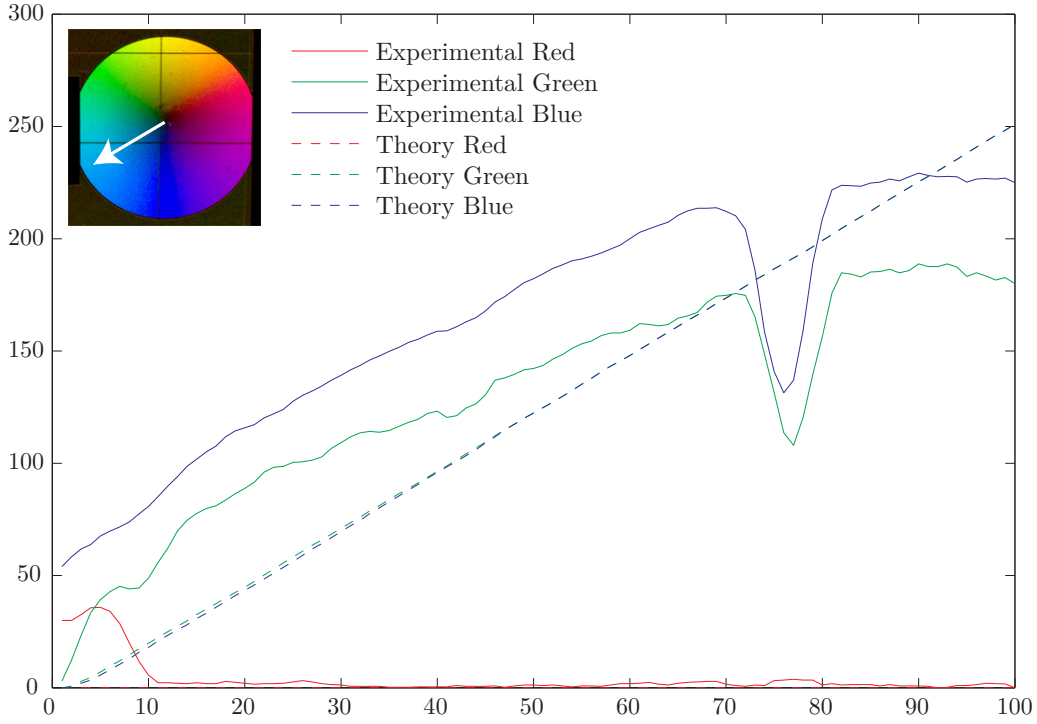


Figure 7.37: Calibration lens response - Cyan

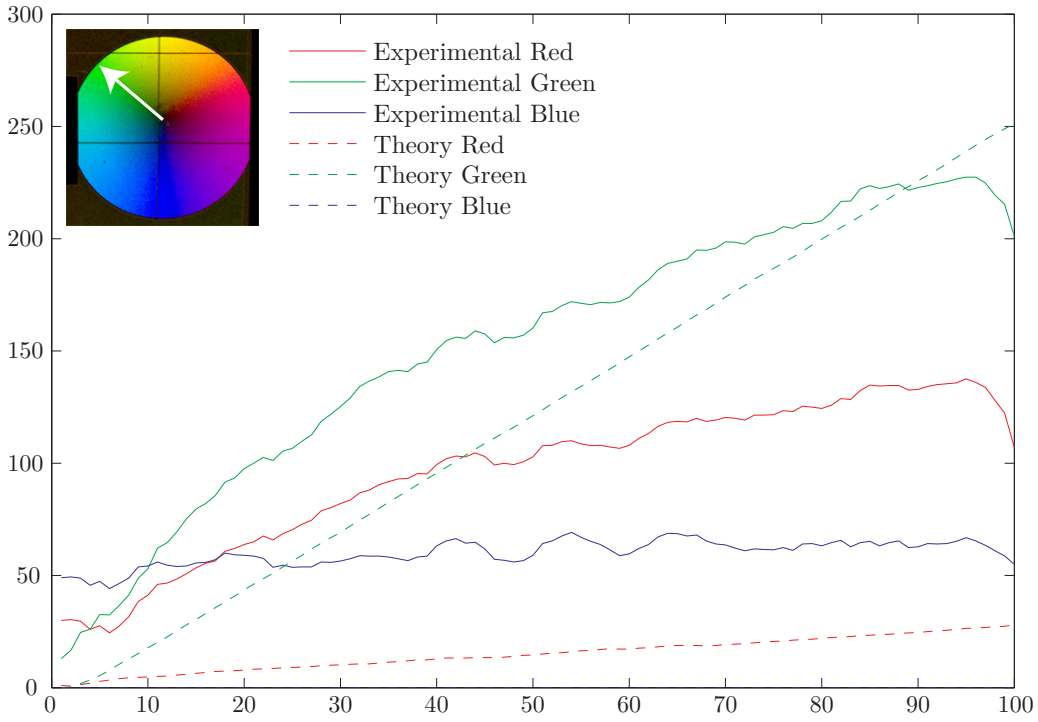


Figure 7.38: Calibration lens response - Green

The results from the linear data extraction are shown in figures 7.33, 7.34, 7.35, 7.36, 7.37 and 7.38 which represent the yellow, red, magenta, blue, cyan and green directions, respectively. Once again, the various significant dips and peaks were caused by grid lines across the test section.

The plots contain theoretical lines illustrating a linear relationship between the pixel value and the lens radius. This linear relationship seems not to be a particularly accurate representation of the experimental results and perhaps an exponential relationship would be more suited.

Examining figure 7.33, it is clear that the ratio between the red and green channels varies relatively uniformly with lens radius. It is also apparent that this relationship has more of a linear response than an exponential response. There should ideally be no blue channel information for this direction however, there is clearly a degree of blue noise present in for this direction with a magnitude averaging in the region of 25 pixel units.

Figure 7.34 shows quite a substantial degree of noise from both the blue and green channels. This may perhaps be due to the fact that the imaging sensor is less sensitive to red hues and thus during the image leveling process, the red channel was enhanced to a greater degree than either the green or blue channels. This leveling process would enhance not only the desired response, but also the noise present in the other colour channels. Again, this response in the red direction seems roughly linear.

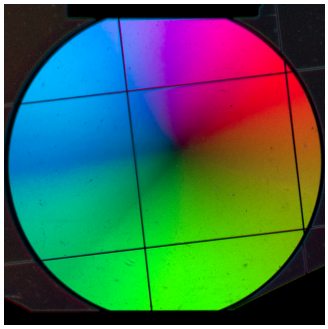
The magenta channel, figure 7.35, illustrates more of an exponential response with the maximum colour intensity not reaching the 200 pixel unit level. This lower maximum intensity

response is in line with the results shown in figure 7.32 for this direction. There is almost no green channel noise present in this direction.

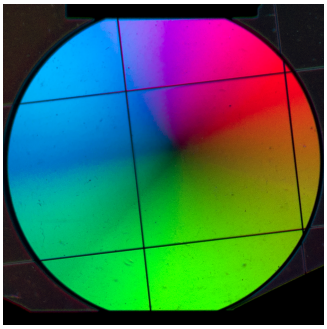
As expected, the blue channel shown in figure 7.36, exhibits little noise from either the red or green channels and displays a particularly exponential response. The hue intensity seems to saturate at about 70% of the lens radius and thus little change in hue intensity occurs after this point. This results in poor quantitative data being extracted from this region of the lens as there is a small variation in intensities over a relatively large section of the lens.

The cyan response, figure 7.37, is similar to the blue response in terms of proportionality. There is a small degree of red noise but nothing to cause significant error in quantitative results. The most red noise occurred in the dark center of the lens where there should ideally be no colour information. This likely to be a result of stray and ambient light refracting through the test section. The uniformity of the colour appears to be consistent along the length of the lens radius.

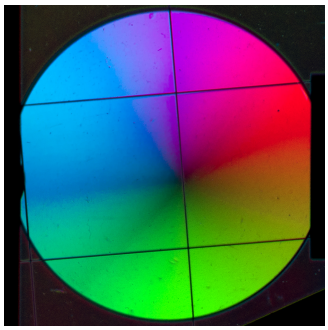
The green channel, figure 7.38, shows some interesting results in that the levels from the blue and red channels are somewhat overwhelming. The intensity of the green response does not reach the full available level of 255 while the red channel exhibits levels of more than half the green response. This may simply be the combination of colours for this direction however the blue channel shows no intensity increase with lens radius and thus the levels in the blue channel are likely to be attributed to noise.



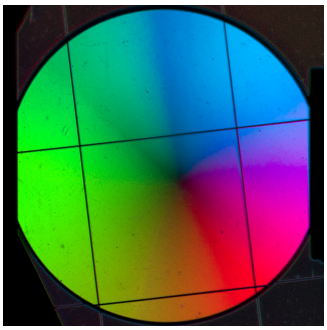
(a) Initial position, 0^o



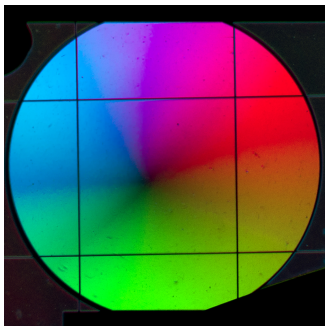
(b) Initial Position, 0^o



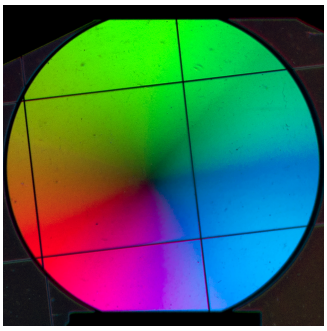
(c) Physically rotated clockwise, 90^o



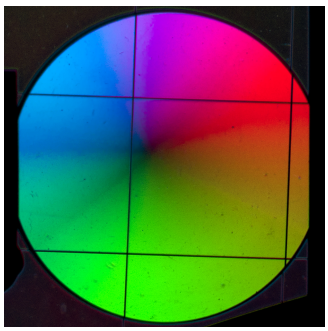
(d) Computationally rotated clockwise, 90^o



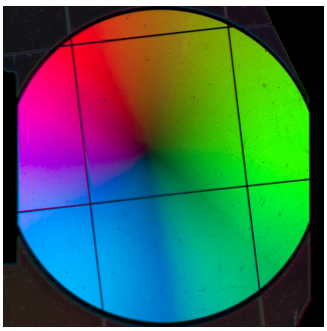
(e) Physically rotated clockwise, 180^o



(f) Computationally rotated clockwise, 180^o



(g) Physically rotated clockwise, 270^o



(h) Computationally rotated clockwise, 270^o

Figure 7.39: Images showing the rotation of the calibration lens within the test section

The method described to obtain quantitative results from experimental images relies on a

method of accurately calibrating the system. The method used to calibrate the system was by means of a large focal length plano-convex lens. An analysis was undertaken into the accuracy of the calibration lens before any attempt was made to use the results from the calibration lens to analyze experimental images. Source mask B was used to capture these images, figure 4.2b and figure 7.14d.

Figure 7.39 shows an interesting outcome related to the accuracy of the manufacture of the calibration lens. The following procedure was followed to obtain this outcome:

- Align the optical system as accurately as possible using laser cross-hairs where possible as well as accurate physical measurements and placements for all components.
- The iris diaphragm was adjusted so as to allow enough light to pass through the cut-off plane and hit the imaging sensor as shown in figure 7.39. The background illumination was adjusted to obtain the most even possible intensity and hue regardless of the dark spot position on the calibration lens.
- The calibration lens was placed in a lens holder and positioned just outside the test section doors, with the doors firmly closed.
- Four images were taken of the calibration lens; at four angles of rotation in a clockwise fashion. The lens holder was not rotated by exactly 90 degrees each time which is evident by the marginally angled grid lines covering the test section. The lens was kept planar and normal to the optical axis as well as being rotated about its center.
- It is important to note that no other optical components were adjusted or moved in any way when taking these four images.

The result of this analysis proves that the optical center of the lens seems to vary according to the rotation of the lens. With each of the physically rotated lens images it is clear the colour combinations do not shift. This is expected since the light passing through the lens will do so, and refract, no matter the orientation of the lens. To further prove the optical center of the lens is non-concentric, the initial image has been computationally rotated by the same amounts and, as expected, the dark optical center of the lens coincides with the experimentally rotated lens.

One argument to these results is that if the dark spot was centrally positioned and the lens rotated, there would be no visible shift in the optical center of the lens. However, if no optical adjustments are being made to the system between shots and the dark spot has purposefully been offset to test the lens accuracy then there should be no reason for the dark spot on the lens to shift unless there is some kind of optical flaw in the manufacture of the lens.

If the lens was 100% accurate with the optical center coinciding with the physical center of the lens, the light would pass through the lens the same way regardless of the angle of rotation of the lens. This is not the case and it has been proven, through the discussion of the figures above, that the lens exhibits a shifted optical center.

Furthermore, it was found that when the dark spot was centralized to coincide with the physical center of the lens, the background hue became significantly biased towards one colour and a uniform hue was unachievable.

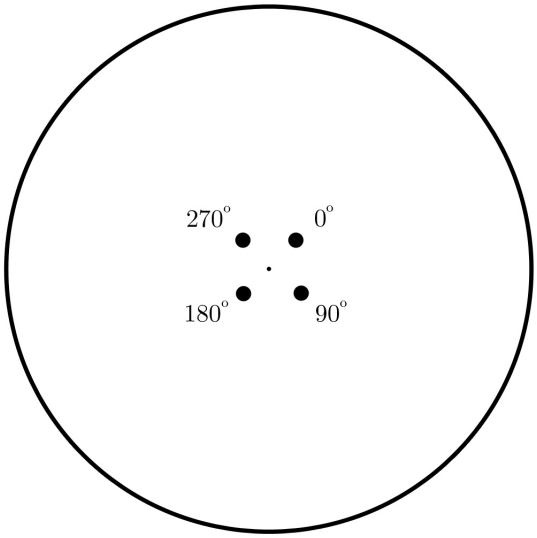
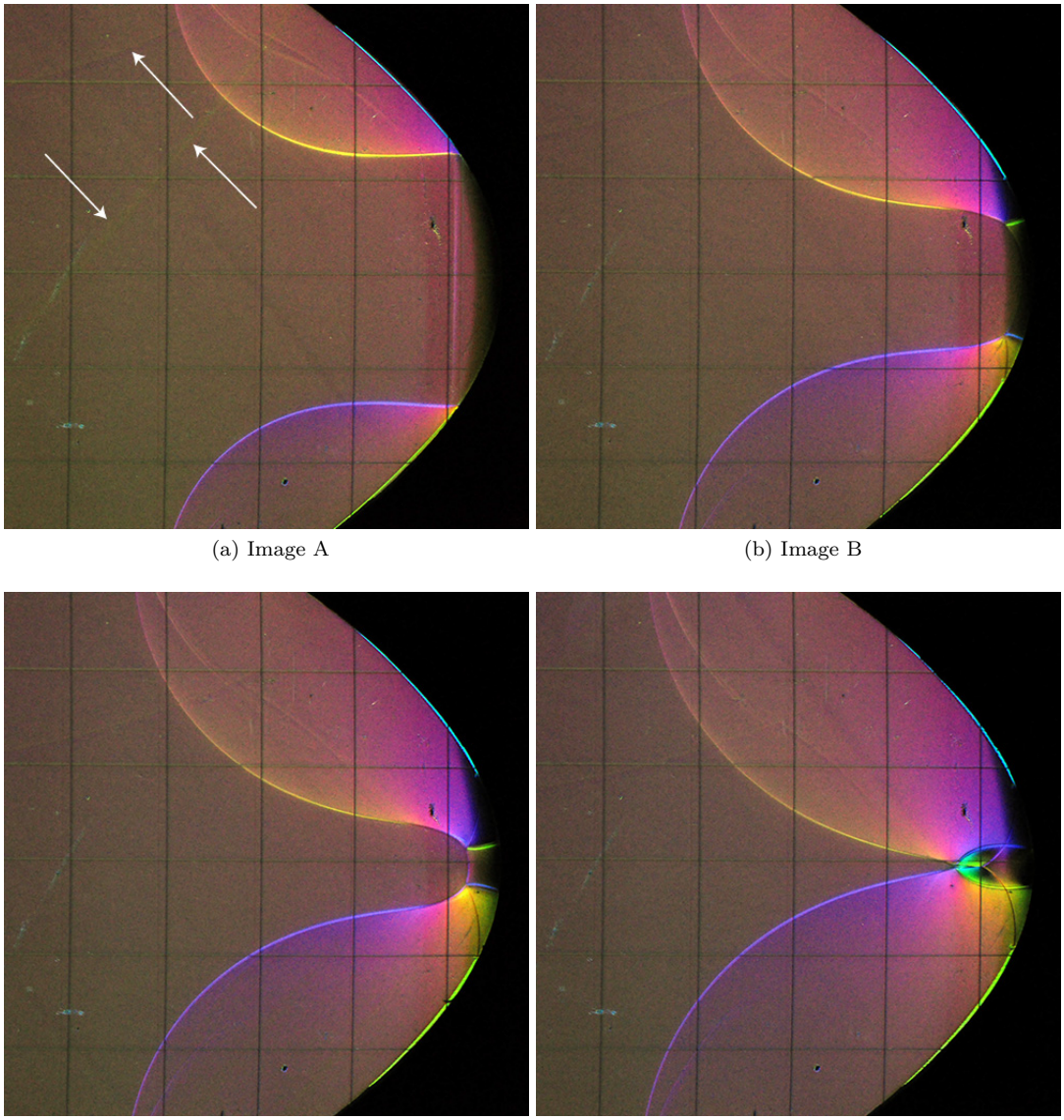


Figure 7.40: Extracted center positions

The physically rotated dark spots on the calibration lens were extracted and mapped onto a mask with the results shown in figure 7.40. It is quite clear that for each approximate 90 degree rotation, the dark spot rotates by approximately 90 degrees in the direction of rotation.

7.3.2 Image palette

This section contains a number of sequenced shock reflection images taken with the colour schlieren system as well as comparison between RAW and JPEG file formats. Due to the LED light source's incapacity to produce enough light in a $1 - 2\mu s$ range, the conventional xenon flash lamp is used to capture the images in this section. The source mask used to capture all images in this section may be seen in figure 4.2d and figure 7.14b



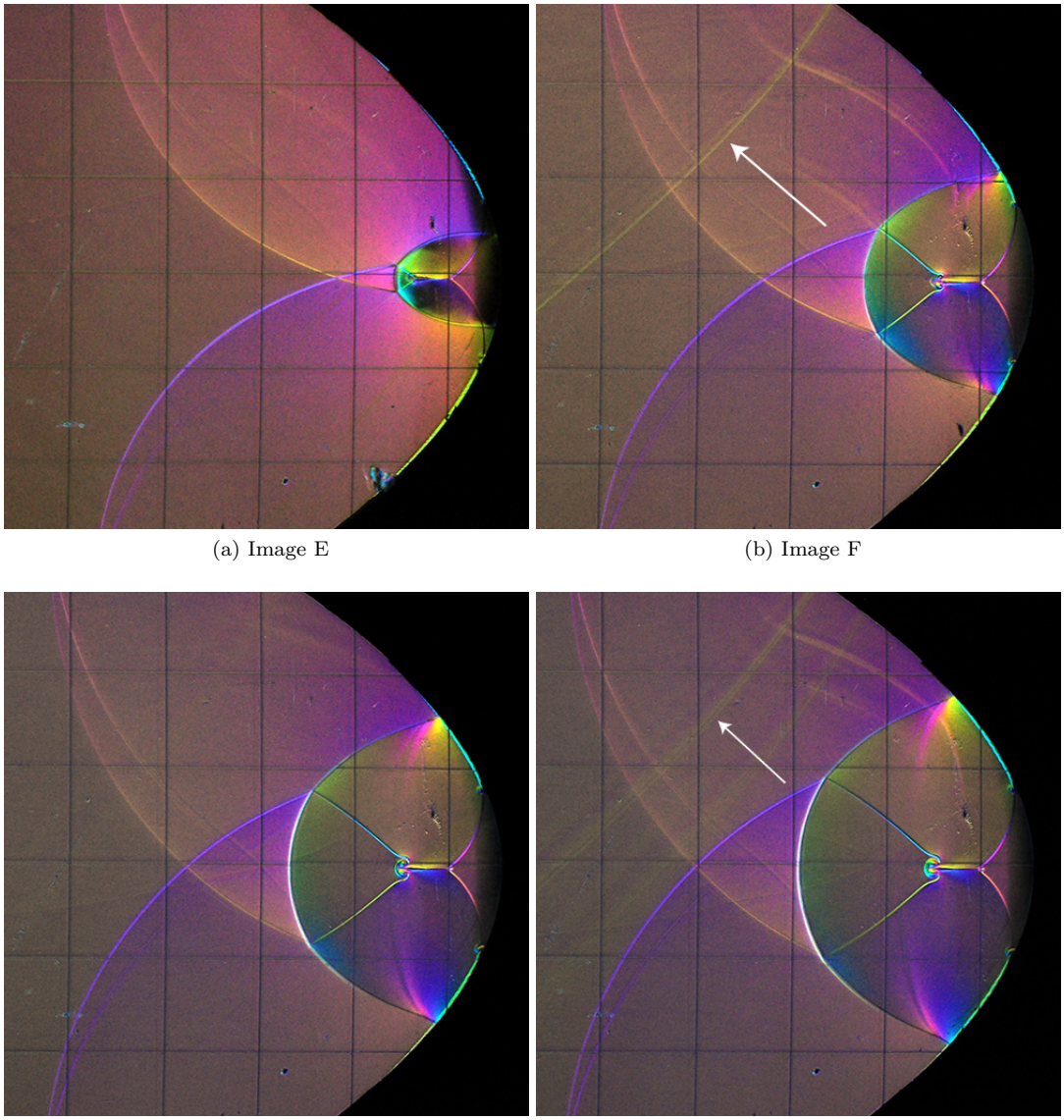
(a) Image A (b) Image B

(c) Image C (d) Image D

Figure 7.41: Progression of shock wave at $20\mu s$ intervals prior to shock focus

Image A in figure 7.41 exhibits weak transverse shocks traveling through the test section indicating a sensitive schlieren system. These transverse shocks however do not contain enough colour information to obtain quantitative data.

The images exhibit a darkening on the test model face at the extreme right and this is due, in part, to non-parallel light passing through the test section which is effectively causing a shadow cast by the light source side of the test model.



(a) Image E

(b) Image F

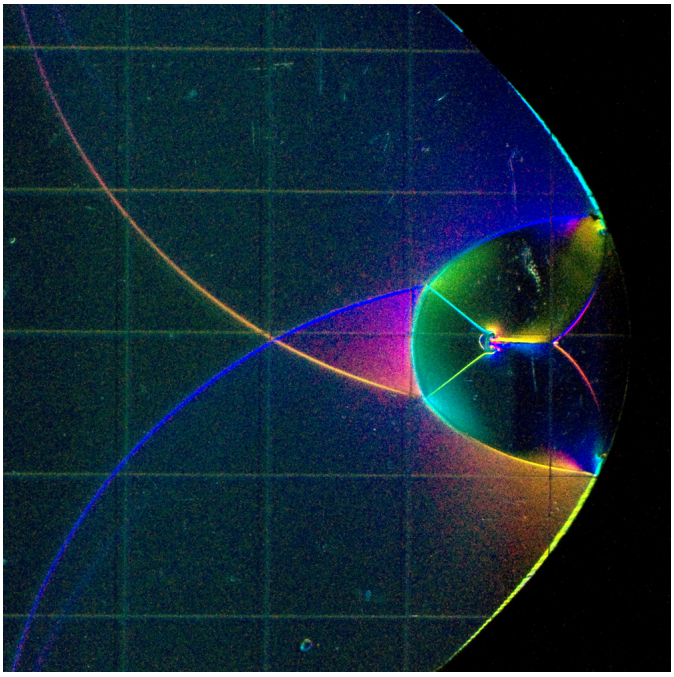
(c) Image G

(d) Image H

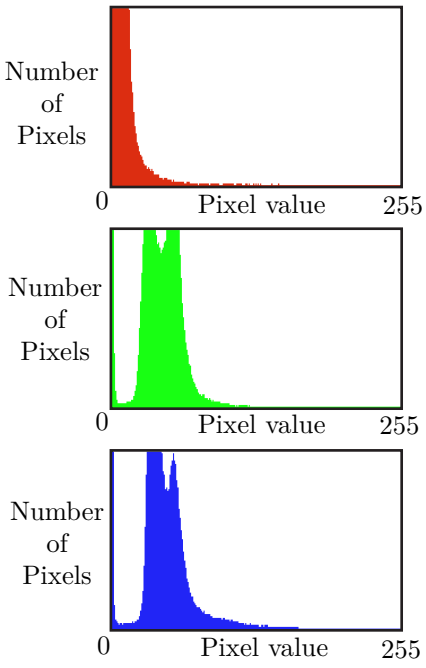
Figure 7.42: Progression of shock wave at $20\mu s$ intervals after shock focus

Figure 7.42 exhibits shock waves after they have formed into a focal point by the test model. The density gradients around the focal region begin to reduce in magnitude and all sub-images show some degree of transverse shock waves in the test section. These transverse shocks may be due to diaphragm pieces in the shock tube moving and changing position in each subsequent test or they may be created by anomalies in the shock tube itself such as protruding pressure transducers.

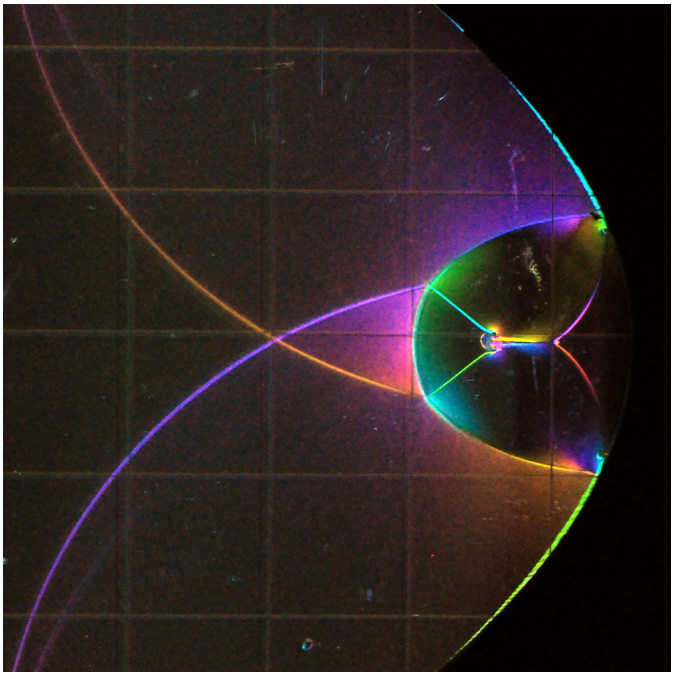
The clarity and sharpness in all images have not be adjusted and only the colour balance and intensities have been modified. The light source for these tests was the $1.5\mu s$ xenon strobe and the continuously blended source mask was used.



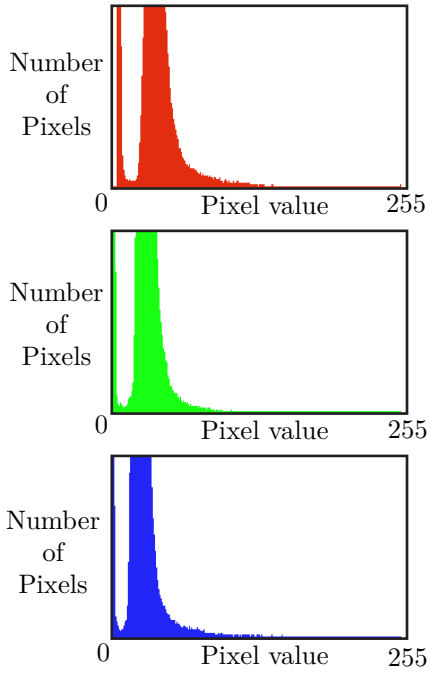
(a) RAW Image



(b) Raw Levels



(c) JPEG Image



(d) JPEG Levels

Figure 7.43: Raw and Jpeg image comparison

Most higher end imaging sensor systems have the ability to record RAW files containing the unmodified light intensity data directly from the sensor itself. Figure 7.43 illustrates the difference between an unmodified RAW image and a compressed JPEG image. Each image is paired with the corresponding image levels present in that image. For this particular

image, the RAW red channel is weaker than either the blue or the green channels. The JPEG image has more even levels with the red channel slightly more pronounced than the other channels.

This comparison is used simply to highlight the importance of using like images for a comparison between hues and intensities. It is possible to convert a RAW image to JPEG however the image colours and hues will need to be exactly matched or there will be an offset in any measured data. The methods described herein work regardless of the image type used provided both the calibration image and the experimental image are the same type and are taken with no adjustment to any of the optical components.

Chapter 8

Conclusions

The investigation into a quantitative colour schlieren system has resulted in a system which has the capability to produce quantitative results. The schlieren components and system as a whole have been improved significantly and as a result, the system now has the capacity to produce higher quality colour images with the added benefit of quantitative analysis. It was found that the system was able to produce images in which quantitative information could be extracted. The accuracy and quality of this quantitative data is limited and as such the system is perhaps more suited to qualitative results until it is refined further. Images from constant fluid flow fields may prove to yield improved quantitative data since higher powered light sources may be used.

The digital design and generation of the source masks have, in general, increased the image quality and quantitative potential for the schlieren system. The production process reduces the likelihood of errors being introduced by mis-shapen hand designed masks and allows a precise ratio of the width and height of the masks to be controlled to counteract the effects of the cylindrical lens employed to reduce astigmatism. The source code allows quick generation of a number of masks to be produced with different configurations. It was found that the continuously blended source masks improve the colour blending properties and result in higher quality, quantitatively viable, images.

The Euler based CFD simulations compiled and run from within the C++ environment have resulted in flow field density distributions similar to those found experimentally. The CFD results did not originally contain colour schlieren information and as a result colour schlieren code was generated to run within Tecplot as a script. The colour schlieren script has shown a large degree of flexibility in producing results which accurately represent the experimental results. The script may be used as a quantitative or qualitative tool to analyze CFD results and has the potential to be modified to encompass monochromatic schlieren as well. There is potential to move the colour schlieren script out of Tecplot and into a non scripted language to improve processing time and efficiency.

It was found that the colour schlieren system is more complex to set up and the alignment is crucial to obtain a quality image. The use of a cylindrical lens specifically with low

f number mirrors is imperative to obtain reasonable focus in the cutoff plane. Since the source masks are of a finite width and height, the effects of astigmatism and non-parallel light passing through the test section are greatly exaggerated. Ideally, source masks with smaller dimensions should be used, however, the means to cut this light off in the image cut off plane becomes increasingly difficult with conventional iris diaphragms. This is due to the total area of the iris aperture the light must pass through being restricted by an exponential amount as the aperture is stopped down. It was found that the test section doors of the Seitz shock tube were not 100% true and as such, the light passing through them was shifted. It was also found that the amount the light was being shifted was not uniform over the entire glass door area, indicating some kind of manufacturing inconsistencies.

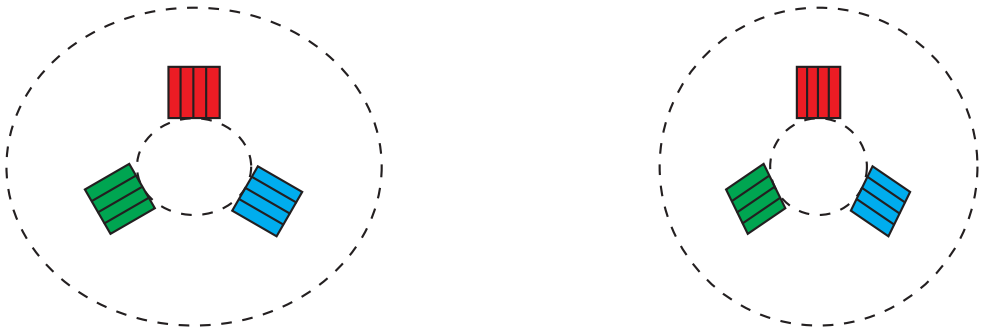
An LED light source was designed and built with the hope of improving the current xenon flash lamps. The LED light sources showed an improved wavelength spectrum which in turn improved the colour reproduction in the colour schlieren system. They also drastically improved the set up time of the optics since a constant on mode was available. Unfortunately, the nature of the current low cost LED's means they are not able to produce the required amount of light to successfully illuminate a source mask as well as lose a lot of light due to the cylindrical lens. The pulse duration of the LED light source is more than adequate with pulse times as low as $800ns$. Higher power, higher output LED's are under constant development and as technology improves, the LED light source will become a more viable option. New research is also being undertaken into the effect of high current, low duration pulses on the electronic components within the LED and this will result in LED's evolving to suit these requirements.

The means of analyzing experimental images was designed using a large focal length calibration lens to emulate the effects of changing refractive indices within the test section. A calibration image was taken before any experimental images and no system adjustments were made in between photos. The light passing through the lens is refracted, in all directions and at vary degrees of refraction magnitude, in a normal plane to the optical axis. This results in a complete map of all possible colour combinations and hues which will be produced by the schlieren system when light passes through a density field within the test section. The colour hues and intensities in both the calibration image and the experimental test image were then compared and since the density gradient magnitudes and directions are known for each position on the calibration lens, the information may be directly compared to the experimental image. This method has mixed results, mainly due to the quality of the images obtained. The xenon and LED light sources did not produce enough illumination to adequately expose the imaging sensor and thus the ISO of the sensor had to be boosted. This boost in sensor sensitivity results in a significant increase in noise generated and stored in the image. The full range of colours is thus also not fully utilized and the images have to undergo an image leveling procedure which not only boost monochromatic colour channel levels but it also amplifies the noise. All these techniques to amplify the image response increase the visual appeal of the image but do little to improve the information carrying capacity of the image.

Chapter 9

Recommendations

Although the source mask system provides a good array of results, there may perhaps be a more efficient way of producing a 2 dimensional colour schlieren system using an array of LED's instead of a fixed source mask. The method would require the array to take into account the distortion introduced into the system by the cylindrical lens. This distortion and is the primary reason the method was not followed as the design of an accurate piece of equipment to finely adjust each colour LED diode, before the proof of concept of a source mask based colour schlieren system, would simply be too expensive.



(a) Physical layout of 3 colour LED diodes prior to passing through cylindrical lens

(b) Virtual image of the 3 colour LED diodes after passing through cylindrical lens

Figure 9.1: Figure of a possible LED layout to replace the source mask

The results presented in this dissertation show how a relatively simple method may yield quantitative results from experimental images. The improvement of the light source end of the schlieren system would result in a far more efficient lighting system in terms of light scatter, colour reproduction and adjustability. Figure 9.1 illustrates a possible arrangement of 3 LED diodes around a part with either fixed or adjustable positions made possible by some mechanical means. The hyphenated lines show the possible iris diaphragm position in the cut off plane. There is a degree of ratio change in the size of the LED diodes however, there should be no effect on the images produced. This concept of emitting light is based on

the method by Scott et al. [1991], however, instead of employing colour masks to block out unwanted wavelengths of light for each 120 degree section, a specific wavelength LED with adjustable intensity could be used. The LED's would have to be arranged in such a way as to be aligned at 120 degrees to one another after passing through the cylindrical lens.

This method negates the need for complicated source masks to be produced as well as a light wasting diffusing screen. Typical LED's are Lambertian by nature and thus they throw light in all directions by default. The LED arrangement wouldn't allow for a constantly blended light source as seen in the HSV blended colour wheels, however, LED's would allow a more precise and repeatable wavelength of colour to be produced. The intensity of each LED would also be able to be adjusted finely using some basic current limiting electronics and so the precise amount of light forming each direction may be produced. This method would also allow a general spectral shift to be recorded quite easily using the standard imaging sensor when pulsing the LED's.

Other recommendations include:

- Further the design of the LED light source using the latest highest powered LED's.
- Improve Luke's code CFD routines to employ multicore processing which will drastically reduce computation time.
- Analyze the test section doors on the Seitz tube and replace the ones causing optical distortions.
- Address the reliability issues of the Seitz tube electronics systems to reduce the likelihood of premature flash firing.
- Update the image processing library, OpenCV, to use a blob tracking system to automatically locate, refine and extract quantitative information from the calibration images instead of having to extract data point by point manually.

Bibliography

P. Balachandran. *Gas Dynamics For Engineers*. Prentice-Hall Of India Pvt Ltd, 1 edition, 2010. ISBN 9788120340213. URL `http://books.google.co.za/books?id=6p4fgrGUG_8C`. ISBN 8120340213.

D.R. Buttsworth and T.L. Ahfock. A pulsed led system for schlieren flow visualisation. Technical report, Faculty of Engineering & Surveying, Queensland, March 2003.

P.H. Cords. A high resolution, high sensitivity color schlieren method. *SPIE Journal*, 6: 85–88, 1968.

Cree. Xlamp mc-e led, January 2011a. URL `http://www.cree.com/products/xlamp_mce.asp`.

Cree. Pulsed over-current driving of xlamp led's. Technical report, Cree, 2011b.

G.E. Elsinga, B.W. van Oudheusden, F. Scarano, and D.W. Watt. Assessment and application of quantitative schlieren methods with bi-directional sensitivity: Ccs and bos. Technical report, France, 2003.

Douglas A. Feikema. Quantitative rainbow schlieren deflectometry as a temperature diagnostic for spherical flames. Technical Report NASA 2004-212955, NASA STI, June 2004.

Luke Timothy Felthun. Finite element analysis of compressible flows. Technical report, University of the Witwatersrand, Johannesburg, 1995.

Roland Haitz and Fred Kish. The case for a national research program on semiconductor lighting. Technical report, Hewlett-Packard Company, 1999.

Hamamatsu. Xenon flash lamps, 2005.

Michael J Hargather, Michael J Lawson, Gary S Settles, Leonard M Weinstein, and Sivaram Gogineni. Focusing-schlieren piv measurements of a supersonic turbulent boundary layer. *American Institute of Aeronautics and Astronautics*, 2009.

A. F. Ibarreta and C. J. Sung. Determination of flame location using rainbow schlieren deflectometry. Department of Mechanical and Aerospace Engineering, Case Western Reserve University, Cleveland, 2000. The Combustion Institute.

National Instruments. Ni pci-6110 technical brochure, 2004. URL http://www.ni.com/pdf/manuals/370980a.pdf.

National Instruments. Ni pci-6224 technical information, 2008. URL http://sine.ni.com/ds/app/doc/p/id/ds-15/lang/en.

Harald Kleine. *Measurement Techniques and Diagnostics*, volume 1, chapter 5, pages 683–740. Handbook of Shock Waves, 2000.

Harald Kleine and H. Gronig. Color schlieren methods in shock wave research. *Shock Waves*, pages 51–63, 1991.

N Suresh Kumar, A Vallavaraj, and S Salivahanan. *Electronic devices and circuits*. Tata McGraw-Hill Education, 2008.

Peter A. Leptuch and Ajay K. Agrawal. High-speed rainbow schlieren visualization of an oscillating helium jet undergoing gravitational change. 2003.

Steve Luck. *The practical illustrated encyclopedia of digital photography*. Hermes House, London,, 2009.

Deborah Morley and Charles S. Parker. *Understanding Computers: Today and Tomorrow, Comprehensive*. Cengage Learning, 2009.

National-Semiconductor. 54121/dm54121/dm74121 one-shot with clear and complementary outputs, 1995.

W.J. O'Hagan, M. McKenna, D.C. Sherrington, O.J. Rolinski, and D.J.S. Birch. Mhz led source for nanosecond fluorescence sensing. *Measurement Science and Technology*, pages 84–91, 2002.

DC Oren, RP Durrett, and CR Ferguson. Bullseye color schlieren flow visualization. In *Experiments in Fluids*, volume 6, pages 357–364. Springer, 1988.

Photron. Fastcam sa5, 2011.

M.C. Potter and D.C. Wiggert. *Schaum's Outline of Fluid Mechanics*. Schaum's Outline Series. McGraw-Hill Contemporary Learning, 2007. ISBN 9780071487818. URL http://books.google.co.za/books?id=Xhlc4MLYQ7gC.

Ethirajan Rathakrishnan. *Applied Gas Dynamics*, volume 1. Wiley, 2010.

H. Schardin. Schlieren methods and their application. Technical Translation NASA TT F-12,731, NASA Technical Translation, 1942.

D M Scott, M W Seitz, and B W Skews. A fully two-dimensional colour schlieren photographic technique. Technical report, The University of the Witwatersrand, 1991.

M W Seitz. Shock wave interaction with porous foams. Technical report, The University of the Witwatersrand, 2001.

G. S. Settles. *Schlieren and Shadowgraph Techniques*. Springer, 2001.

Gregory Hallock Smith. *Camera lenses: from box camera to digital*. SPIE Press, 2006.

Uwe Steinmueller and Juergen Gulbins. *The Digital Photography Workflow Handbook*. O'Reilly Media, Inc., 2010.

C C Ting, S J Wu, J S Huang, H D Lin, and Y B Luo. The improvement of color schlieren technique by using an lcd projector. Taichung, 2004. AASRC/CCAS Joint Conference.

Zhengji Zhang. *LDA Application Methods: Laser Doppler Anemometry for Fluid Dynamics*. Springer, 2010.

Appendices

Appendix A

LED light sources

A.1 LED Circuit

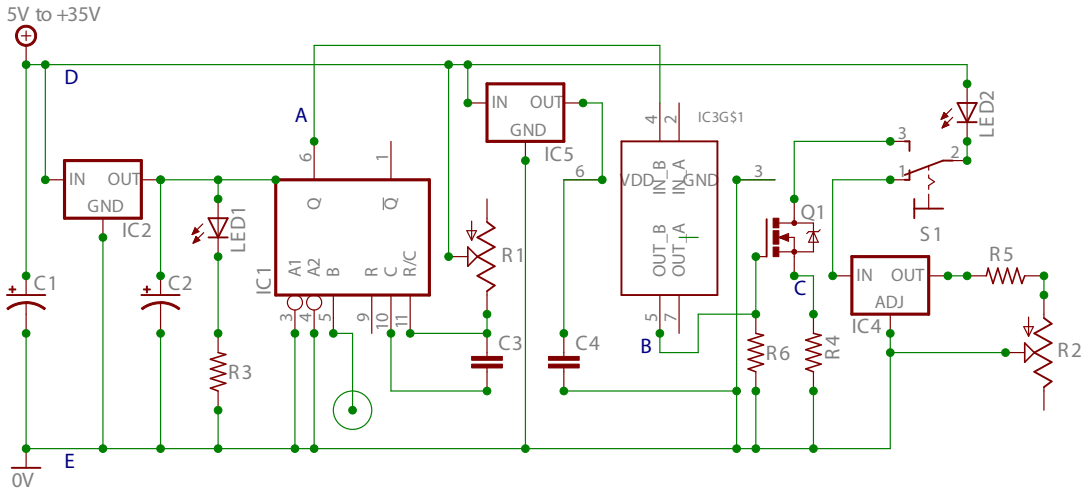


Figure A.1: High power LED circuit

Circuit Code	Value	Details
C1	$220\mu F$	50v, Electrolytic
C2	$220\mu F$	50v, Electrolytic
C3	$100pF$	Ceramic
C4	$0.1\mu F$	Ceramic
R1	$20k\Omega$	Variable resistor trim-pot
R2	Variable depending on LED	Variable resistor
R3	$1k\Omega$	1/4 watt
R4	1Ω	1/4 watt
R5	Variable depending on LED	Power depends on MAX draw of LED
R6	$100k\Omega$	1/4 watt, Pull down resistor
IC1	DM74121N	Monostable Vibrator
IC2	7805	5v Voltage regulator
IC3	TC4427CPA	MOSFET driver
IC4	LM317	Voltage/Current regulator
IC5	7812	12v Voltage regulator
Q1	IRL520A	MOSFET
S1	Switch	Single Pole Single Throw (SPST)
LED1	3mm Red LED	Power indicator LED
LED2	High power LED	Various high power LED's

Table A.1: Circuit bill of materials

A.2 Buttsworth et al. LED circuit

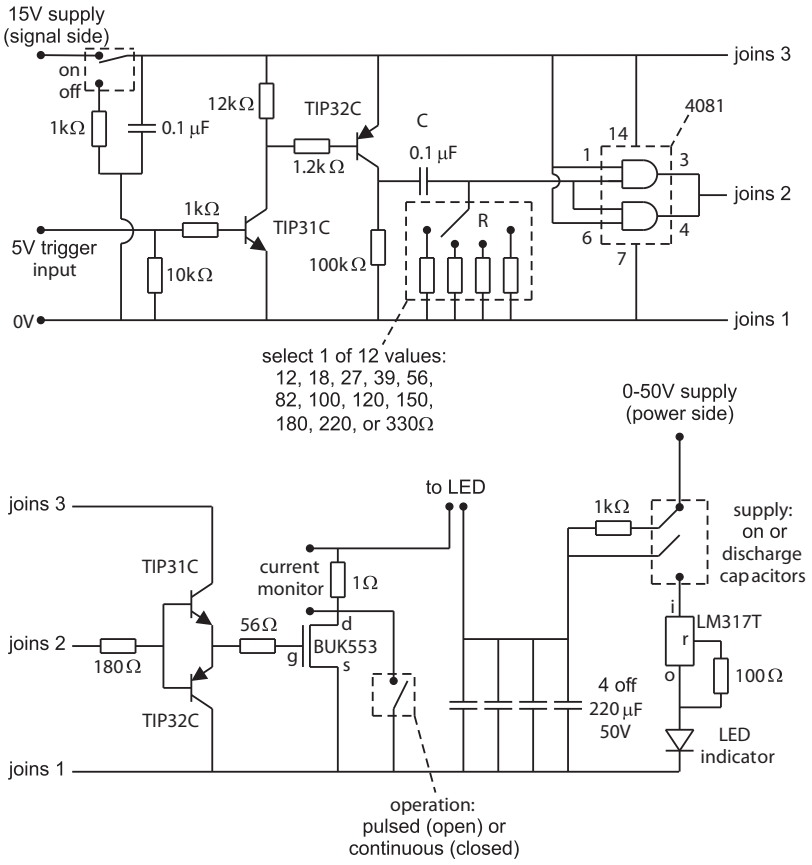


Figure A.2: Excerpt fromButtsworth and Ahfock [2003]

A.3 Hargather et al. LED circuit

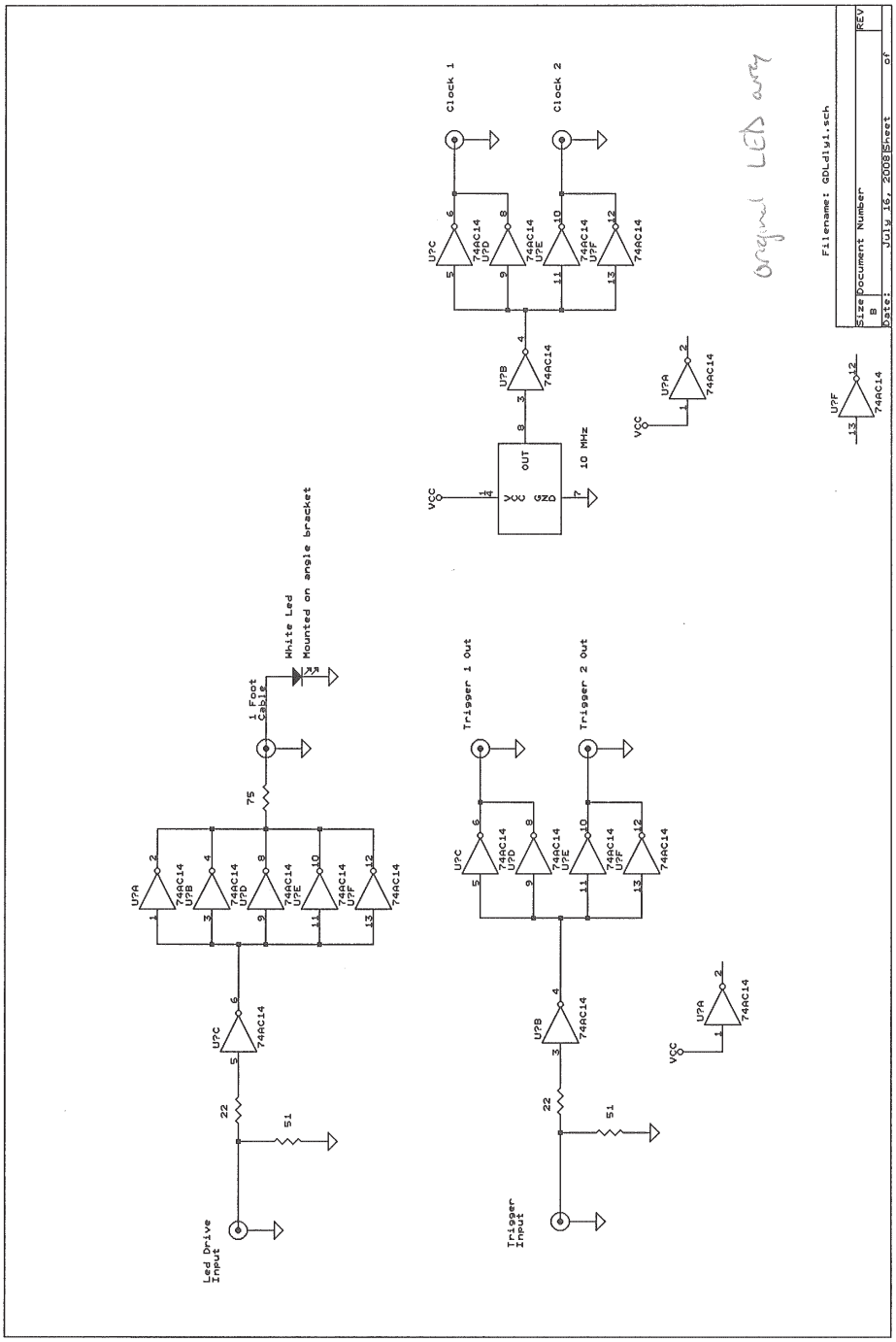


Figure A.3: Original 1 LED system Hargather et al. [2009]

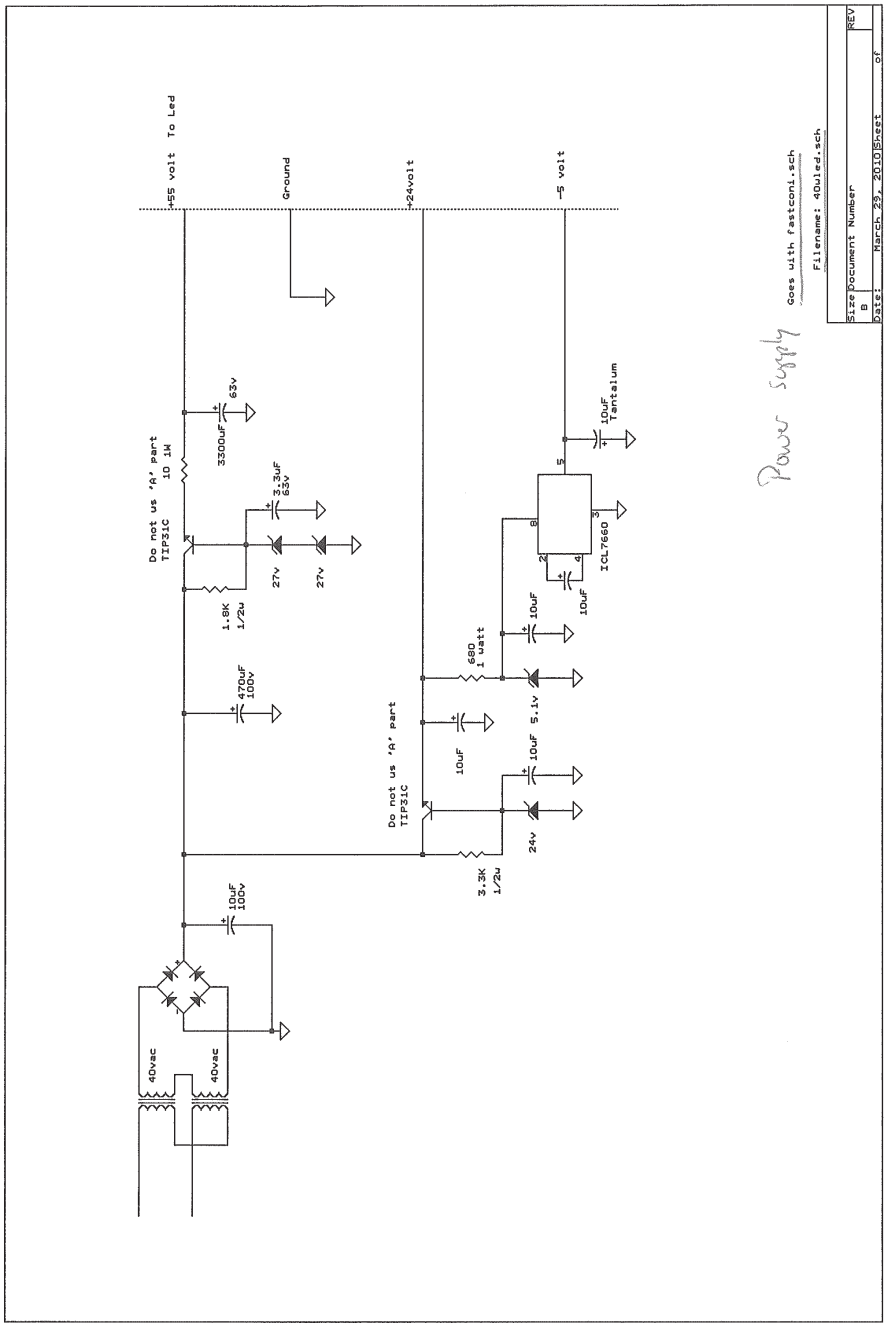


Figure A.4: High power LED power supply Hargather et al. [2009]

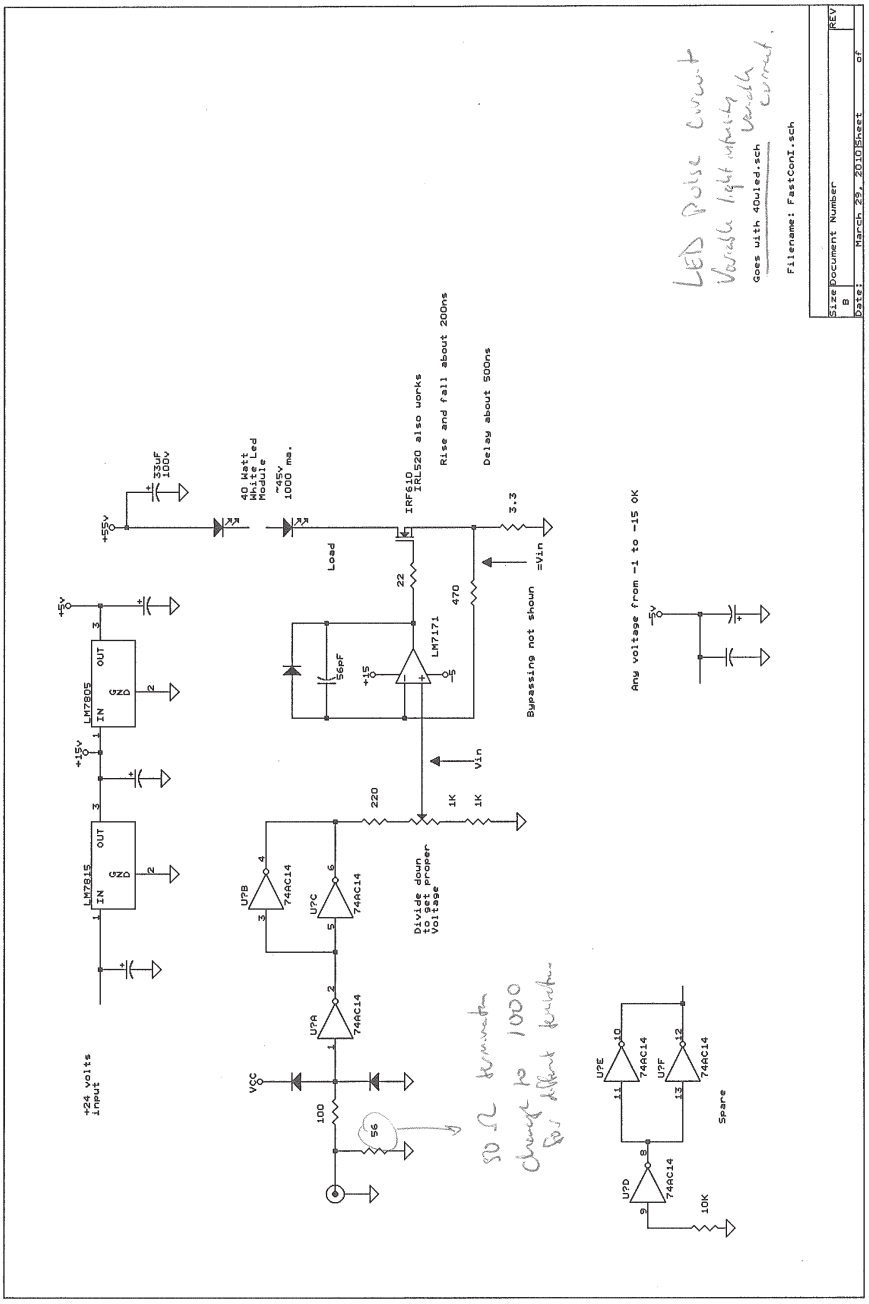


Figure A.5: High power LED pulsing circuit Hargather et al. [2009]

Appendix B

DVD

DVD folder contents:

1. MSc Dissertation
2. Tecplot Schlieren Script
3. Matlab Source Mask Script
4. OpenCV Code
5. Matlab Image Integration Code
6. Optics Software
7. Lukes Code CFD Configuration
8. High Speed Video Footage
9. Schlieren Optics Setup Video
10. Circuit Components